Rosenthal, Y., Holbourn, A.E., Kulhanek, D.K., and the Expedition 363 Scientists
Proceedings of the International Ocean Discovery Program Volume 363
publications.iodp.org

https://doi.org/10.14379/iodp.proc.363.107.2018

Site U1486[1]

Y. Rosenthal, A.E. Holbourn, D.K. Kulhanek, I.W. Aiello, T.L. Babila, G. Bayon, L. Beaufort, S.C. Bova, J.-H. Chun, H. Dang, A.J. Drury, T. Dunkley Jones, P.P.B. Eichler, A.G.S. Fernando, K.A. Gibson, R.G. Hatfield, D.L. Johnson, Y. Kumagai, T. Li, B.K. Linsley, N. Meinicke, G.S. Mountain, B.N. Opdyke, P.N. Pearson, C.R. Poole, A.C. Ravelo, T. Sagawa, A. Schmitt, J.B. Wurtzel, J. Xu, M. Yamamoto, and Y.G. Zhang[2]

Keywords: International Ocean Discovery Program, IODP, *JOIDES Resolution*, Expedition 363, Site U1486, Manus Basin, Bismarck microplate, central sector Western Pacific Warm Pool, Pleistocene, late Pliocene, Indonesian Throughflow, New Guinea Coastal Current, suborbital to orbital scale climate variability, Admiralty Islands volcanism, tephra, basalt, volcanogenic sediment, volcanic ash, scoria, zeolite, exceptional foraminifer and nannofossil preservation, stratigraphic intercalibration and cyclostratigraphy, high-resolution interstitial water sampling, Last Glacial Maximum ocean density structure, diagenesis, anaerobic methane oxidation, sulfate–methane transition zone, SMTZ, clay mineral authigenesis

Contents

Background and objectives

International Ocean Discovery Program (IODP) Site U1486 (proposed Site WP-05A) is located ~215 km west-southwest of Manus Island at 02°22.34′S, 144°36.08′E in 1332 m water depth (Figure F1). The site is situated at the cross-point of seismic Lines GeoB13-084 and GeoB13-088 (Figure F2). The seismic profile shows a continuous succession of hemipelagic sediment with acoustic basement estimated at ~225 meters below seafloor (mbsf) (Rosenthal et al., 2016) (Figure F3). This site was targeted to recover a complete Pleistocene record with unprecedented resolution for the Western Pacific Warm Pool (WPWP).

The tectonic setting of Sites U1486 and U1487 (similar to that of the northern Papua New Guinea Sites U1484 and U1485) was shaped by the oblique northward movement of the Australian plate as it rapidly converged with the Pacific plate. This collision resulted in a complex plate boundary zone that includes volcanic arcs but also resulted in the formation and rotation of microplates within

Figure F1. Northern margin of Papua New Guinea showing location of Sites U1484–U1487 (yellow circles). Contour interval = 500 m.

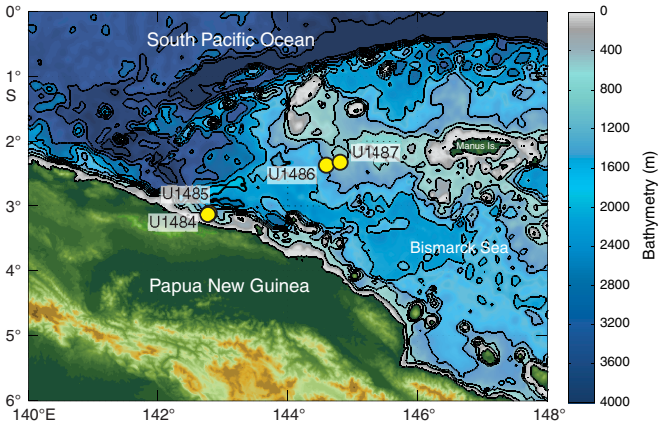

Figure F2. Bathymetric map showing location of Site U1486 at intersection of seismic Lines GeoB13-084 (west–east) and GeoB13-088 (south–north) collected during the R/V *Sonne* SO-228 cruise (Mohtadi et al., 2013). Bathymetry is based on EM122 multibeam survey collected during same cruise. Numbers along seismic lines (black) are shotpoints.

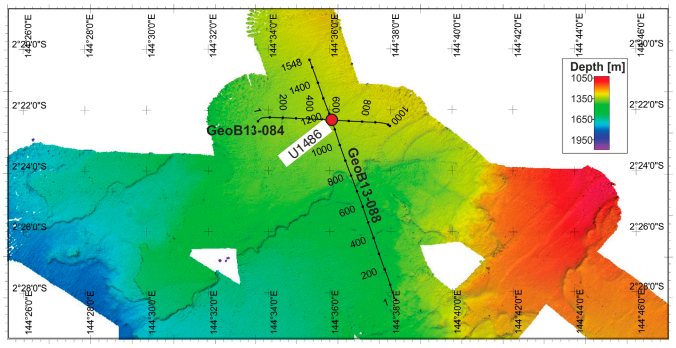

[1] Rosenthal, Y., Holbourn, A.E., Kulhanek, D.K., Aiello, I.W., Babila, T.L., Bayon, G., Beaufort, L., Bova, S.C., Chun, J.-H., Dang, H., Drury, A.J., Dunkley Jones, T., Eichler, P.P.B., Fernando, A.G.S., Gibson, K.A., Hatfield, R.G., Johnson, D.L., Kumagai, Y., Li, T., Linsley, B.K., Meinicke, N., Mountain, G.S., Opdyke, B.N., Pearson, P.N., Poole, C.R., Ravelo, A.C., Sagawa, T., Schmitt, A., Wurtzel, J.B., Xu, J., Yamamoto, M., and Zhang, Y.G., 2018. Site U1486. *In* Rosenthal, Y., Holbourn, A.E., Kulhanek, D.K., and the Expedition 363 Scientists, *Western Pacific Warm Pool*. Proceedings of the International Ocean Discovery Program, 363: College Station, TX (International Ocean Discovery Program). https://doi.org/10.14379/iodp.proc.363.107.2018

[2] **Expedition 363 Scientists' addresses.**

MS 363-107: Published 8 June 2018

Figure F3. Seismic lines showing location of Site U1486. Dashed lines at top show the intersection of the two lines. SP = shotpoint. A. Seismic Line GeoB13-084 (west–east). B. Seismic Line GeoB13-088 (south–north) (Mohtadi et al., 2013).

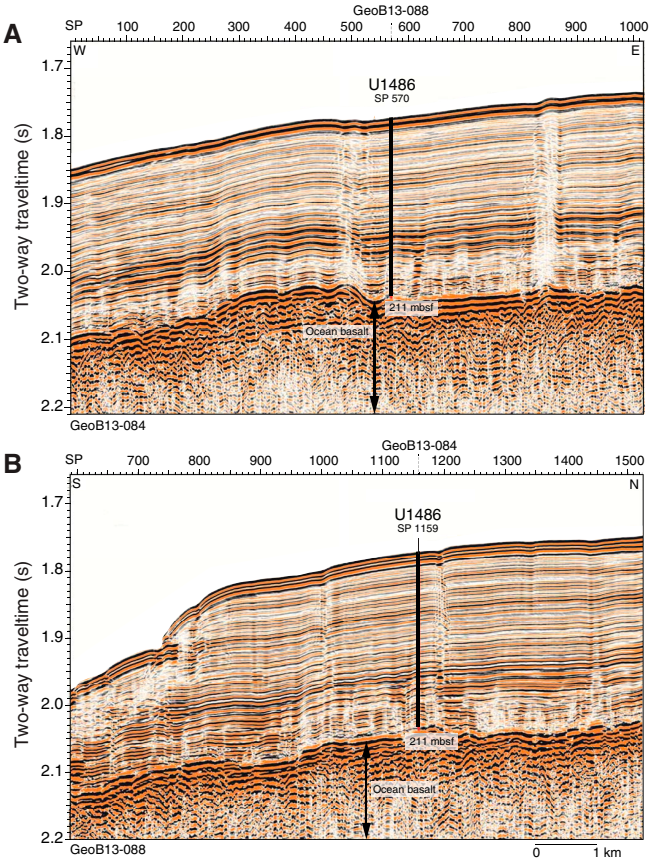

Figure F4. Hydrographic profiles of temperature, salinity, and dissolved oxygen northeast of Papua New Guinea along the path of the New Guinea Coastal Current (Y. Rosenthal, unpubl. data). SPSTW = South Pacific Subtropical Water, AAIW = Antarctic Intermediate Water, UCDW = Upper Circumpolar Deepwater.

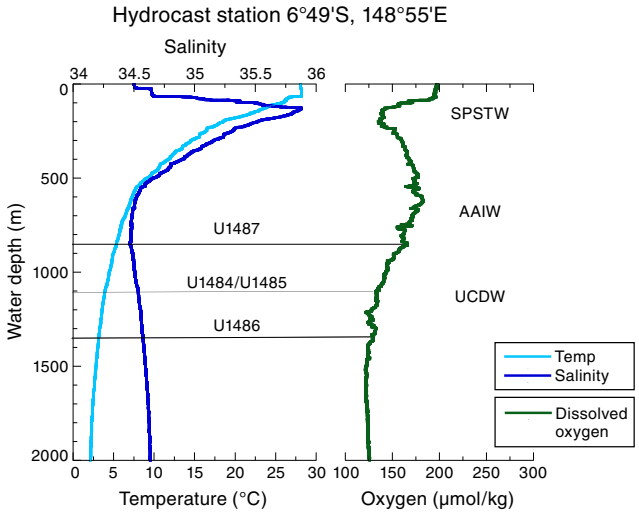

this zone, as well as lithospheric rupture that formed small oceanic basins (Baldwin et al., 2012). The Bismarck Sea, on the northeastern side of Papua New Guinea (Figure **F1**), forms a back-arc basin with respect to the New Britain arc and is divided into the North Bismarck (NBS) and South Bismarck (SBS) microplates, separated by the active Bismarck Sea left-lateral transform fault and spreading segments (Taylor, 1979). Site U1486 is located on the NBS microplate. To the north, the NBS microplate is bordered by the Manus Trench, which defines the boundary between it and the Pacific plate. Within this complex tectonic regime, the southwestern side of the Manus Basin is considered one of the more stable regions. Magnetic anomalies in the Bismarck Sea indicate rapid asymmetric spreading since 3.5 Ma (Taylor, 1979). The continuous collision between the Australian and Pacific plates causes the SBS microplate to rotate rapidly clockwise (~9°/My), whereas the NBS microplate is rotating slowly anticlockwise (0.3–1.25°/My) (Baldwin et al., 2012). Asymmetric rotation of the North and South Bismarck Basins likely changed the position of New Britain and adjacent islands relative to Papua New Guinea. Ocean Drilling Program (ODP) Leg 193 focused on the eastern part of the Manus Basin, exploring the tectonic, volcanic, and seafloor hydrothermal system activity in this convergent plate margin setting.

An isotope record from piston Core MD05-2920 located near Site U1486 indicates a sedimentation rate of ~10 cm/ky, substantially higher than that found in other open-ocean Pacific sites, with no discernible disturbance for the past ~400 ky (Tachikawa et al., 2011, 2013). The moderately high $CaCO_3$ content (25–45 wt%) and well-preserved foraminifer tests suggest the potential to generate a suborbitally resolved paleoceanographic record of unprecedented quality through the Pleistocene. X-ray fluorescence scanning of Core MD05-2920 demonstrates that centennial precipitation variability can be resolved from the elemental content of the sediment (Tachikawa et al., 2011).

This site was targeted because of its potential to provide an excellent Pleistocene paleoceanographic record to examine orbital-scale climate variability at high resolution through the Pleistocene. The site is ideally located to monitor the contribution from the New Guinea Coastal Current and Undercurrent to the Indonesian Throughflow (ITF). The New Guinea Coastal Current is the southern branch of the westward, cross-equatorial flowing South Equatorial Current and constitutes the main southern Pacific contribution to the surface transport of the ITF. At ~1300 meters below sea level (mbsl), this site is bathed by Upper Circumpolar Deepwater originating from the Southern Ocean (Figure **F4**) and thus will allow for the reconstruction of past variability of this water mass.

Operations

Transit to Site U1486

The 117 nmi transit to Site U1486 was completed in 9.9 h at an average speed of 11.8 kt. We lowered the thrusters and switched to dynamic positioning mode at 0921 h (all times local ship time; UTC + 10 h) on 14 November 2016. After arriving on site, we deployed a positioning beacon at 0942 h before commencing coring operations.

Operations summary

The original operations plan included three holes using the advanced piston corer (APC) to 200 mbsf. We ultimately cored four holes (Table **T1**). Hole U1486A consisted of a single full core and was terminated because it did not recover the mudline. Holes U1486B and U1486C were cored to 211.2 and 201.3 mbsf, respectively. Hole U1486D was cored to 186.5 mbsf to fill coring gaps and

intervals where significant numbers of interstitial water samples were taken from Hole U1486B for construction of the composite section.

Hole U1486A was cored to 9.5 mbsf with the APC using orientation and nonmagnetic hardware. When Core 363-U1486A-1H retrieved a full core liner, indicating that we missed the mudline, we terminated coring in this hole. A total of 9.95 m of sediment was recovered over 9.5 m of coring (105% recovery) in Hole U1486A.

Hole U1486B was cored to 211.2 mbsf (Cores 363-U1486B-1H through 23H) using the APC with orientation and nonmagnetic hardware. Downhole formation temperature measurements using the advanced piston corer temperature tool (APCT-3) were taken on Cores 4H (34.5 mbsf), 7H (63.0 mbsf), 10H (91.5 mbsf), and 13H (120.0 mbsf), obtaining good results on all four deployments. Whole-round samples for high-resolution interstitial water analyses were taken at a frequency of one per section in the upper 150 mbsf of Hole U1486B. Core 23H seemed to be a full stroke; however, only 5.67 m of core was recovered. When drilling out the "rathole," drilling stalled at 211.2 mbsf, indicating something hard at that depth that the core barrel was unable to penetrate. Given that the acoustic basement at Site U1486 was estimated at ~225 mbsf, we speculate that we encountered the acoustic basement at a somewhat shallower depth. The presence of a few small basalt fragments in the core catcher of Core 23H supports this interpretation. We collected 215.49 m of sediment over 211.2 m of coring (102% recovery) in Hole U1486B.

Hole U1486C was cored to 201.3 mbsf (Cores 363-U1486C-1H through 23H) using the APC with orientation and nonmagnetic hardware. We decided to terminate coring above the hard layer encountered in Hole U1486B. Two drilled intervals (each 2 m) were used to advance the hole without recovery for stratigraphic correlation and one core (Core 11H) did not recover any material. We collected 172.70 m of sediment over 197.3 m of coring (88% recovery) in Hole U1486C.

Hole U1486D was cored to 186.5 mbsf in order to fill gaps in the composite stratigraphic section. Continuous coring penetrated to 153.2 mbsf (Cores 363-U1486-1H through 16H) with the APC using orientation and nonmagnetic hardware. We then drilled ahead without coring to 177 mbsf (23.8 m advance) to shoot Core 19H to capture a paleomagnetic reversal that was recovered in Hole U1486B but had fallen within a core gap in Hole U1486C. We collected 166.53 m of core over 162.7 m of coring (102% recovery) in Hole U1486D. Operations at Site U1486 ended at 1015 h on 17 November 2016. Total time spent at Site U1486 was 73.0 h (3.0 d).

A total of 63 APC cores were recovered at this site, collecting 564.67 m of sediment over 580.7 m of coring (97.2% recovery).

Hole U1486A

We prepared and spaced out the bottom-hole assembly (BHA), which consisted of an APC/extended core barrel (XCB) coring assembly with two stands of drill collars. During deployment of the drill string, the seafloor depth was measured at 1346.4 meters below rig floor (mbrf) with the precision depth recorder (PDR), and we positioned the bit at 1341.5 mbrf to shoot the first core. Hole U1486A was spudded at 1545 h on 14 November 2016. Core 363-U1486A-1H recovered 9.95 m of sediment using the APC. We terminated coring in Hole U1486A at 1600 h after retrieval of the first core due to the missed mudline. Total time spent in Hole U1486A was 6.75 h (0.3 days).

A single APC core was taken in Hole U1486A. We recovered 9.95 m of sediment over 9.5 m of coring for a recovery of 104.7%.

Hole U1486B

The vessel was offset 20 m east of Hole U1486A, and the drill string was spaced out with the bit at 1341.5 mbrf. Hole U1486B was spudded at 1645 h on 14 November 2016, with Core 363-U1486B-1H recovering 5.99 m of sediment, establishing a seafloor depth of 1333.8 mbsl. Oriented APC coring using the Icefield MI-5 core orientation tool with nonmagnetic hardware continued to 211.2 mbsf (Cores 1H through 23H). Downhole formation temperature measurements using the APCT-3 were taken on Cores 4H (34.5 mbsf), 7H (63.0 mbsf), 10H (91.5 mbsf), and 13H (120.0 mbsf), obtaining good results on all four deployments. Whole-round samples for high-resolution interstitial water analyses were taken at a frequency of one 5 or 10 cm sample per section in the upper 150 mbsf of Hole U1486B (through Section 363-U1486B-17H-2). Core 7H had a twisted and split liner, and Cores 21H and 22H had excessive overpull that required drillover to extract them from the formation. Core 23H seemed to be a full stroke; however, only 5.67 m of core was recovered. When drilling out the rathole, drilling stalled at 211.2 mbsf, indicating something hard at that depth that the core barrel was unable to penetrate. Given that the acoustic basement at Site U1486 was estimated at ~225 mbsf, we speculate that we encountered the acoustic basement at a slightly shallower depth. The presence of a few small basalt fragments in the core catcher of Core 23H supports this interpretation. We terminated coring at 211.2 mbsf, with the bit clearing the seafloor at 1250 h on 15 November. Total time spent on Hole U1486B was 20.75 h (0.9 days).

A total of 23 APC cores were taken in Hole U1486B. We recovered 215.49 m of sediment over 211.2 m of coring for a total recovery of 102.0%.

Hole U1486C

The vessel was offset 20 m south of Hole U1486B, and the drill string was spaced out with the bit at 1343.5 mbrf. Hole U1486C was spudded at 1415 h on 15 November 2016, with Core 363-U1486C-1H recovering 7.34 m of sediment, establishing a seafloor depth of 1334.5 mbsl. Oriented APC coring using the Icefield MI-5 core orientation tool with nonmagnetic hardware continued to 201.3 mbsf (Cores 1H through 23H). Two drilled intervals of 2 m each advanced the hole without coring to avoid alignment of core gaps for stratigraphic correlation purposes. Core 11H had no recovery, and the bottom of the core liner imploded on Core 13H. Four cores required drillover to extract them from the formation due to excessive overpull (Cores 17H, 18H, 22H, and 23H). We opted to terminate coring at 201.3 mbsf, well above the hard layer encountered in Hole U1486B. The bit cleared the seafloor at 1015 h on 16 November. Total time spent in Hole U1486C was 21.50 h (0.9 days).

A total of 21 APC cores were taken in Hole U1486C. We recovered 172.7 m of sediment over 197.3 m of coring for a total recovery of 87.5%. Two drilled intervals advanced the hole 4 m without coring.

Hole U1486D

Hole U1486D was cored to fill gaps in the stratigraphic section, particularly over the upper 150 mbsf of high-resolution interstitial water sampling in Hole U1486B. The vessel was offset 20 m west of

Hole U1486C, and the drill string was spaced out with the bit at 1337.0 mbrf. Hole U1486D was spudded at 1320 h on 16 November 2016, with Core 363-U1486D-1H recovering 1.23 m of sediment, establishing a seafloor depth of 1334.1 mbsl. Oriented APC coring using the Icefield MI-5 core orientation tool with nonmagnetic hardware continued to 153.2 mbsf (Cores 1H through 17H). We then drilled ahead without coring to 177 mbsf (23.8 m advance) to shoot Core 19H and capture a paleomagnetic reversal that was recovered in Hole U1486B but had fallen within a core gap in Hole U1486C. Cores 3H and 8H had split liners, and Core 16H required drillover to extract it from the formation. We terminated coring after Core 19H at 186.5 mbsf. The drill string was retrieved to the vessel, with the bit clearing the rotary table at 1010 h on 17 November. The positioning beacon was recovered after the bit cleared the seafloor. The rig was secured for transit, and the thrusters were raised, ending operations at Site U1486 at 1015 h on 17 November. Total time spent in Hole U1486D was 24.0 h (1 day).

A total of 18 APC cores were taken in Hole U1486D. We recovered 166.53 m of sediment over 162.7 m of coring for a total recovery of 102.4%. A single drilled interval advanced the hole 23.8 m without coring.

Table T1. Site U1486 core summary. CSF = core depth below seafloor (mbsf in text), DRF = drilling depth below rig floor, DSF = drilling depth below seafloor. APC = advanced piston corer, XCB = extended core barrel, HLAPC = half-length advanced piston corer. Core types: H = advanced piston corer, numeric core type = drilled interval. APCT-3 = advanced piston corer temperature tool, Icefield = orientation tool. (Continued on next page.) **Download table in CSV format.**

Hole U1486A
Latitude: 02°22.3375′S
Longitude: 144°36.0796′E
Water depth (m): 1330.33
Date started (UTC): 13 November 2016, 2321 h
Date finished (UTC): 14 November 2016, 0600 h
Time on hole (days): 0.28
Seafloor depth DRF (m): 1341.5
Seafloor depth calculation method: APC calculated depth
Rig floor to sea level (m): 11.17
Drilling system: 11-7/16 inch APC/XCB DC280 bit
Penetration DSF (m): 9.5
Cored interval (m): 9.5
Recovered length (m): 9.95
Recovery (%): 104.74
Total cores (no.): 1
APC cores (no.): 1
Age of oldest sediment cored: late Pleistocene

Hole U1486B
Latitude: 02°22.3368′S
Longitude: 144°36.0794′E
Water depth (m): 1333.83
Date started (UTC): 14 November 2016, 0600 h
Date finished (UTC): 15 November 2016, 0250 h
Time on hole (days): 0.87
Seafloor depth DRF (m): 1345.0
Seafloor depth calculation method: APC calculated depth
Rig floor to sea level (m): 11.17
Drilling system: 11-7/16 inch APC/XCB DC280 bit
Penetration DSF (m): 211.2
Cored interval (m): 211.2
Recovered length (m): 215.49
Recovery (%): 102.03
Total cores (no.): 23
APC cores (no.): 23
Age of oldest sediment cored: late Pliocene

Hole U1486C
Latitude: 02°22.3478′S
Longitude: 144°36.0798′E
Water depth (m): 1334.5
Date started (UTC): 15 November 2016, 0250 h
Date finished (UTC): 16 November 2016, 0010 h
Time on hole (days): 0.89
Seafloor depth DRF (m): 1345.7
Seafloor depth calculation method: APC calculated depth
Rig floor to sea level (m): 11.20
Drilling system: 11-7/16 inch APC/XCB DC280 bit
Penetration DSF (m): 201.3
Cored interval (m): 197.3
Recovered length (m): 172.70
Recovery (%): 87.53
Drilled interval (m): 4
Drilled interval (no.): 2
Total cores (no.): 21
APC cores (no.): 21
Age of oldest sediment cored: late Pliocene

Hole U1486D
Latitude: 02°22.3484′S
Longitude: 144°36.0690′E
Water depth (m): 1334.1
Date started (UTC): 16 November 2016, 0010 h
Date finished (UTC): 17 November 2016, 0018 h
Time on hole (days): 1.01
Seafloor depth DRF (m): 1345.3
Seafloor depth calculation method: APC calculated depth
Rig floor to sea level (m): 11.20
Drilling system: 11-7/16 inch APC/XCB DC280 bit
Penetration DSF (m): 186.5
Cored interval (m): 162.7
Recovered length (m): 166.53
Recovery (%): 102.35
Drilled interval (m): 23.8
Drilled interval (no.): 1
Total cores (no.): 18
APC cores (no.): 18
Age of oldest sediment cored: late Pliocene

Core	Date (2016)	Time on deck UTC (h)	Depth DSF (m) Top of interval	Depth DSF (m) Bottom of interval	Interval advanced (m)	Depth CSF (m) Top of cored interval	Depth CSF (m) Bottom of cored interval	Recovered length (m)	Curated length (m)	Recovery (%)	Sections (*N*)	Comments
363-U1486A-												
1H	14 Nov	0600	0	9.5	9.5	0	9.95	9.95	9.95	105	8	Icefield
363-U1486B-												
1H	14 Nov	0700	0	6.0	6.0	0	5.99	5.99	5.99	100	5	Icefield
2H	14 Nov	0750	6.0	15.5	9.5	6.0	16.06	10.06	10.06	106	8	Icefield
3H	14 Nov	0830	15.5	25.0	9.5	15.5	25.42	9.92	9.92	104	8	Icefield
4H	14 Nov	0920	25.0	34.5	9.5	25.0	35.10	10.10	10.10	106	8	Icefield, APCT-3
5H	14 Nov	0950	34.5	44.0	9.5	34.5	44.45	9.95	9.95	105	8	Icefield
6H	14 Nov	1025	44.0	53.5	9.5	44.0	53.93	9.93	9.93	105	8	Icefield

Table T1 (continued).

Core	Date (2016)	Time on deck UTC (h)	Depth DSF (m) Top of interval	Depth DSF (m) Bottom of interval	Interval advanced (m)	Depth CSF (m) Top of cored interval	Depth CSF (m) Bottom of cored interval	Recovered length (m)	Curated length (m)	Recovery (%)	Sections (*N*)	Comments
7H	14 Nov	1115	53.5	63.0	9.5	53.5	62.86	9.36	9.36	99	7	Icefield, APCT-3, liner twisted and split throughout
8H	14 Nov	1200	63.0	72.5	9.5	63.0	72.79	9.79	9.79	103	8	Icefield
9H	14 Nov	1230	72.5	82.0	9.5	72.5	82.52	10.02	10.02	105	8	Icefield
10H	14 Nov	1320	82.0	91.5	9.5	82.0	91.90	9.90	9.90	104	8	Icefield, APCT-3
11H	14 Nov	1405	91.5	101.0	9.5	91.5	101.44	9.94	9.94	105	8	Icefield
12H	14 Nov	1445	101.0	110.5	9.5	101.0	110.99	9.99	9.99	105	8	Icefield
13H	14 Nov	1535	110.5	120.0	9.5	110.5	120.16	9.69	9.66	102	8	Icefield, APCT-3
14H	14 Nov	1620	120.0	129.5	9.5	120.0	129.98	9.98	9.98	105	8	Icefield
15H	14 Nov	1655	129.5	139.0	9.5	129.5	139.22	9.72	9.72	102	8	Icefield
16H	14 Nov	1735	139.0	148.5	9.5	139.0	148.94	9.94	9.94	105	8	Icefield
17H	14 Nov	1830	148.5	158.0	9.5	148.5	158.42	9.92	9.92	104	8	Icefield
18H	14 Nov	1930	158.0	167.5	9.5	158.0	167.55	9.55	9.55	101	8	Icefield
19H	14 Nov	2005	167.5	177.0	9.5	167.5	174.16	6.71	6.66	71	6	Icefield
20H	14 Nov	2045	177.0	186.5	9.5	177.0	187.00	10.00	10.00	105	8	Icefield
21H	14 Nov	2230	186.5	196.0	9.5	186.5	196.07	9.57	9.57	101	8	Icefield
22H	14 Nov	2350	196.0	205.5	9.5	196.0	205.79	9.79	9.79	103	8	Icefield
23H	15 Nov	0030	205.5	211.2	5.7	205.5	211.17	5.67	5.67	99	5	Icefield, encountered refusal while drilling out rathole
363-U1486C-												
1H	15 Nov	0430	0	7.3	7.3	0	7.34	7.34	7.34	101	6	Icefield
2H	15 Nov	0510	7.3	16.8	9.5	7.3	16.56	9.26	9.26	97	8	Icefield
31	15 Nov	0605	16.8	18.8	2.0	*****Drilled from 16.8 to 18.8 m DSF without coring*****						
4H	15 Nov	0630	18.8	28.3	9.5	18.8	28.60	9.80	9.80	103	8	Icefield
5H	15 Nov	0720	28.3	37.8	9.5	28.3	38.15	9.85	9.85	104	8	Icefield
6H	15 Nov	0800	37.8	47.3	9.5	37.8	43.23	5.43	5.43	57	5	Icefield
71	15 Nov	0850	47.3	49.3	2.0	*****Drilled from 47.3 to 49.3 m DSF without coring*****						
8H	15 Nov	0925	49.3	58.8	9.5	49.3	59.09	9.79	9.79	103	8	Icefield
9H	15 Nov	1015	58.8	68.3	9.5	58.8	67.51	8.71	8.71	92	7	Icefield
10H	15 Nov	1050	68.3	77.8	9.5	68.3	77.06	8.76	8.76	92	7	Icefield
11H	15 Nov	1130	77.8	87.3	9.5	77.8	87.30	0	8.76	0	0	Icefield
12H	15 Nov	1220	87.3	96.8	9.5	87.3	96.96	9.77	9.66	103	8	Icefield
13H	15 Nov	1255	96.8	106.3	9.5	96.8	105.46	8.66	8.66	91	7	Icefield, liner imploded (bottom)
14H	15 Nov	1330	106.3	115.8	9.5	106.3	116.18	9.88	9.88	104	8	Icefield
15H	15 Nov	1410	115.8	125.3	9.5	115.8	125.58	9.78	9.78	103	8	Icefield
16H	15 Nov	1445	125.3	134.8	9.5	125.3	128.03	2.73	2.73	29	3	Icefield
17H	15 Nov	1615	134.8	144.3	9.5	134.8	144.39	9.59	9.59	101	8	Icefield, drillover
18H	15 Nov	1735	144.3	153.8	9.5	144.3	154.07	9.77	9.77	103	8	Icefield
19H	15 Nov	1815	153.8	163.3	9.5	153.8	162.18	8.38	8.38	88	7	Icefield
20H	15 Nov	1855	163.3	172.8	9.5	163.3	171.68	8.38	8.38	88	7	Icefield
21H	15 Nov	1940	172.8	182.3	9.5	172.8	181.40	8.60	8.60	91	7	Icefield
22H	15 Nov	2110	182.3	191.8	9.5	182.3	191.34	9.04	9.04	95	7	Icefield
23H	15 Nov	2215	191.8	201.3	9.5	191.8	200.98	9.18	9.18	97	7	Icefield
363-U1486D-												
1H	16 Nov	0330	0	1.2	1.2	0	1.23	1.23	1.23	103	2	Icefield
2H	16 Nov	0420	1.2	10.7	9.5	1.2	10.38	9.18	9.18	97	8	Icefield
3H	16 Nov	0615	10.7	20.2	9.5	10.7	20.83	10.13	10.13	107	8	Icefield, required 2 wireline runs
4H	16 Nov	0645	20.2	29.7	9.5	20.2	30.04	9.84	9.84	104	8	Icefield, core liner split throughout
5H	16 Nov	0815	29.7	39.2	9.5	29.7	39.70	10.00	10.00	105	8	Icefield
6H	16 Nov	0915	39.2	48.7	9.5	39.2	49.08	9.88	9.88	104	8	Icefield
7H	16 Nov	0950	48.7	58.2	9.5	48.7	58.66	9.96	9.96	105	8	Icefield
8H	16 Nov	1040	58.2	67.7	9.5	58.2	67.88	10.11	9.68	106	8	Icefield, core liner split throughout
9H	16 Nov	1115	67.7	77.2	9.5	67.7	77.69	9.99	9.99	105	8	Icefield
10H	16 Nov	1150	77.2	86.7	9.5	77.2	84.35	7.15	7.15	75	6	Icefield
11H	16 Nov	1225	86.7	96.2	9.5	86.7	96.71	10.01	10.01	105	8	Icefield
12H	16 Nov	1300	96.2	105.7	9.5	96.2	106.12	9.92	9.92	104	8	Icefield
13H	16 Nov	1330	105.7	115.2	9.5	105.7	115.65	9.95	9.95	105	8	Icefield
14H	16 Nov	1415	115.2	124.7	9.5	115.2	125.00	9.80	9.80	103	8	Icefield
15H	16 Nov	1515	124.7	134.2	9.5	124.7	134.69	9.99	9.99	105	8	Icefield
16H	16 Nov	1630	134.2	143.7	9.5	134.2	144.10	9.90	9.90	104	8	Icefield, drillover
17H	16 Nov	1710	143.7	153.2	9.5	143.7	153.44	9.74	9.74	103	8	Icefield
181	16 Nov	1800	153.2	177.0	23.8	*****Drilled from 153.2 to 177 m DSF without coring*****						
19H	16 Nov	1835	177.0	186.5	9.5	177.0	186.75	9.75	9.75	103	8	Icefield

Core description

We cored four holes at Site U1486, with the deepest hole penetrating to 211.20 mbsf (Hole U1486B) and the shallowest to 9.95 mbsf (Hole U1486A). The cores recovered from Site U1486 are composed of upper Pliocene to recent volcanogenic sediments, biogenic sediments, and authigenic minerals overlying oceanic basement, which was not cored. The relative abundance of the volcanogenic and biogenic components varies significantly downhole. Based on lithologic changes identified by a combination of visual core description, microscopic examination of smear slides, magnetic susceptibility, natural gamma radiation (NGR), color reflectance, and mineralogical analysis by X-ray diffraction (XRD) (see **Core description** and **Physical properties** in the Expedition 363 methods chapter [Rosenthal et al., 2018a]), we assign the recovered succession to one lithologic unit, which is divided into three subunits (Figure **F5**). Subunit IA (~57 m thick) includes mid-Pleistocene to recent mainly biogenic (nannofossil and foraminifer) sediment mixed with clay minerals and rare ash-rich layers. Subunit IB (~85 m thick) consists mainly of lower Pleistocene biogenic sediment with volcanic particles (ash and pumice), which occur both as dispersed particles and distinct layers (tephra). Subunit IC (~70 m thick; upper Pliocene to lower Pleistocene) is dominated by volcanic particles in discrete lamina and layers of different thicknesses, grain sizes (from a few millimeter-sized glass shards to several large scoria fragments), and colors. These are interbedded with a biogenic component that is also mixed with dispersed volcanic particles. The lowermost ~4 m of Subunit IC is permeated by authigenic zeolites of probable hydrothermal origin. The presence of both subrounded and angular fragments of basaltic rocks and hydrothermal precipitates indicates proximity to the oceanic basement.

Unit description

Unit I

Intervals: 363-U1486A-1H-1, 0 cm, through 1H-CC, 21 cm; 363-U1486B-1H-1, 0 cm, through 23H-CC, 8 cm; 363-U1486C-1H-1, 0 cm, through 23H-CC, 29 cm; 363-U1486D-1H-1, 0 cm, through 19H-CC, 24 cm

Depths: Hole U1486A = 0–9.95 mbsf, Hole U1486B = 0–211.17 mbsf, Hole U1486C = 0–200.98 mbsf, Hole U1486D = 0–186.75 mbsf

Thickness: Hole U1486A = 9.95 m, Hole U1486B = 211.17 m, Hole U1486C = 200.98 m, Hole U1486D = 186.75 m

Age: late Pliocene to recent

Lithology: radiolarian-bearing foraminifer- and clay-rich nannofossil ooze, nannofossil clay, ashy sand, and ash

Unit I is composed of ~211 m of upper Pliocene to recent biogenic, siliciclastic (mainly clay minerals), and volcanogenic sediment (Figures **F5**, **F6**, **F7**, **F8**). These sedimentary components occur both mixed together and alternating in layers with distinct lithologic compositions. Bioturbation is moderate to light throughout the unit. The upper ~57 mbsf of the site (Subunit IA; latest early Pleistocene to recent) is dominated by biogenic ooze (mainly nannofossils and foraminifers) (Figure **F6A, F6B**) with variable (bearing to rich) amounts of clay minerals and with a few interbedded layers (between ~2 and 5 cm thick) in which volcanic glass occurs mixed with biogenic sediment (Figure **F9**). Volcanogenic particles increase in frequency downhole, and volcanic glass and pumice occur both mixed with the hemipelagic sediment and in distinct tephra layers in Subunit IB (early Pleistocene). The volcanogenic component is most abundant in the bottom part of the site in

Figure F5. Lithologic summary, Site U1486. cps = counts per second, MS = magnetic susceptibility, SHMSL = Section Half Multisensor Logger.

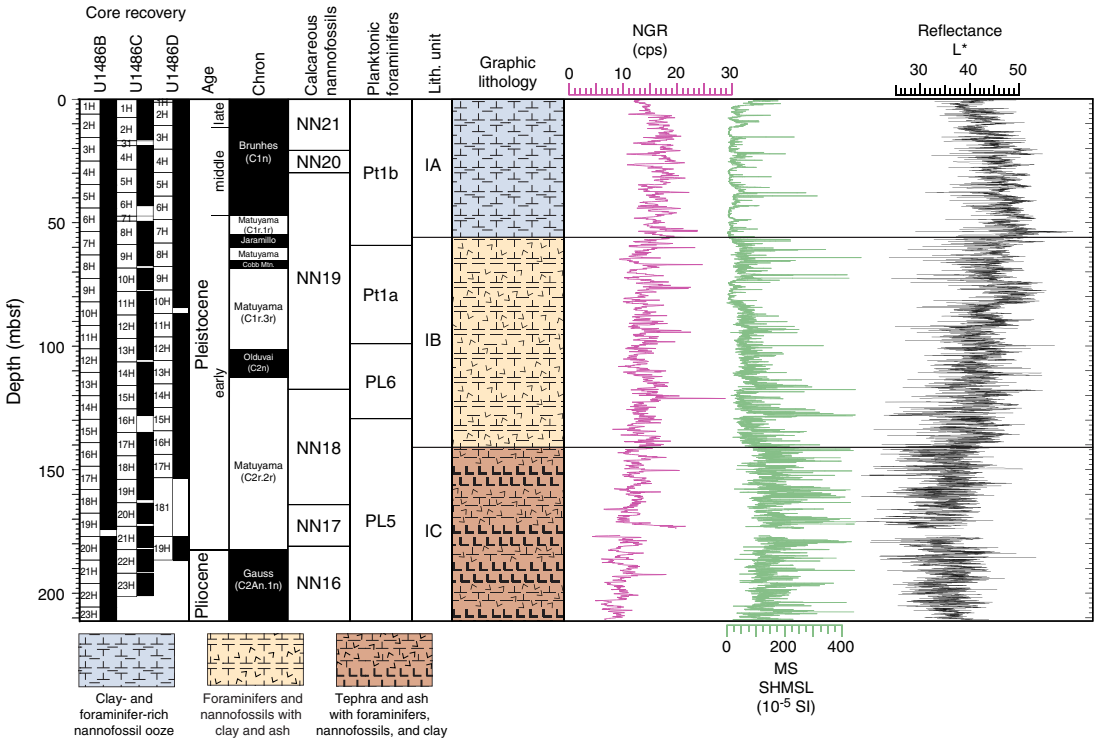

Figure F6. Main sedimentary components, Site U1486. A, B. Foraminifer- and clay-rich nannofossil ooze (Subunit IA). C, D. Foraminifer-rich ashy nannofossil ooze (Subunit IB). E, F. Silt- and sand-sized volcanogenic particles and feldspars (Fs) (Subunit IC). A, C, and E: plane-polarized light (PPL); B, D, and F: cross-polarized light (XPL).

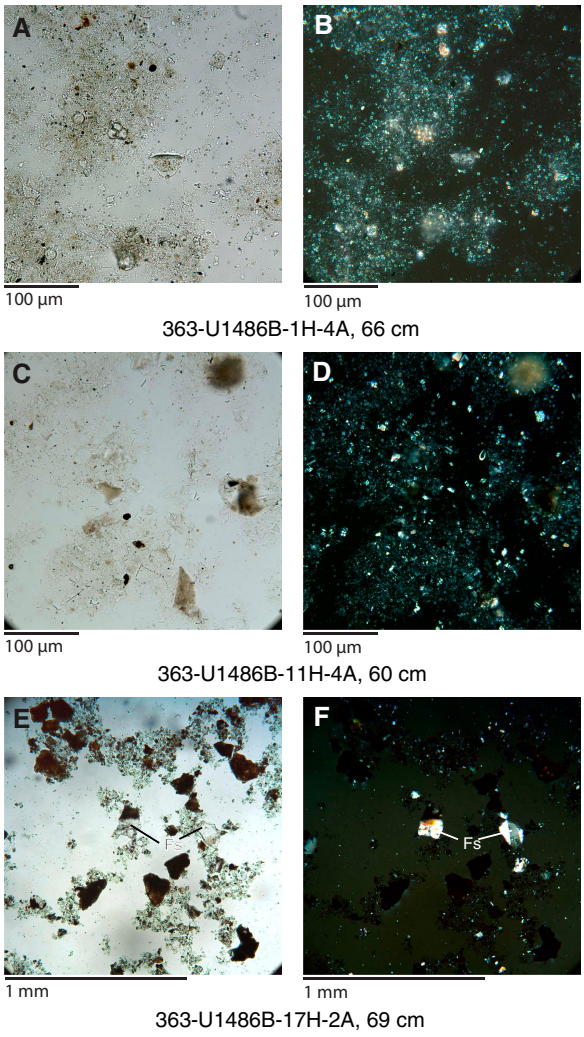

Figure F7. Biosiliceous sedimentary components, Site U1486. A. Centric and pennate diatoms (mudline). B. Radiolarian and partially preserved centric diatom.

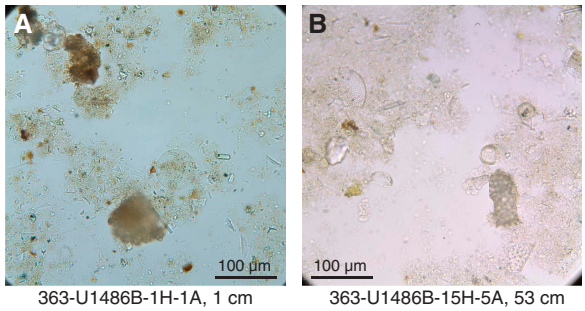

Figure F8. Main lithologies, Site U1486. A. Mainly biogenic sediment (Subunit IA). B. Alternating dark–light biogenic and volcanogenic sediment (Subunit IB). C. Dominantly volcanogenic sediment (Subunit IC).

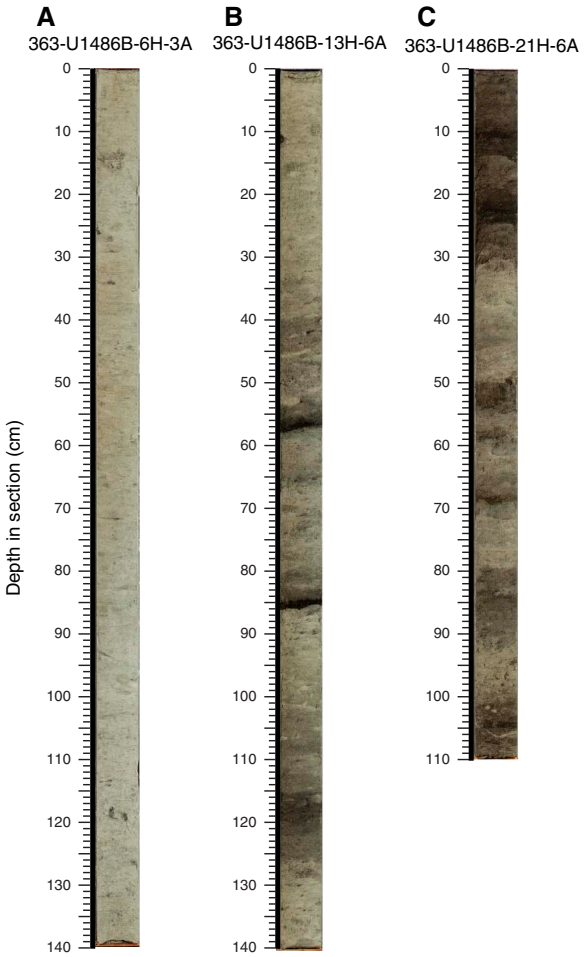

Subunit IC (late Pliocene to early Pleistocene; Figure **F10**), whereas both biogenic and clay components are less abundant. The volcanic material is generally dark (mainly scoria), and green patches indicating glass alteration are frequently observed on the split-core surface. At the bottom of the site, a ~4 m thick interval characterized by zeolite precipitates (probably mordenite) and basalt fragments indicates likely proximity to oceanic crust (Figure **F11**).

Subunit IA

Intervals: 363-U1486A-1H-1, 0 cm, through 1H-CC, 21 cm; 363-U1486B-1H-1, 0 cm, through 7H-3, 27 cm; 363-U1486C-1H-1, 0 cm, through 8H-6, 75 cm; 363-U1486D-1H-1, 0 cm, through 7H-7, 32.5 cm

Depths: Hole U1486A = 0–9.95 mbsf (total depth), Hole U1486B = 0–56.77 mbsf, Hole U1486C = 0–57.55 mbsf, Hole U1486D = 0–58.025 mbsf

Thickness: Hole U1486A = 9.95 m (minimum thickness), Hole U1486B = 56.77 m, Hole U1486C = 57.55 m, Hole U1486D = 58.025 m

Age: late early Pleistocene to recent

Lithology: foraminifer and clay-rich nannofossil ooze, clay-bearing foraminifer-rich nannofossil ooze, clay-rich nannofossil ooze, ashy sand, and ash

Figure F9. Characteristic lithology, color alternations, and boundary between Subunits IA and IB (red line), Core 363-U1486B-7H.

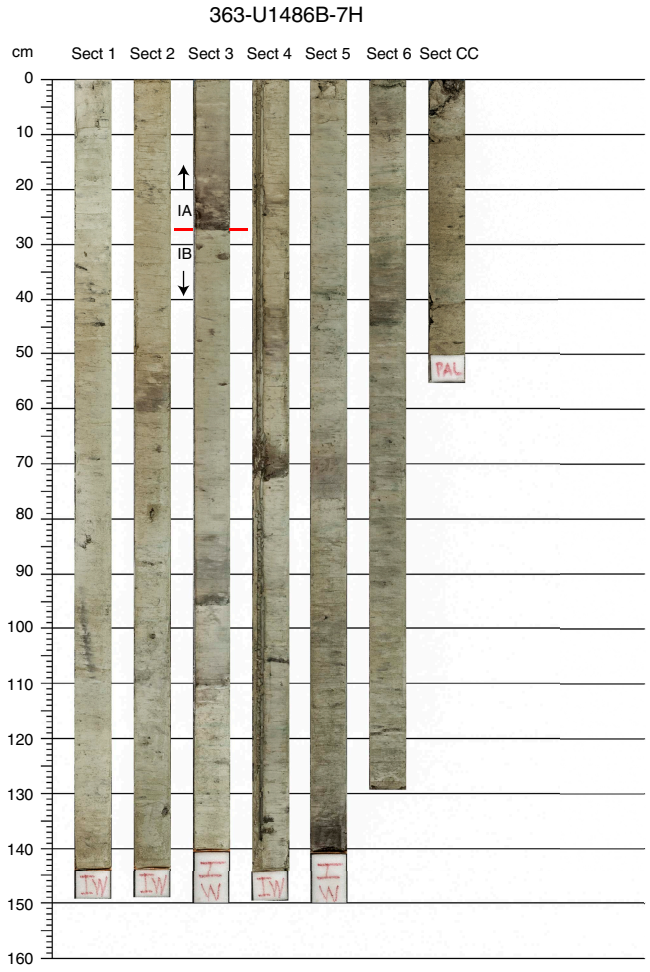

The top of this subunit includes the mudline, characterized by a prominent change in color from reddish brown to light greenish gray at ~5 cm, with the sediment composed of abundant foraminifers, nannofossils, siliceous microfossils, and clay (Figure **F7A**). The primary lithology of Subunit IA is nannofossil ooze mixed with variable amounts of clay minerals and foraminifers as well as other components including silt-sized volcanic shards and, less frequently, silt-sized siliciclastics and glauconite. Biosilica is also present, generally in trace amounts, and is derived from the skeletal parts of radiolarians, diatoms, and silicoflagellates in decreasing order of abundance. Fragments of pteropod shells were also observed in the upper ~3.5 mbsf.

The color of the subunit is dominantly greenish gray (~10GY 7/1); this subunit shows the highest luminosity (L*) reflectance (Figure **F5**). The darker sediment corresponds to intervals that have higher clay mineral or volcanogenic particle content. The brightest sediment (highest L* values) occurs between ~6 and 25 mbsf and is concentrated in the middle part of the subunit at ~21 mbsf (e.g., Core 363-U1486B-3H), which consists mainly of foraminifer-rich nannofossil ooze.

Subunit IA has higher NGR than the other subunits, probably reflecting the higher clay content in the sediment. It also shows relatively low magnetic susceptibility values, in contrast to the deeper subunits characterized by higher concentrations of volcanic glass (Figure **F5**). Layers with volcanogenic sediment become more abundant below ~21 mbsf. These layers are a few centimeters thick, light brown and dark gray in color, and exhibit higher NGR and gamma ray attenuation (GRA) bulk density than the background sediment (see **Physical properties**).

The boundary with Subunit IB is placed at the base of the first black tephra layer at intervals 363-U1486B-7H-3, 27 cm (56.77 mbsf), 363-U1486C-8H-6, 75 cm (57.55 mbsf), and 363-U1486D-7H-7, 32.5 cm (58.025 mbsf). The occurrence of tephra layers increases downhole below these depths, and the color of the sediment is darker than in Subunit IA (Figure **F9**).

Subunit IB

Intervals: 363-U1486B-7H-3, 27 cm, through 16H-2, 70 cm; 363-U1486C-8H-6, 75 cm, through 17H-5, 25 cm; 363-U1486D-7H-7, 32.5 cm, through 16H-6, 17.5 cm
Depths: Hole U1486B = 56.77–141.20 mbsf, Hole U1486C = 57.55–141.05 mbsf, Hole U1486D = 58.025–143.375 mbsf
Thickness: Hole U1486B = 84.43 m, Hole U1486C = 83.50 m, Hole U1486D = 85.35 m
Age: early Pleistocene
Lithology: foraminifer- and ash-rich nannofossil clay, ashy sand, and ash

The main lithology in Subunit IB is nannofossil ooze mixed with variable amounts of glass shards and foraminifers, as well as clay minerals. Coarser grained, silt- to fine sand-sized layers are also present. The particles in these layers are mainly composed of lighter colored and transparent volcanic glass and darker/opaque scoria fragments. Both volcanogenic components occur mixed with foraminifers and/or feldspars and variable amounts of clay. As observed for Subunit IA, biosilica (mainly radiolarians and diatoms) is present in variable amounts but always less than ~10% (Figure **F7B**). This subunit is characterized by higher magnetic susceptibility and lower NGR and L* than Subunit IA (Figure **F5**). The higher abundance of volcanic glass, the presence of volcanic scoria, and lower clay mineral content account for these physical property variations.

The first downhole appearance of black ash layers (few centimeters thick) entirely composed of volcanic glass (tephras) marks the boundary with Subunit IA (see **Subunit IA**); they become more common downhole (Figure **F9**). The tephra layers are spaced at intervals between 10 and 50 cm over several sections producing a prominent dark–light alternation in the sediment color. The base of these alternations typically starts with a black tephra layer, which has a sharp contact with the underlying light-colored hemipelagic sediment, followed by a gradual transition from darker to lighter colors due to mixing by bioturbation. The upper part of these cycles is composed of the background hemipelagic sediment, which dominates until the next tephra appears.

Generally, felsic, nonpleochroic volcanic glasses are the most abundant volcanogenic particle type found in the ash layers of Subunit IB (Figure **F12A**). Pumice fragments ranging from pebble sized to a few millimeters are also present (Figure **F13A**).

The base of the subunit coincides with the top of a prominent black volcanic ash layer that corresponds to a significant jump in magnetic susceptibility at 363-U1486B-16H-2, 70 cm (141.20 mbsf), 363-U1486C-17H-5, 25 cm (141.05 mbsf), and 363-U1486D-

Figure F10. A–E. Physical property data indicating different styles of alternation between volcanogenic and hemipelagic sediment. Arrows = intervals discussed in text. cps = counts per second.

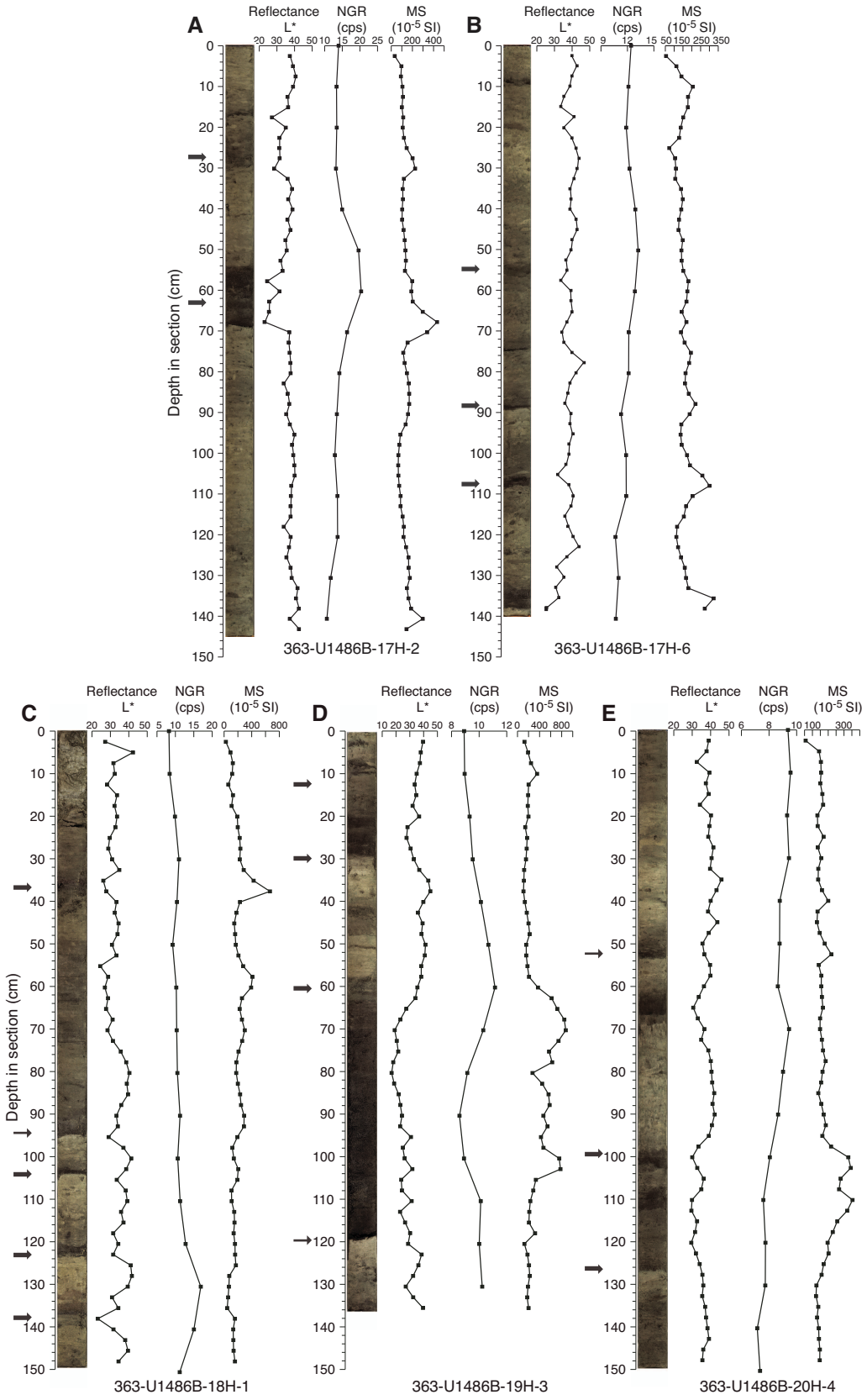

Figure F11. Basalt fragments found at the bottom of Hole U1486B (23H-CC, 0–8 cm). Green, rounded olivine crystals and black prismatic pyroxenes can be observed on both the (A, C) photographs and (B, D) photomicrographs.

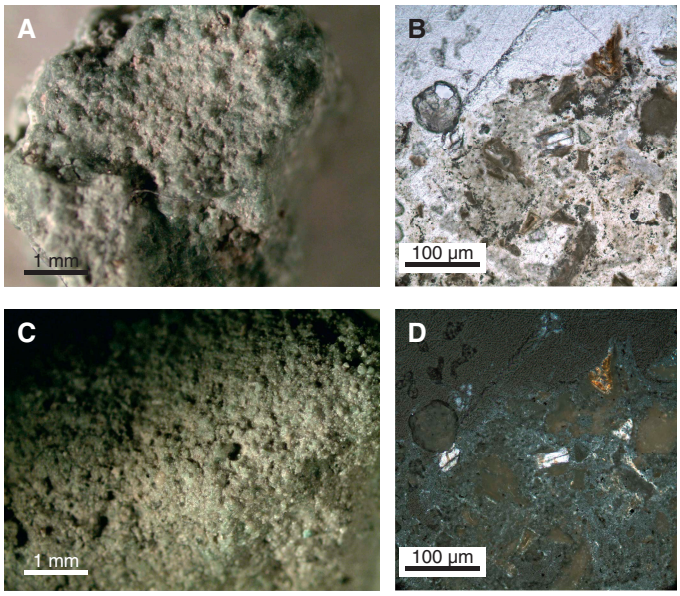

Figure F12. SEM photomicrographs of selected tephra layers, Site U1486. A. Vesicular glass fragments. B. Bubble wall shards. C. Micropumice.

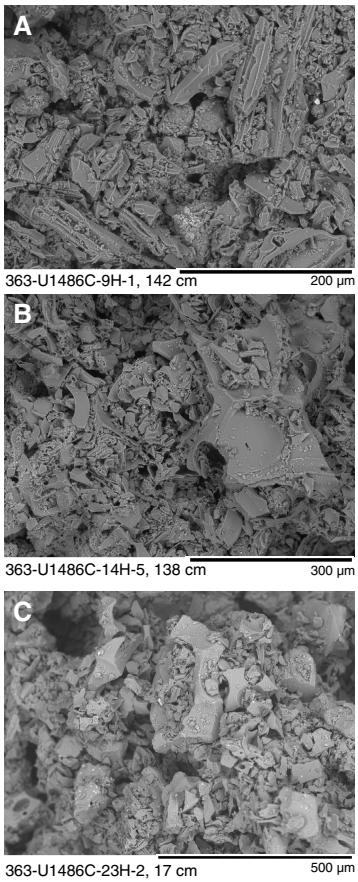

Figure F13. SEM photomicrographs of selected pumice samples, Site U1486. A. Elongate coalescing vesicles. B. Spherical vesicles.

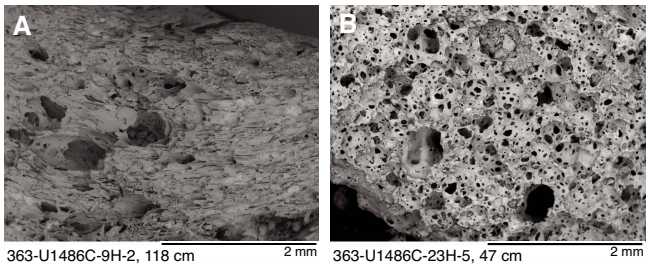

16H-6, 17.5 cm (143.375 mbsf). Below these depths, magnetic susceptibility values are higher, and the sediment is darker (lower L*) (Subunit IC; Figure **F5**).

Subunit IC

Intervals: 363-U1486B-16H-2, 70 cm, through 23H-CC, 8 cm; 363-U1486C-17H-5, 25 cm, through 23H-CC, 29 cm; 363-U1486D-16H-6, 17.5 cm, through 19H-CC, 24 cm
Depths: Hole U1486B = 141.20–211.17 mbsf, Hole U1486C = 141.05–200.98 mbsf, Hole U1486D = 143.375–186.75 mbsf
Thickness: Hole U1486B = 69.97 m, U1486C = 59.93 m, U1486D = 43.375 m
Age: late Pliocene to early Pleistocene
Lithology: foraminifer- and ash-rich nannofossil clay, ashy sand, and ash

The main components of Subunit IC are silt- to fine sand-sized volcanogenic particles mainly composed of dark scoria fragments and brown volcanic glass. The volcanogenic material occurs in discrete layers and beds ranging from a few centimeters to >50 cm (Figure **F10**). Volcanic glass and scoria also occur mixed with the biogenic component, which consists of foraminifer-rich nannofossil clay (Figure **F6E, F6F**). Biosilica is also present and the clay mineral content is variable, although generally lower than in the upper two subunits. Subunit IC is characterized by the highest magnetic susceptibility, lowest NGR (which shows a clear decreasing trend downhole), and lowest L* values (Figure **F5**) and the darkest sediment recovered at this site. The changes in physical properties and L* reflect the high abundance of volcanic scoria compared with the biogenic component and a lower clay mineral content compared with the younger part of the sediment record.

Figure **F10** shows different geometries of the volcanogenic layers in Subunit IC as observed during core description. High-resolution digital line-scan images are compared with the magnetic susceptibility, L*, and NGR to highlight differences in composition and depositional style among the different types of volcanogenic deposits. In Figure **F10A**, a layer between 54 and 68 cm containing abundant volcanogenic material is clearly identified by lower luminosity (L*) and higher magnetic susceptibility toward the base of this interval. The layer shows a sharp and slightly undulated basal contact, and magnetic susceptibility decreases and NGR (a proxy for clay minerals) increases toward the top. Together with the results of smear slide analyses, this suggests that the layer was either resedimented (i.e., not directly deposited from a pyroclastic event as is typical for tephra layers) or was bioturbated toward the top. In the

Figure F14. Lithologies and authigenic minerals in the hydrothermally altered interval at the base of Site U1486. A. Core images. B. Microgranular aspect of zeolites (PPL). C. XRD of the zeolite (arrows = variety mordenite). WL = wavelength.

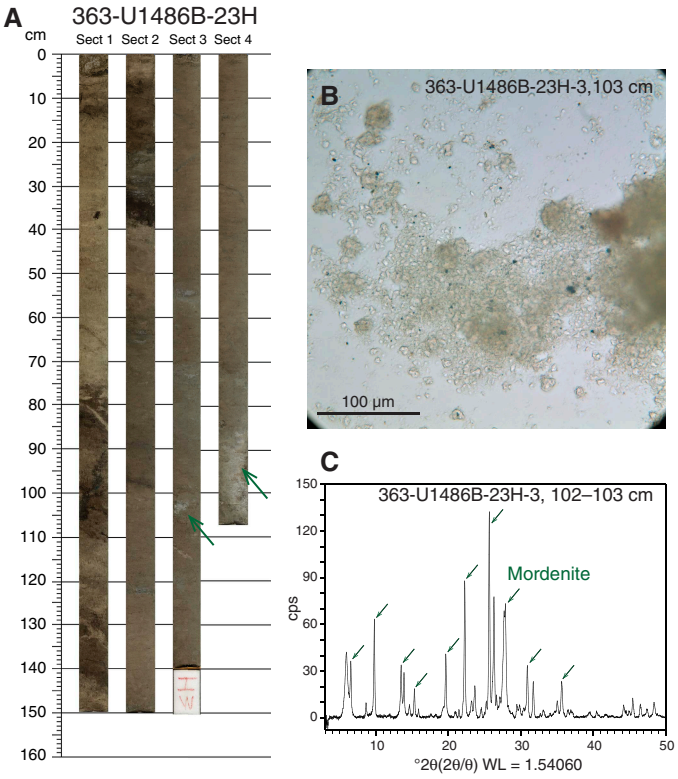

same core section, the dark layer at ~30 cm has higher magnetic susceptibility, low NGR, and lower L*, which may indicate that it is solely composed of volcanic glass (tephra). Similarly, most dark layers in Figures **F10B** and **F10C** show sharp contacts at the base and a gradual transition to lighter colors and lower magnetic susceptibility values toward the top.

Resedimentation by either mass gravity deposition or bottom current reworking combined with bioturbation is a possible explanation for some of the thicker (>2–3 cm), mainly volcanogenic layers observed at Site U1486, which in Subunit IC are particularly abundant. For instance, the layer between ~120 and 60 cm in Figure **F10D** and the dark layer between ~125 and 100 cm in Figure **F10E** have a sharp base and higher NGR at both the base and top, whereas magnetic susceptibility is highest toward the top. The low L* interval between ~125 and 100 cm in Figure **F10E** corresponds to the depth of the Matuyama/Brunhes boundary, which is dated to 2.581 Ma (see **Paleomagnetism**).

The bottom sections of Subunit IC (~207–211 mbsf; e.g., Sections 363-U1486B-23H-2, 23H-3, and 23H-4) are pervaded by a whitish, microcrystalline, mainly cemented zeolite (variety mordenite; Ca and/or Na dominated) (Figure **F14**). In smear slides, the mordenite crystals appear subhedral to ragged, small, platy, and fine grained (2–45 µm). They are transparent and colorless, show moderate relief, weak birefringence, and no pleochroism. The sediment at the base of the succession also contains angular to subangular centimeter-scale fragments of greenish gray rocks that are particularly common in the core catcher of the last two cores from Hole U1486B (Cores 363-U1486B-22H and 23H). Some of the fragments were collected for thin sections and observed under a petrographic microscope. The rock is basalt with small olivine and pyroxene phenocrysts (Figure **F11**).

Discussion

Volcanogenic sediment

Volcanic glass in marine sediment occurs in the form of shards and fragments that result from explosively erupted pumice, rapid quenching of molten lava, or through the erosion of glassy rocks such as pumice or scoria. Volcanic glass may also originate during submarine volcanic eruptions through the granulation of pillow rims or during subaerial eruptions as a result of ash fallout through the water column (tephra layers; Rothwell, 1989).

Glass shards can show a variety of morphologies and size ranges between fine silt (~10 µm) to medium sand (~500 µm). Generally, felsic glass (e.g., derived from volcanic arc magmatism) are colorless, whereas darker glass tends to be more mafic (e.g., derived from basalts). Volcanic glass is inherently unstable and devitrifies over time. Glass of different compositions will hydrate and devitrify differently, with the most important products of alteration being palagonite, smectite, and zeolites (Rothwell, 1989).

As discussed in **Unit description**, volcanogenic sediment is observed throughout the succession at Site U1486 but is most abundant in Subunit IB and especially Subunit IC, where it makes up the bulk of the sediment. In both Subunits IB and IC, the volcanogenic component occurs in well-defined tephra layers that often recur at intervals of several tens of centimeters (e.g., Figure **F10C**). However, in Subunit IC, thicker (>>2–3 cm) volcanogenic layers are also common (e.g., Figure **F10D, F10E**). Visual core description, smear slide analysis, and comparison with physical property data suggest that several of these thicker layers were the product of resedimentation by either mass gravity deposition or bottom current reworking.

In Hole U1486B, we identified ~185 distinct tephra layers. However, this is probably an underestimate because bioturbation has disrupted several of the thinner tephra layers. Overall, the tephra layers increase in abundance and thickness downhole. Added together, the thickness of the tephra layers is >20 m, which is ~10% of the core recovery.

Sediment generally darkens downhole, and the base of Subunit IC is distinctively darker than that of Subunit IA (Figure **F5**). Light gray (N 7) tephras (e.g., interval 363-U1486C-9H-1, 142 cm) commonly consist of micropumice with elongate vesicles and vesicular glass fragments. Dark brown (7.5YR 3/2) tephras (e.g., interval 363-U1486C-14H-5, 138 cm) are composed of bubble wall shards. Very dark gray (N 3) tephras (e.g., interval 363-U1486B-23H-2, 17 cm) are composed of microscoria and vesicular glass fragments (Figures **F12**, **F13**). Pumice vesicles (e.g., interval 363-U1486C-9H-2, 118 cm) show parallel and elongate shapes with secondary elongate coalescing vesicles, whereas scoria vesicles (e.g., interval 363-U1486C-23H-5, 47 cm) exhibit spherical shape with secondary spherical coalescing vesicles (Figure **F13**).

Hydrothermal reactions and sediment/basalt interface

Zeolites (variety mordenite) are found near the base of Hole U1486B (Figure **F14**). Zeolites are a group of basic, hydrous minerals that possess an open aluminosilicate framework structure containing channels filled with water molecules and cations. The increase in chlorinity in the lower ~70 m at this site might be a con-

sequence of the hydration of zeolites (see **Geochemistry**). The occurrence of cementation by mordenite coincides with anomalously high *P*-wave velocity and low bulk density (see **Physical properties**). Zeolites are produced by different geological mechanisms (e.g., magmatism, metamorphism, burial diagenesis, and weathering) and as precipitates in marine sediment. However, mordenite is mainly found associated with submarine hydrothermal activity (Iijima, 1980). Hydrothermal activity is also supported by the very low heat flow gradient measured at this site with the APCT-3 (see **Physical properties**).

Evolution of sedimentation

Sedimentation at Site U1486 started in the late Pliocene (~2.7 Ma; see **Biostratigraphy**). The presence of both subrounded and angular fragments of basaltic rocks and hydrothermal activity at the bottom of the recovered succession suggests that sedimentation occurred directly above basaltic crust that was hydrothermally active at least during deposition of the lower ~4 m of sediment. Basaltic volcanism is recorded mainly in Subunit IC (over a period of ~500 ky; see **Biostratigraphy**) and part of Subunit IB by the presence of mafic volcanic glass and scoria. The very high sedimentation rates recorded in Subunit IC are probably the result of the remobilization and rapid deposition through mass gravity mechanisms of pyroclastic material temporarily deposited in subaerial and other submarine areas.

This regime dominated by mafic volcanism and very rapid sedimentation by mass gravity flows continued until ~2 Ma (the top of Subunit IC), which marks the cessation of the basaltic magmatism and/or the lack of delivery of basaltic-type volcanogenic material to the depositional basin of Site U1486. The volcanogenic sediment observed in Subunit IB is mainly clear volcanic glass and pumice, indicating a possible origin from more felsic sources of explosive magmatism, such as volcanic arcs.

The onset of deposition of Subunit IA, at ~1 Ma, records the dominance of hemipelagic (biogenic and clay minerals) components over the volcanogenic material. The increase in clay minerals that occurs throughout both Subunits IA and IB indicates an increased terrigenous influence during deposition of these subunits.

Biostratigraphy

At Site U1486, a 206 m thick succession of nannofossil ooze, ash, and clay, silt, and sand with varying proportions of nannofossils, foraminifers, and radiolarians was recovered (see **Core description**). Planktonic foraminifers, benthic foraminifers, and calcareous nannofossils are always present and generally excellently preserved, although a slight decrease in preservation state is noted in the lowermost two cores of Hole U1486B (see **Foraminifer preservation**). The results from each fossil group (calcareous nannofossils, planktonic foraminifers, and benthic foraminifers) are presented below, followed by a detailed characterization of both benthic and planktonic foraminifer preservation state using shipboard light microscope and scanning electron microscope (SEM) observations. An integrated bio- and magnetostratigraphy is presented in the final section. Shipboard taxon occurrence data are available to download from the Laboratory Information Management System (LIMS) database (**http://web.iodp.tamu.edu/LORE**).

Calcareous nannofossils

Calcareous nannofossil biostratigraphy is primarily based on analysis of core catcher (CC) samples and two or three additional samples per core from working-half sections in Hole U1486B, providing a sampling resolution of ~3 m. In the deepest part of the hole, the sediment samples were sieved at 20 µm to remove coarser ash particles prior to making smear slides. Depth positions and age estimates of key biohorizons are given in Table **T2**. Observations were undertaken using plane- (PPL), cross- (XPL), and circular-polarized light (CPL), as well as the shipboard desktop SEM (Hitachi TM3000) to confirm the presence of *Emiliania huxleyi* and to check preservation state. Bioevent/biohorizon abbreviations in the text follow those in the caption of Table **T2**.

At Site U1486, the preservation of calcareous nannofossils is generally excellent to very good (Figure **F15**). Dissolution-susceptible taxa are consistently present throughout the recovered interval (*Syracosphaera, Oolithotus fragilis, Tetralithoides symeonidesii*, and *Calciosolenia* sp.). Very small *Reticulofenestra minuta, Gephyrocapsa* spp., and *Emiliania huxleyi* are abundant and well preserved (SEM/CPL). Reworked calcareous nannofossils are very rare through the succession, consisting of occasional specimens of *Sphenolithus abies* and one specimen of *Reticulofenestra pseudoumbilicus*. Although not significant in the assemblages, this does indicate the transport of sediments derived from strata older (~early Pliocene) than those recorded at the base of the hole (latest Pliocene), just above acoustic basement.

Calcareous nannofossil assemblages from Pleistocene sediments at Site U1486 show high diversity. The main components are

Table T2. Calcareous nannofossil bioevents, Site U1486. B = base, T = top, Bc = base common, Ba = base acme, Ta = top acme. **Download table in CSV format.**

Bioevent number	Marker species	Age (Ma)	Zone base	Top core, section, interval (cm)	Bottom core, section, interval (cm)	Top depth (mbsf)	Bottom depth (mbsf)	Midpoint depth (mbsf)	± depth (mbsf)
				363-U1486B-	363-U1486B-				
1	Bc *Emiliania huxleyi*	0.09		1H-CC	2H-3, 50	5.94	9.50	7.72	1.78
2	Ta *Gephyrocapsa caribbeanica*	0.28		3H-3, 20	3H-5, 100	18.65	22.35	20.50	1.85
3	B *Emiliania huxleyi*	0.29	NN21	3H-3, 20	3H-5, 100	18.65	22.35	20.50	1.85
4	T *Pseudoemiliania lacunosa*	0.44	NN20	4H-3, 50	4H-4, 50	28.50	31.50	30.00	1.50
5	Ba *Gephyrocapsa caribbeanica*	0.56		4H-CC	5H-2,75	35.05	36.75	35.90	0.85
6	T *Reticulofenestra asanoi*	0.91		6H-CC	7H-2, 120	53.88	56.20	55.04	1.16
7	Bc *Reticulofenestra asanoi*	1.14		9H-CC	10H-2, 100	82.47	84.50	83.49	1.02
8	T *Gephyrocapsa* >5.5 µm	1.25		8H-5, 130	8H-CC	70.30	72.79	71.55	1.25
9	T *Helicosphaera sellii*	1.26		9H-CC	10H-2, 100	82.47	84.50	83.49	1.02
10	T *Calcidiscus macintyrei*	1.60		11H-2, 120	11H-4, 120	94.20	97.20	95.70	1.50
11	T *Discoaster brouweri*	1.93	NN19	13H-4, 110	13H-6, 67	116.36	118.67	117.52	1.16
14	T *Discoaster pentaradiatus*	2.39	NN18	18H-4, 21	18H-6, 21	162.71	165.71	164.21	1.50
15	T *Discoaster surculus*	2.49	NN17	20H-2, 85	20H-4, 85	179.35	182.35	180.85	1.50

Figure F15. Calcareous nannofossils, Hole U1486B. A. *Calcidiscus leptoporus* (12H-CC). B, C. *Calcidiscus macintyrei;* (B) 12H-CC; (C) 19H-CC. D, E. *Coccolithus pelagicus* (15H-CC). F. *Cruciplacolithus neohelis* (15H-CC). G, H. *Discoaster brouweri* (22H-6, 81 cm). I. *Discoaster surculus* (20H-6, 85 cm). J. *Discoaster* sp. (22H-6, 81 cm). K. *Emiliania huxleyi* (1H-CC). L. *Gephyrocapsa* sp. >5.5 µm (8H-CC). M. *Gephyrocapsa oceanica* and *Gephyrocapsa caribbeanica* (4H-CC). N. *Gephyrocapsa oceanica* (2H-CC). O. *G. caribbeanica* (arrows) (4H-3, 50 cm). P. Small *Gephyrocapsa* sp. (arrows) (10H-CC). Q. *Helicosphaera carteri* (10H-CC). R. *Helicosphaera princei* (9H-CC). S. *Helicosphaera sellii* (10H-CC). T, U. *Pontosphaera* spp.; (T) 5H-CC; (U) 20H-CC. V. *Pontosphaera japonica* (1H-CC). W. *Pontosphaera discopora* (1H-CC). X. *Pontosphaera* cf. *P. alta* (12H-CC). Y, Z. *Pseudoemiliania lacunosa*; (Y) 8H-3, 130 cm; (Z) 7H-4, 120 cm. AA. *Reticulofenestra asanoi* (10H-6, 100 cm). AB. *Scyphosphaera pulcherrima* (13H-CC). AC. *Umbilicosphaera sibogae* coccosphere (1H-CC). AD. Coccosphere (19H-CC). A, C–F, L–U, X, Z, AA, and AB: XPL; B, K, V, W, Y, AC, and AD: CPL; G–J: PPL. All photos are at same magnification (scale bar in A).

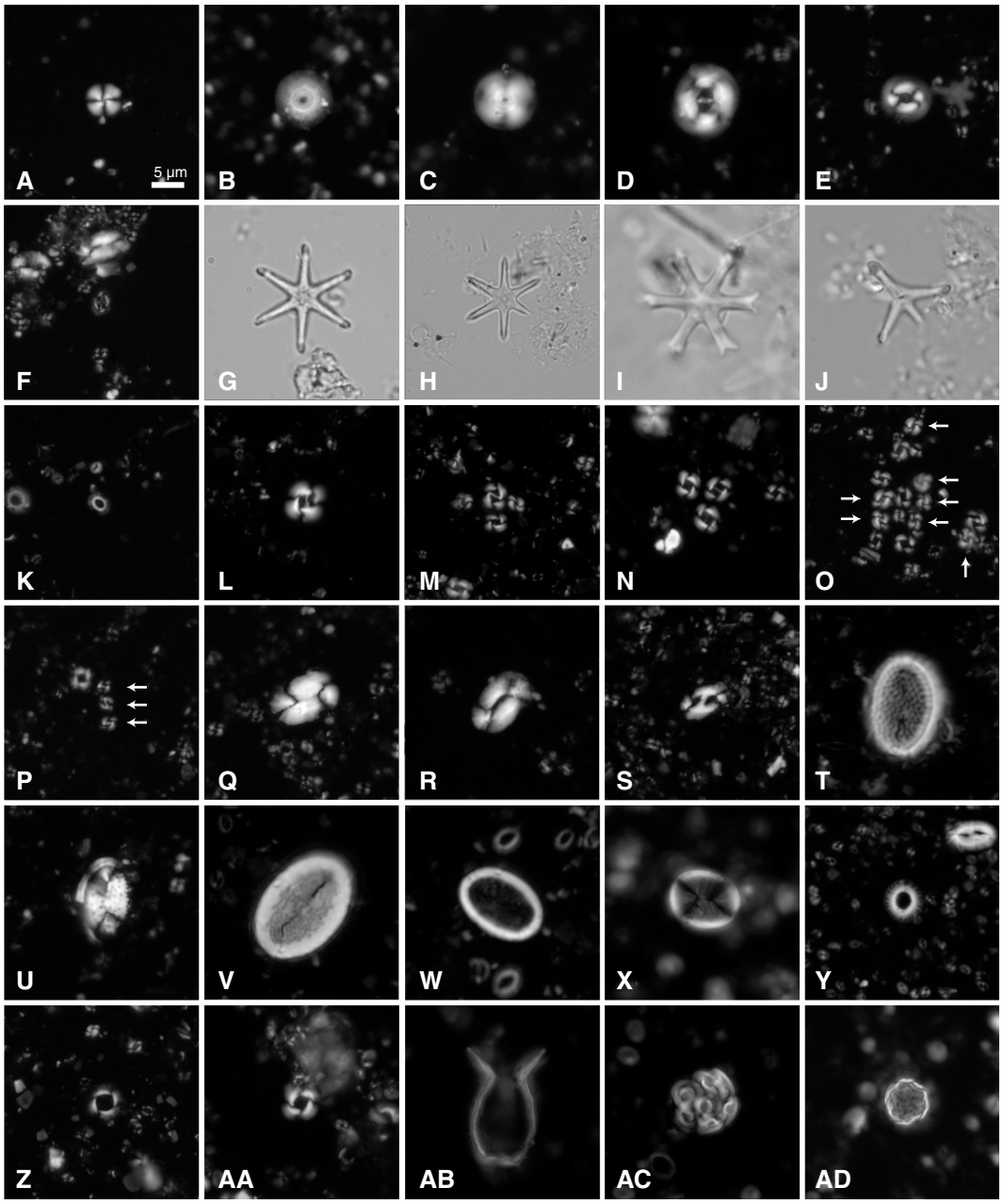

Florisphaera profunda and members of the Noelaerhabdaceae family (genera include *Gephyrocapsa, Emiliania, Pseudoemiliania*, and *Reticulofenestra*), but with significant additional diversity from the Calcidiscaceae as well as *Helicosphaera, Rhabdosphaera, Pontosphaera*, and *Syracosphaera* species. The distribution of the main taxa through the Pleistocene is shown in Table **T3**.

Biohorizon base common *E. huxleyi* (0.09 Ma) occurs between Samples 363-U1486B-1H-CC and 2H-3, 50 cm (5.94–9.50 mbsf).

Table T3. Distribution of selected calcareous nannofossil species, Hole U1486B. **Download table in CSV format**.

The base of Zone NN21 is identified by biohorizon base *E. huxleyi* (0.29 Ma) between Samples 3H-3, 20 cm, and 3H-5, 100 cm (18.65–22.35 mbsf). The base of Zone NN20 is identified by biohorizon top *Pseudoemiliania lacunosa* (0.44 Ma) between Samples 4H-3, 50 cm, and 4H-4, 50 cm (28.50–31.50 mbsf). Biohorizon base acme *G. ca-*

ribbeanica (0.56 Ma) occurs between Samples 4H-CC and 5H-2, 75 cm (35.05–36.75 mbsf). Below this level, in Sample 6H-CC (53.88 mbsf), medium-sized *Gephyrocapsa* are still dominant but are distinct from *G. caribbeanica* based on the shape of their collar. It is not clear whether this slightly older morphotype is equivalent to the medium-sized *Gephyrocapsa* (>4 µm) of Raffi and Flores (1995) or *Gephyrocapsa omega* or other taxonomic concepts of *G. caribbeanica*. Biohorizon top *Gephyrocapsa* >5.5 µm, which is based strictly on coccolith size (e.g., Raffi and Flores, 1995), is difficult to place accurately at this site, as, in general, the size of *Gephyrocapsa* coccoliths is smaller (<5 µm) than in other Pleistocene successions (e.g., in ODP Leg 138; Raffi and Flores, 1995). Biohorizon top *Gephyrocapsa* >5.5 µm (1.25 Ma) is placed between Samples 8H-5, 130 cm, and 8H-CC (70.3–72.79 mbsf) based on the occurrence of *Gephyrocapsa* >5.5 µm in one sample (8H-CC; 72.79 mbsf). Below this level, medium to large *Gephyrocapsa* (~4.5–5.5 µm) are present down to Sample 11H-2, 120 cm (94.20 mbsf).

The base of Zone NN19 is identified by biohorizon top *Discoaster brouweri* (1.93 Ma) between Samples 363-U1486B-13H-4, 110 cm, and 13H-6, 67 cm (116.36–118.67 mbsf). Within Sample 13H-6, 67 cm, well-preserved *D. brouweri* are present at very low abundance, but they disappear below this level until Sample 14H-CC (129.93 mbsf). This species is then present in fluctuating abundance (present to frequent) in Core 15H, only becoming common and continuously present downhole within Core 16H. This is taken as a true pattern of *D. brouweri* abundance fluctuation at this location based on the preservation state of the specimens observed.

The base of Zone NN18 is placed at biohorizon top *Discoaster pentaradiatus* (2.39 Ma) between Samples 363-U1486B-18H-4, 21 cm, and 18H-6, 21 cm (162.71–165.71 mbsf). Biohorizon top *Discoaster surculus* (2.49 Ma) is the last biohorizon recorded downhole and marks the base of Zone NN17 between Samples 20H-2, 85 cm, and 20H-4, 85 cm (179.35–182.35 mbsf).

Planktonic foraminifers

Planktonic foraminifer biostratigraphy was conducted on Hole U1486B. Above ~82.5 mbsf (Cores 363-U1486B-1H through 9H; 5.94–82.47 mbsf), we examined core catcher samples only, resulting in a sampling resolution of ~9.5 m. Below ~82.5 mbsf (Cores 10H through 23H; 84.49–211.09 mbsf), three additional samples per core were taken, typically from Sections 2, 4, and 6, although in shorter cores fewer additional samples were taken. This resulted in a sampling resolution of ~2.5 m. A list of biohorizons is given in Table **T4**. Coiling direction counts on *Pulleniatina* are given in Table **T5** and plotted in Figure **F16**.

Sample 363-U1486B-1H-CC (5.94 mbsf) is assigned to the uppermost part of Subzone Pt1b (<0.07 Ma) based on the absence of *Globorotalia flexuosa* and *Globigerinoides ruber* (pink). Biohorizons top *G. flexuosa* (0.07 Ma) and top *G. ruber* (pink) (0.12 Ma) are both observed between Samples 1H-CC and 2H-CC (5.94–16.01 mbsf).

Biohorizons base *Globigerinella calida* and base *G. flexuosa* are problematic for several reasons: (1) both require careful taxonomic discrimination; (2) reasonably large populations need to be examined when the forms are rare so that a biohorizon must sometimes be located with just one or two taxonomically marginal specimens in a sample, which becomes more problematic with sparse downhole resolution based only on core catcher samples; and (3) convergent morphologies of both forms reappear further downhole. For instance, well-developed morphologies similar to *G. calida* with characteristic radially elongated final chambers (compared to co-occurring ancestor *Globigerinella siphonifera*) occur down to Sample 363-U1486B-14H-CC (129.93 mbsf), and morphologies similar to *G. flexuosa* are common in the Pliocene down to Sample 20H-CC (186.95 mbsf), as was found at other Expedition 363 sites (see **Biostratigraphy** in the Site U1484 chapter and **Biostratigraphy** in the Site U1485 chapter [Rosenthal et al., 2018d, 2018e]). Some of the issues surrounding *G. calida* in particular might be clarified in the light of recent research (Weiner et al., 2015), which distinguished two genetically and morphologically distinct populations in the modern ocean that have previously been grouped as *G. calida*, namely *Globigerinella calida* (Parker) sensu stricto and *Globigerinella radians* (Egger). At Site U1486 we attempted to distinguish *G. radians* from *G. calida* for the first time during Expedition 363. We found that both forms are present in the sediment and appear to have similar stratigraphic distributions in the upper two cores, although much more detailed work is required postexpedition to fully investigate this. For biostratigraphic purposes we assume that in stratigraphically much lower samples, morphologies that are recorded as "*calida*" and "*flexuosa*" in our preliminary occurrence tables can be ascribed to evolutionary convergence and are excluded from consideration. Hence, we were able to tentatively identify biohorizon base *G. calida* (0.22 Ma) between Samples 2H-CC and 3H-CC (16.01–25.37 mbsf) and biohorizon base *G. flexuosa* (0.40 Ma) between Samples 3H-CC and 4H-CC (25.37–35.05 mbsf).

Table T4. Planktonic foraminifer bioevents, Site U1486. * = calibration follows Dowsett (1988). B = base, T = top. **Download table in CSV format.**

Bioevent number	Marker species	Age (Ma)	Zone base	Top core, section, interval (cm)	Bottom core, section, interval (cm)	Top depth (mbsf)	Bottom depth (mbsf)	Midpoint depth (mbsf)	± depth (mbsf)
				363-U1486B-	363-U1486B-				
1	T *Globorotalia flexuosa*	0.07		1H-CC	2H-CC	5.94	16.01	10.98	5.04
2	T *Globigerinoides ruber* (pink)	0.12		1H-CC	2H-CC	5.94	16.01	10.98	5.04
3	B *Globigerinella calida*	0.22		2H-CC	3H-CC	16.01	25.37	20.69	4.68
4	B *Globorotalia flexuosa*	0.40		3H-CC	4H-CC	25.37	35.05	30.21	4.84
6	T *Globorotalia tosaensis*	0.61	Pt1b	6H-CC	7H-CC	53.88	62.81	58.35	4.46
11	T *Globigerinoidesella fistulosa*	1.88	Pt1a	11H-4, 119–121	11H-6, 119–121	97.19	100.19	98.69	1.50
14	B *Pulleniatina finalis*	2.04		14H-6, 93–95	14H-CC	128.43	129.93	129.18	0.75
17	T *Globorotalia pseudomiocenica*	2.30	PL6	14H-6, 93–95	14H-CC	128.43	129.93	129.18	0.75
18	T *Globorotalia limbata*	2.39		14H-6, 93–95	14H-CC	128.43	129.93	129.18	0.75
12	B *Globorotalia truncatulinoides*	2.47*		22H-4, 80–82	22H-6, 80–82	201.30	204.30	202.80	1.50

Table T5. *Pulleniatina* coiling count data, Hole U1486B. **Download table in CSV format**.

Figure F16. Coiling patterns in *Pulleniatina*, Hole U1486B.

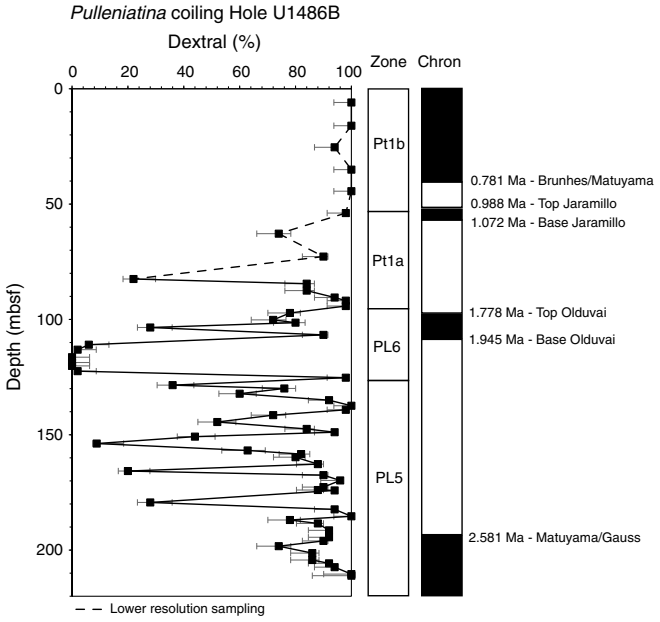

Biohorizon top *Globorotalia tosaensis* (0.61 Ma) demarcates the base of Subzone Pt1b and is observed between Samples 363-U1486B-6H-CC and 7H-CC (53.88–62.81 mbsf). The L1 coiling change in *Pulleniatina* from "random" coiling to predominantly dextral individuals (0.80 Ma) cannot be located reliably because of the low sampling resolution (Figure **F16**).

The base of Zone Pt1, defined by biohorizon top *Globigerinoidesella fistulosa* (1.88 Ma according to the Atlantic Ocean calibration at ODP Site 925 of Chaisson and Pearson, 1997), is observed between Samples 363-U1486B-11H-4, 119–121 cm, and 11H-6, 119–121 cm (97.19–100.19 mbsf). Unlike in the Atlantic site where *G. fistulosa* disappears gradually uphole, with only poorly developed forms below the extinction level (Chaisson and Pearson, 1997), at Site U1486 there are well-developed *G. fistulosa* in the highest sample in which they are present. The age of this biohorizon in the Pacific Ocean may represent the true extinction of *G. fistulosa* after its local disappearance from the Atlantic Ocean (Resig et al., 2001) and needs careful recalibration.

Three biohorizons are observed between Samples 363-U1486B-14H-6, 93–95 cm, and 14H-CC (128.43–129.93 mbsf):

1. Biohorizon base *Pulleniatina finalis* (2.04 Ma);
2. Biohorizon top *Globorotalia pseudomiocenica* (2.30 Ma), which marks the base of Zone PL6; and
3. Biohorizon top *Globorotalia limbata* (2.39 Ma).

With no sedimentological evidence of reworking or hiatuses (see **Core description**) and apparently continuous calcareous nannofossil biostratigraphy (see **Calcareous nannofossils**) in this interval, it seems most likely that the close association of these bioevents in time is real and consequently that they are not well calibrated in the Indo-Pacific region. Moreover, the events were found to be closely associated at several other Expedition 363 sites (see **Biostratigraphy** in the Site U1482 chapter, **Biostratigraphy** in the Site U1483 chapter, **Biostratigraphy** in the Site U1487 chapter, and **Biostratigraphy** in the Site U1490 chapter [Rosenthal et al., 2018b, 2018c, 2018f, 2018g]). The biochronologic age for biohorizon top *G. limbata* is based on an Atlantic Ocean calibration from ODP Site 925 (Chaisson and Pearson 1997). The age for biohorizon top *G. pseudomiocenica* can be sourced to Berggren et al. (1995) where no other calibration information is provided other than the age of 2.30 Ma, except that the extinction is regarded as likely coeval with the extinction of the similar species *Globorotalia miocenica* in the Atlantic Ocean. This highlights the need for better calibrations in the Pacific Ocean and renewed study of the extent of diachrony and species provincialism between ocean basins.

A series of coiling reversals in *Pulleniatina* occurs in Hole U1486B (Figure **F16**), which have the potential for more detailed correlation to other sites including nearby Site U1487, Indian Ocean Sites U1482 and U1483, and elsewhere (e.g., offshore Papua New Guinea sites from ODP Leg 180 studied by Resig et al., 2001).

Biohorizon base *Globorotalia truncatulinoides* (2.47 Ma according to the regional calibration of Dowsett, 1988) was tentatively placed between Samples 363-U1486B-22H-4, 80–82 cm, and 22H-6, 80–82 cm (201.30–204.30 mbsf). At the bottom of Hole U1486B, the sediment particles in Sample 23H-CC (211.09) are dominated by volcanic fragments, but planktonic foraminifers are still present in sufficient abundance to establish the biostratigraphic zone and approximate age. *Pulleniatina* is exclusively dextral. Well-developed *G. fistulosa* is found in the absence of *G. truncatulinoides* and *Dentoglobigerina altispira*, indicating an age in the range of 2.47–3.33 Ma within Zone PL5.

Table T6. Benthic foraminifer distribution, Hole U1486B. **Download table in CSV format**.

Benthic foraminifers

Benthic foraminifers were studied in every core catcher sample from Hole U1486B. Specimen counts are presented in Table **T6**. The planktonic:benthic foraminifer ratio is ~99:1 in all studied samples. The composition of the assemblages is similar to that at Sites U1482 and U1483 and is characteristic of bathyal water depths. *Planulina wuellerstorfi* is present except in three of the core catcher samples (363-U1486B-4H-CC [35.05 mbsf], 11H-CC [101.39 mbsf], and 16H-CC [148.89 mbsf]. The upper bathyal species *Cibicidoides pachyderma* is present in about half of the core catcher samples. The benthic foraminifer assemblages are dominated by *Bolivinita quadrilatera*, which usually lives between 750 and 2000 mbsl, and *Bolivina robusta*, which occurs between 7 and 3500 mbsl (van Morkhoven et al., 1986; Jones, 1994). The bathyal species *Uvigerina hispida* and *Uvigerina proboscidea* are present in all samples except Samples 15H-CC (139.17 mbsf), 18H-CC (167.5 mbsf), and 19H-CC (174.08 mbsf). The shallow dweller (4–70 mbsl) *Rotalinoides compressiusculus* is found in association with the deepwater assemblage in Samples 2H-CC (16.01 mbsf), 5H-CC (44.40 mbsf), and 12H-CC (110.94 mbsf). The substantial amount of volcanic ash in the sediment from Samples 14H-CC through 20H-CC (129.93–186.95 mbsf) does not affect the composition of the benthic foraminifer assemblages.

Foraminifer preservation

Site U1486 is located on relatively young oceanic crust (see **Background and objectives**) and was cored nearly to acoustic basement (see **Operations** and **Core description**). There is a generally increasing proportion of volcanic particles downhole until they become the dominant component in the foraminifer residues. The sediment from the lowermost part of the succession may have been

affected by relatively high heat flow, crustal fluids, and hydrothermal processes (see **Geochemistry** and **Core description**). Four core catcher samples from Hole U1486B were selected to assess foraminifer preservation and diagenesis. The upper three samples (1H-CC [5.94 mbsf], 11H-CC [101.39 mbsf], and 21H-CC [196.02 mbsf]) are spaced at ~100 m intervals following the general approach taken during Expedition 363. These samples range in age from late Pleistocene (<0.07 Ma) to early Pleistocene (~2.39–2.47 Ma). Another sample was taken from a level near the bottom of the hole where foraminifers are subordinate to large volumes of ash (Sample 22H-CC; 205.74 mbsf; ~2.72 Ma).

Foraminifer preservation, as visually assessed in the core catcher samples, is generally excellent to very good. Where preservation is not excellent, this can be due to fragmentation, cementation, and/or incipient recrystallization. There is no obvious depth-related pattern to the suboptimal preservation. Foraminifer preservation in the layers with high proportions of volcanogenic grains appears slightly better (more glassy) than in the more carbonate-rich sediment at similar burial depth. Images of selected specimens are shown in Figure **F17**. The full set of images is available online from the LIMS database (**http://web.iodp.tamu.edu/LORE**).

Sample 363-U1486B-1H-CC (5.94 mbsf; late Pleistocene; <0.07 Ma) shows excellent preservation. Foraminifers have a glassy appearance under the light microscope. In cross section, the wall of *Trilobatus trilobus* shows platy microgranules and other typical biogenic features. Minor superficial damage of the outer chamber surfaces of some specimens, especially the interpore ridges, may indicate abrasion on the seafloor. Pyrite framboids and minor infill-

Figure F17. Downhole foraminifer preservation states, Site U1486. A. Light microscope images to assess the extent of fragmentation and staining and whether the tests are glassy or opaque. B. SEM images of selected specimens (*T. trilobus* and *P. wuellerstorfi*) as whole tests, umbilical side upward. C. High-magnification images of outer wall surfaces to examine additional features such as spine holes, pustules, etc. D. High-magnification images of wall cross sections to find original microgranules or diagenetic crystallites. E. High-magnification images of inner wall surfaces, focusing on evidence for internal overgrowth and cementation.

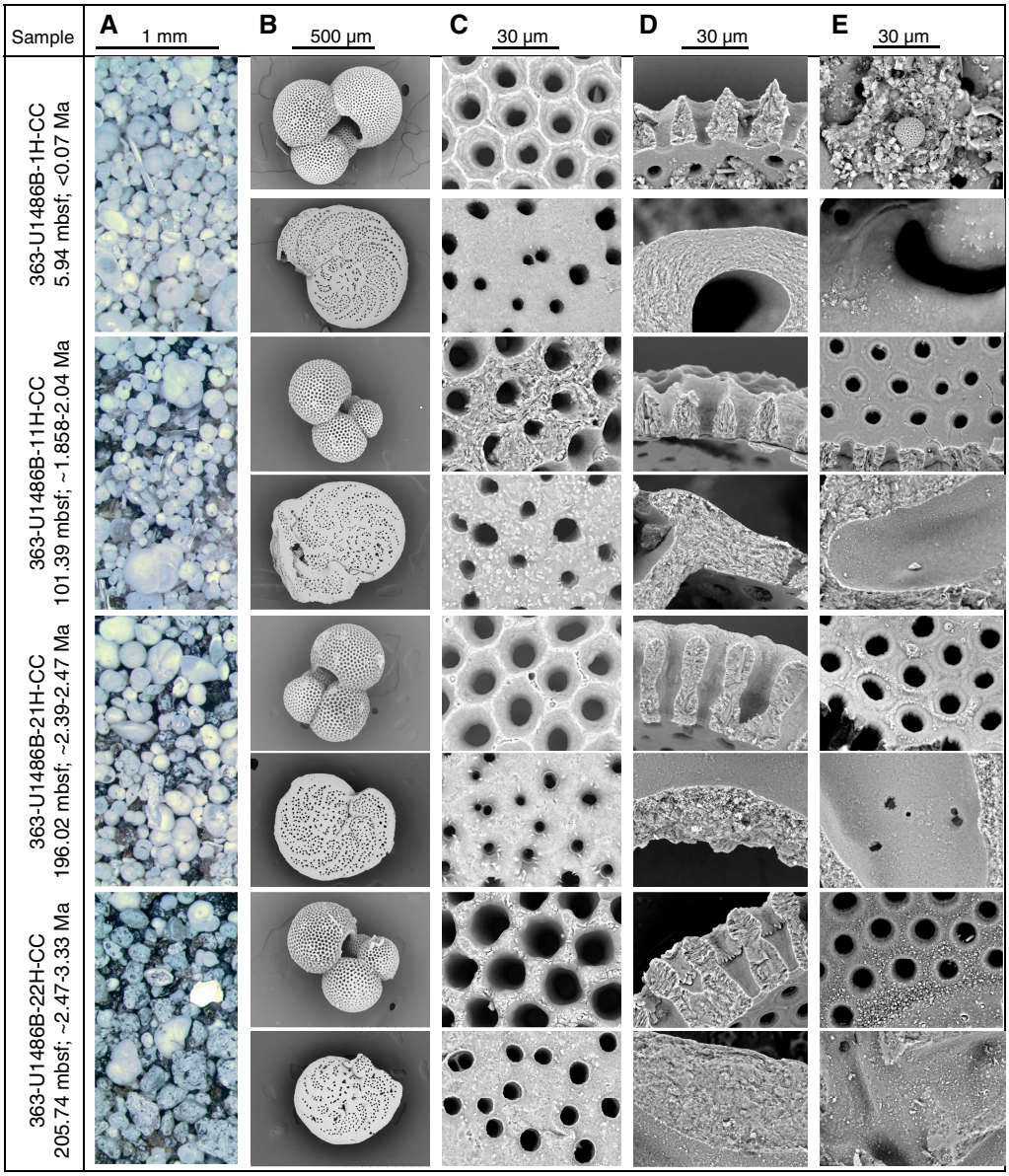

ing of unconsolidated sediment (coccoliths) occur in one examined specimen. In *P. wuellerstorfi* the wall cross section shows biogenic microgranules throughout. All specimens show very minor calcite overgrowth on internal and some external surfaces. Loosely dispersed pyrite framboids up to 3 µm in diameter occur in some patches, with small amounts of cemented sediment infill. There is no evidence of recrystallization or dissolution.

Sample 363-U1486B-11H-CC (101.39 mbsf; early Pleistocene; ~1.88–2.04 Ma) shows excellent preservation. Foraminifers have a glassy appearance under the light microscope. Wall cross sections of both *T. trilobus* and *P. wuellerstorfi* show the biogenic microgranular textures typical of the species and minor evidence of abrasion. The inner wall surfaces of all studied specimens are generally smooth with minor overgrowth of calcite forming an amorphous crystalline layer <1 µm thick. One studied specimen of *T. trilobus* contains pyrite framboids up to 6 µm in diameter. *P. wuellerstorfi* shows very minor calcite overgrowth on outer surfaces. There is no evidence of recrystallization, cementation, or dissolution.

Sample 363-U1486B-21H-CC (196.02 mbsf; early Pleistocene; ~2.39-2.47 Ma) shows excellent to very good preservation. Foraminifers have a glassy appearance under the light microscope. Wall cross sections of *T. trilobus* show platy microgranules and other typical biogenic features, with minor superficial abrasion of the outer chamber surfaces on some specimens. However, the wall cross sections of *P. wuellerstorfi* show evidence of incipient recrystallization and minor calcite overgrowth on the outer surfaces. One *P. wuellerstorfi* specimen contains pyrite framboids up to 3 µm in diameter. There is no evidence of infilling, cementation, or dissolution.

Sample 363-U1486B-22H-CC (205.74 mbsf; early Pleistocene to late Pliocene; ~2.47–3.33 Ma) shows excellent preservation. Foraminifers have a glassy appearance under the light microscope. Wall cross sections of both *T. trilobus* and *P. wuellerstorfi* show biogenic microgranular textures with evidence of minor abrasion. The inner wall surfaces of *T. trilobus* and *P. wuellerstorfi* exhibit moderate calcite overgrowth layers up to 2 µm thick. *P. wuellerstorfi* also shows calcite overgrowth on external surfaces and one studied specimen contained pyrite framboids up to 5 µm in diameter. There is no evidence of recrystallization, cementation, or dissolution.

Shipboard age model

An age-depth plot including all biostratigraphic biohorizons and magnetostratigraphic horizons (see **Paleomagnetism**) is shown in Figure **F18**. Calcareous nannofossil and planktonic foraminifer biohorizons and magnetostratigraphic horizons (see **Paleomagnetism**) show good agreement. Sedimentation rates after 2.15 Ma (0–125 mbsf) are ~6 cm/ky. Before 2.15 Ma (below 125 mbsf), the sedimentation rate was higher, at ~14 cm/ky. Based on these sedimentation rates, the Pliocene/Pleistocene boundary (2.588 Ma) is placed at 183 mbsf, just below the base of Chron C2r.2r (2.581 Ma). The base of the hole (203 mbsf) is assigned a latest Pliocene age, around 2.72 Ma, assuming a constant sedimentation rate of 14 cm/ky for the basal 20 m section.

Figure F18. Age-depth plot for Site U1486 showing integrated biomagnetochronology in Hole U1486A. Sedimentation rates are ~6 cm/ky between 0 and 125 mbsf and 14 cm/ky below 125 mbsf. The base of the hole (203 mbsf) is assigned a latest Pliocene age, ~2.72 Ma, assuming a constant sedimentation rate of 14 cm/ky for the basal 20 m section.

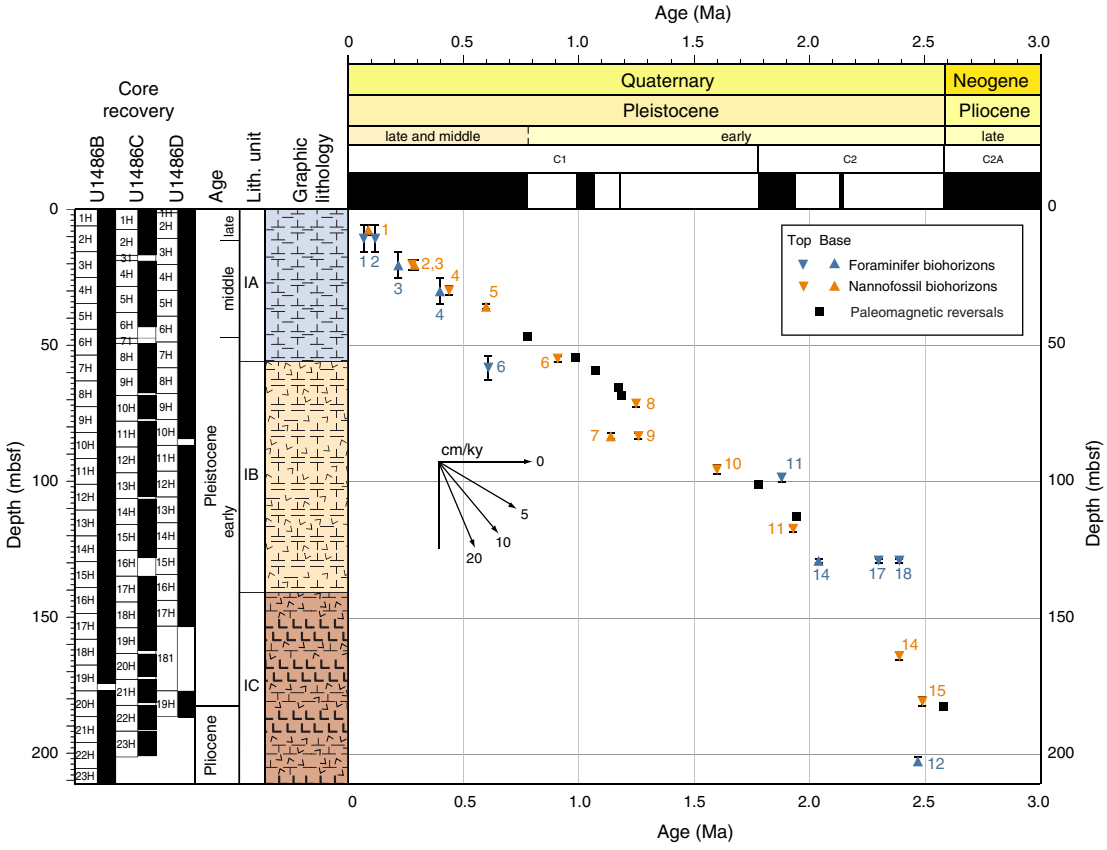

Paleomagnetism

Measurements summary

Paleomagnetic investigations at Site U1486 involved measurement of the natural remanent magnetization (NRM) of archive-half cores from Holes U1486A–U1486D before and after alternating field (AF) demagnetization. We employed a four-step NRM and AF demagnetization procedure (NRM and 10, 15, and 20 mT) to all seven sections of Core 363-U1486A-1H to determine the single-peak AF field (15 mT) to be applied to all measured sections from Holes U1486B–U1486D. In addition to measuring 396 core sections, we took two to three discrete samples per core from Hole U1486B (49 samples) to characterize the NRM demagnetization behavior and to investigate the rock magnetic properties of the sediment. The NRM of discrete samples was measured before and after AF demagnetization in peak fields of 5, 10, 15, 20, 30, and 40 mT. Rock magnetic investigations comprised measurements of magnetic susceptibility (χ), susceptibility of anhysteretic remanent magnetization (χARM) imparted using a 100 mT AF demagnetization and 0.05 mT direct current bias field, and isothermal remanent magnetization (IRM) acquired in 300 mT and 1000 mT (saturation IRM [SIRM]) fields. All sample measurements were mass corrected. The Icefield MI-5 core orientation tool was deployed with nonmagnetic hardware for all cores, which permitted azimuthal correction of declination. Azimuthally corrected declination is largely coherent between cores; however, absolute values in all holes cluster around 180° for normal polarity and 0° for reversed polarity, suggesting that the issues of the baseline offset in azimuthally corrected declination experienced at the majority of sites during Expedition 363 and during previous expeditions (McNeill et al., 2017) affected these data. McNeill et al. (2017) suggest a simple –180° correction could be applied to the corrected declination data to rotate them back to expected values for the respective polarity. However, we leave declination uncorrected for this additional offset in the plotted figures, so care should be employed for future calculations of virtual geomagnetic poles (VGPs) using these data.

Rock magnetic characterization

Whole-Round Multisensor Logger (WRMSL) magnetic susceptibility data average 94 × 10^{-5} SI (see **Physical properties**) and, when coupled with average χ (5.8 × 10^{-7} ± 9.2 × 10^{-7} m^3/kg as 2 standard deviations [2σ]) and SIRM (1.8 × 10^{-2} ± 3.8 × 10^{-2} Am^2/kg as 2σ) values, suggest moderately high (ferri)magnetic mineral concentration in the sediment deposited at Site U1486 (Figure **F19**). In the uppermost ~62 mbsf of Hole U1486B, the majority of samples acquire >90% of their SIRM remanence in a 300 mT field, suggesting that ferrimagnetic minerals (e.g., [titano]magnetite [$Fe_xTi_xO_4$] and/or maghemite [γ-Fe_2O_3]) control the remanence-carrying properties of the sediment. Between ~62 and 204 mbsf, average IRM_{300mT}/IRM_{1000mT} values decrease slightly and cluster around ~0.9 (range = ~0.87–0.94), potentially suggesting greater influence of higher coercivity minerals (e.g., hematite [Fe_2O_3] and goethite [FeO(OH)]) at depth. Two samples from Core 363-U1486B-23H possess very high values (>0.99), indicating a return to strongly ferrimagnetic phases at the base of the hole. The upper ~62 mbsf of Hole U1486B is characterized by relatively low ferrimagnetic concentration (low χ and SIRM) that then increases with depth. Magnetic grain size shows a three-step change with relatively coarse ferrimagnetic grain sizes (low χARM/SIRM) in the upper ~20 mbsf, a finer magnetic assemblage (higher χARM/SIRM) between ~20 and 62 mbsf, and a progressive coarsening of grain size downhole accompanying the increases in ferrimagnetic concentration.

Figure F19. Archive-half NRM intensity after 15 mT AF demagnetization, discrete sample χ and IRM, and discrete sample χARM/SIRM and IRM_{300mT}/IRM_{1000mT} ratios, Hole U1486B.

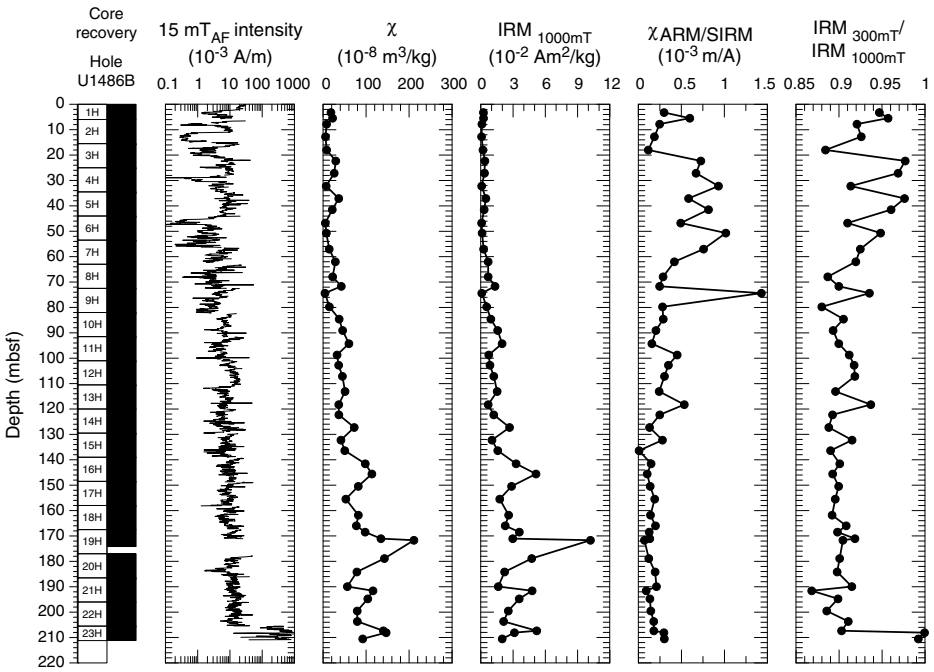

NRM_{15mT} intensity shows a similar pattern to magnetic susceptibility and SIRM with relatively low and variable values (range = ~10^{-5}–10^{-3} A/m) in the upper ~82 mbsf and higher, less variable, and steadily increasing values between ~82 and 205 mbsf (~10^{-4}–10^{-3} A/m), with the highest values (up to 10^{-1} A/m) at the very base of the hole. Decreases in intensity and magnetic grain size, increases in magnetic concentration, and increases in the proportion of higher coercivity minerals at ~62 mbsf occur coevally with the boundary between lithologic Subunits IA and IB, which marks the transition from sediment dominated by biogenic material (foraminifer-rich nannofossil ooze) to a mix of volcanogenic and biogenic material (ash- and foraminifer-bearing nannofossil ooze with interbedded tephra layers) (see **Core description**). Coarser magnetic grain sizes and higher magnetic concentration in the middle to lower part of Hole U1486B are likely related to increases in the concentration of mafic volcanogenic material, with the highest magnetic concentrations at the very bottom of the hole (Core 363-U1486B-23H) associated with the occurrence of basalt fragments (see **Core description**). Assuming a value of ~660 × 10^{-6} m^3/kg for pure single-domain and multidomain magnetite (Maher, 1988), our data suggest a maximum magnetite content of ~0.32%. Interstitial water sulfate concentrations at Site U1486 remain elevated downhole (see **Geochemistry**), and rock magnetic data show little to no evidence of strong magnetic mineral diagenesis (e.g., Karlin and Levi, 1983; Rowan et al., 2009) at depth. As a result, NRM is most likely acquired through (post)depositional remanent magnetization (pDRM) processes that can potentially be used to understand and reconstruct paleogeomagnetic field behavior.

Paleomagnetic data and core orientation

NRM demagnetization behavior and IRM_{300mT}/IRM_{1000mT} ratios are consistent with (titano)magnetite being the primary remanence-carrying mineral species in sediments deposited at Site U1486 (Figures **F19**, **F20**). The drill string overprint is largely removed after AF demagnetization in a 5–15 mT field, and following exposure to higher AF demagnetization steps, inclination and declination stabilize and trend to the origin on Zijderveld diagrams (Zijderveld, 1967), indicating a single component to the magnetization (Figure **F20**). Origin-anchored maximum angular deviation values of the principal component analysis (PCA) calculated over the 15–40 mT range average 3.9° (range = 0.4°–10.1°) in Hole U1486B (Figures **F20**, **F21**), suggesting paleomagnetic directions are stable and well resolved. These values increase slightly downhole from the seafloor, but the generally low maximum angular deviation values (less than ~5°) coupled with qualitative information gleaned from Zijderveld diagrams and stereoplots (Figure **F20**) indicate that the sed-

Figure F20. A–F. Discrete sample AF demagnetization results, Hole U1486B. Left plots: intensity variation through progressive demagnetization steps. Middle and right plots: NRM vector measurements after each AF demagnetization treatment on orthogonal (Zijderveld; blue = horizontal projections, red = vertical projections) and stereographic (solid squares = positive inclination, open squares = negative inclination) projections, respectively. MAD = maximum angular deviation.

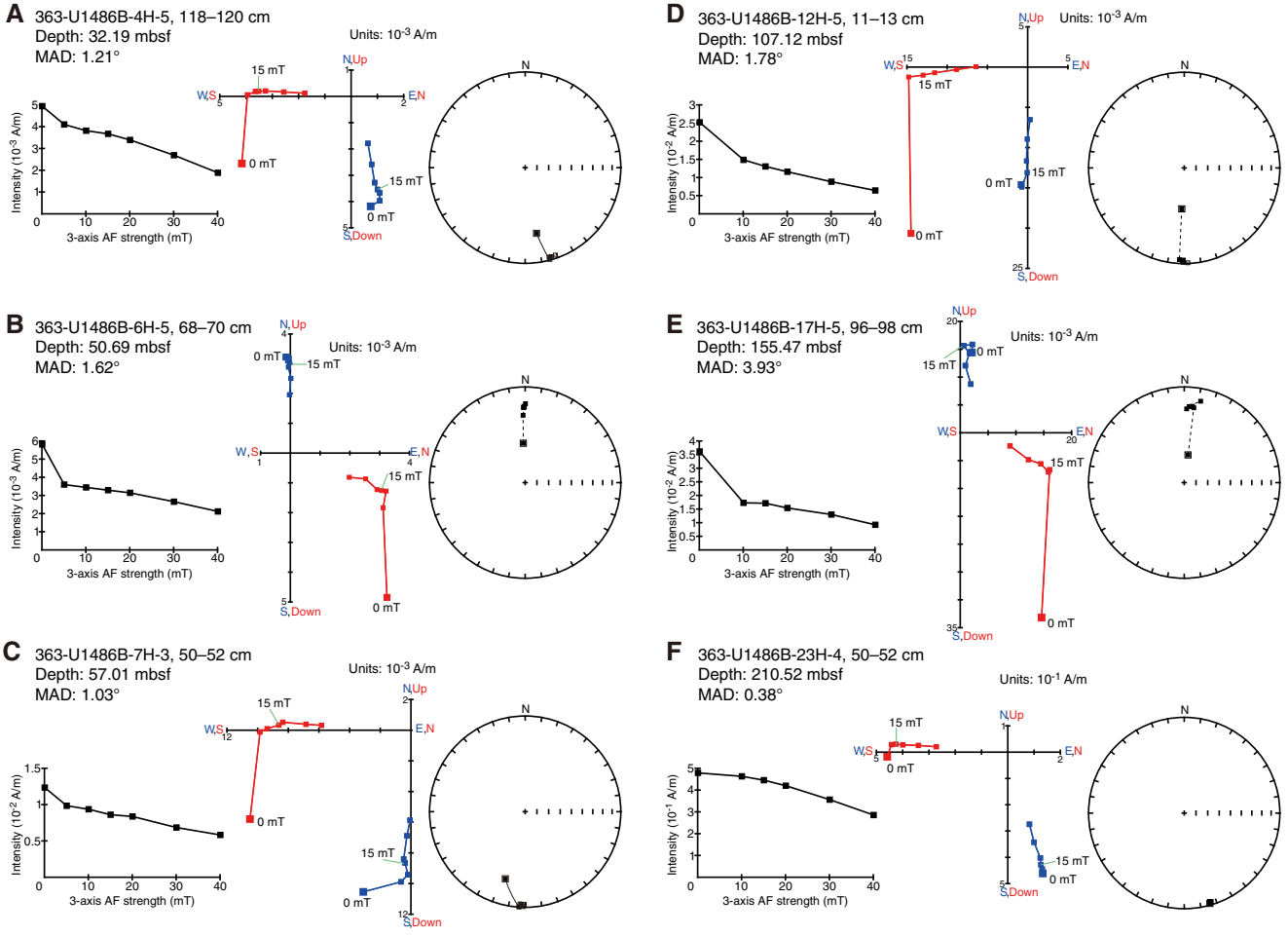

iment should yield reliable estimates for magnetostratigraphy (Stoner and St-Onge, 2007).

For all APC cores from Site U1486, declination was corrected using the Icefield MI-5 tool (see **Operations**). Azimuthally corrected declination is consistent between adjacent cores, and absolute values cluster around ~0° and ~180° (Figures **F21**, **F22**, **F23**). However, assuming the uppermost sediment in each hole was deposited during normal polarity associated with the Brunhes Chron (see **Biostratigraphy**) declination values at Site U1486 experience an offset of ~180° in absolute terms because declination should cluster around 0° (180°) during periods of normal (reversed) polarity. This phenomenon was a persistent issue during Expedition 363 and was also experienced during Expedition 362 (McNeill et al., 2017). Core 363-U1486B-7H suffered a shattered and twisted liner during coring operations. When declination for this core was corrected, it plotted ~60° shallower than Cores 6H and 8H. Because this core contains the upper Jaramillo normal boundary in the lower part of Section 363-U1486B-7H-1 (Table **T7**), we used the uppermost stable polarity interval to manually align declination from the top of Section 363-U1486B-7H-1 to the bottom of Core 6H, resulting in the additional 60° declination correction. The lower Jaramillo normal boundary occurs in Section 363-U1486B-7H-5, and the stable polarity in Section 7H-6 aligns well with the top of Core 8H using the 60° correction derived for the top of the core. Azimuthally oriented declination data for Core 363-U1486B-7H are plotted in dark red in Figure **F21** to indicate the data points with this additional rotation. Replication of these two reversal boundaries in the declination data at similar depths (Table **T7**) in Holes U1486C (Figure **F22**) and U1486D (Figure **F23**) suggests that this additional correction is appropriate.

NRM intensity before and after 15 mT AF demagnetization, WRMSL magnetic susceptibility, and inclination and azimuthally corrected declination after 15 mT AF demagnetization are shown for Holes U1486B, U1486C, and U1486D in Figures **F21**, **F22**, and **F23**, respectively. Displayed inclination and declination values were cleaned of visibly disturbed intervals and voids (see **Paleomagnetism** in the Expedition 363 methods chapter [Rosenthal et al., 2018a]), but the extensive volcanogenic deposits that occur in lithologic Subunits IB and IC deeper than ~60 mbsf (see **Core description**) are too numerous, and often too diffuse, to fully clean from the records. Volcanogenic sediments can potentially affect NRM intensity and directions (Le Friant et al., 2013), and the greater scatter in SRM directions below ~60 mbsf may be related to these horizons. Inclination and declination measured on discrete samples are generally in excellent agreement with those measured on the archive-half sections (Figure **F21**), although between ~110 and 180 mbsf discrete inclination is often shallower than its SRM-measured counterpart. In the upper 60 mbsf and below 180 mbsf, discrete and SRM-measured inclination plots around the expected values of approximately ±3° for the site latitude assuming a geocentric axial dipole (GAD) field. Between 60 and 180 mbsf, inclination is positive and steeper than that predicted from a GAD field. Steep inclinations in a positive direction are most frequently interpreted as a pervasive overprint that is not removed after relatively low AF demagnetization (Richter et al., 2007). Interestingly, the steepest inclinations in Hole U1486B are associated with periods when declination clusters around ~0°/360°. This association suggests that sediment deposited during periods of reversed polarity may be more susceptible to pervasive overprinting than sediment deposited in periods of normal polarity. A similar polarity-specific signature was observed during

Figure F21. NRM intensities before and after 15 mT AF demagnetization, WRMSL MS, maximum angular deviation (MAD), and inclination (dashed lines = predicted values assuming a geomagnetic axial dipole [GAD] field for normal (–3°) and reversed (3°) polarity for the site latitude) and declination (red = azimuthally corrected values, dark red = manually adjusted declination for 363-U1486B-7H) after 15 mT AF demagnetization, Hole U1486B. Black squares = discrete samples. Magnetostratigraphy and GPTS shown at right. Black = normal polarity, white = reversed polarity.

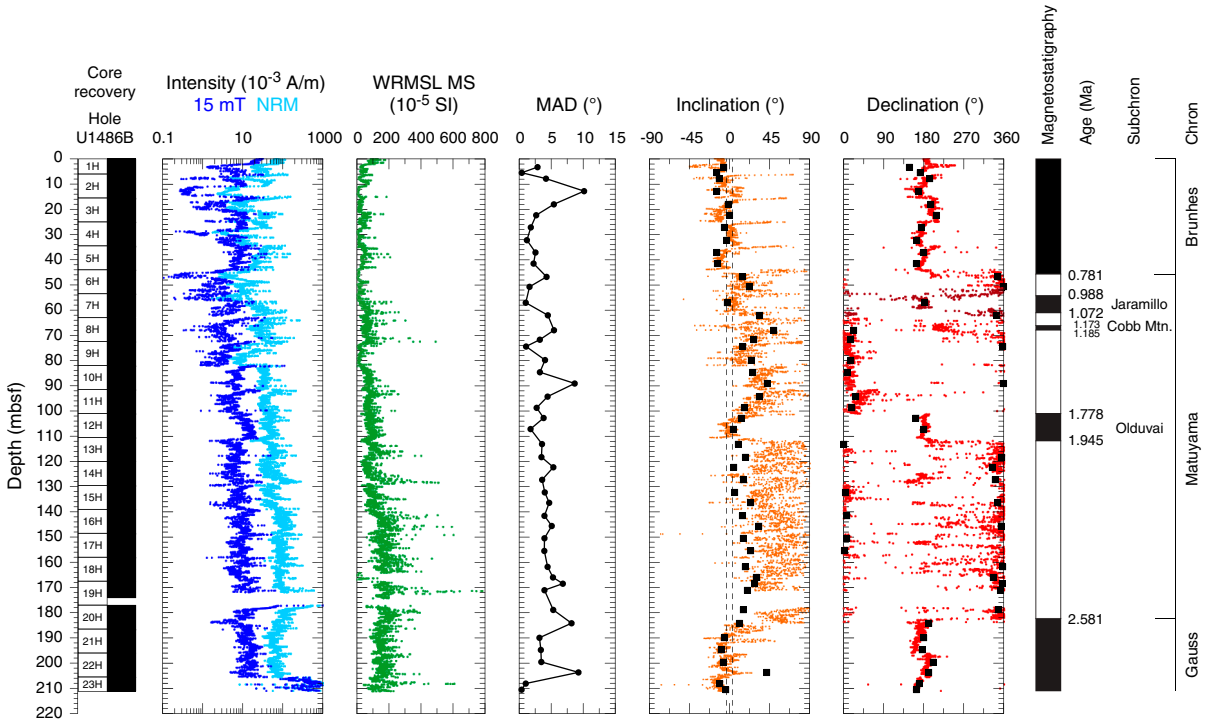

Figure F22. NRM intensities before and after 15 mT AF demagnetization, WRMSL MS, and inclination (dashed lines = predicted values assuming a GAD field for normal (–3°) and reversed (3°) polarity for the site latitude) and azimuthally corrected declination after 15 mT AF demagnetization, Hole U1486C. Magnetostratigraphy and GPTS shown at right. Black = normal polarity, white = reversed polarity.

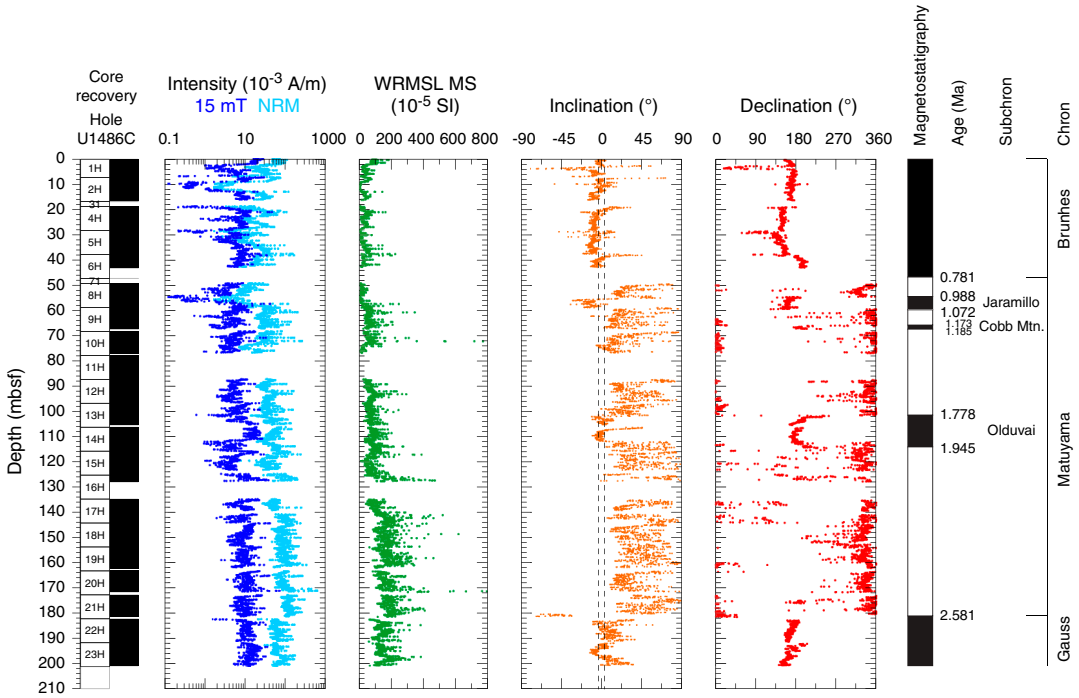

Figure F23. NRM intensities before and after 15 mT AF demagnetization, WRMSL MS, and inclination (dashed lines = predicted values assuming a GAD field for normal (–3°) and reversed (3°) polarity for the site latitude) and azimuthally corrected declination after 15 mT AF demagnetization, Hole U1486D. Magnetostratigraphy and GPTS shown at right. Black = normal polarity, white = reversed polarity.

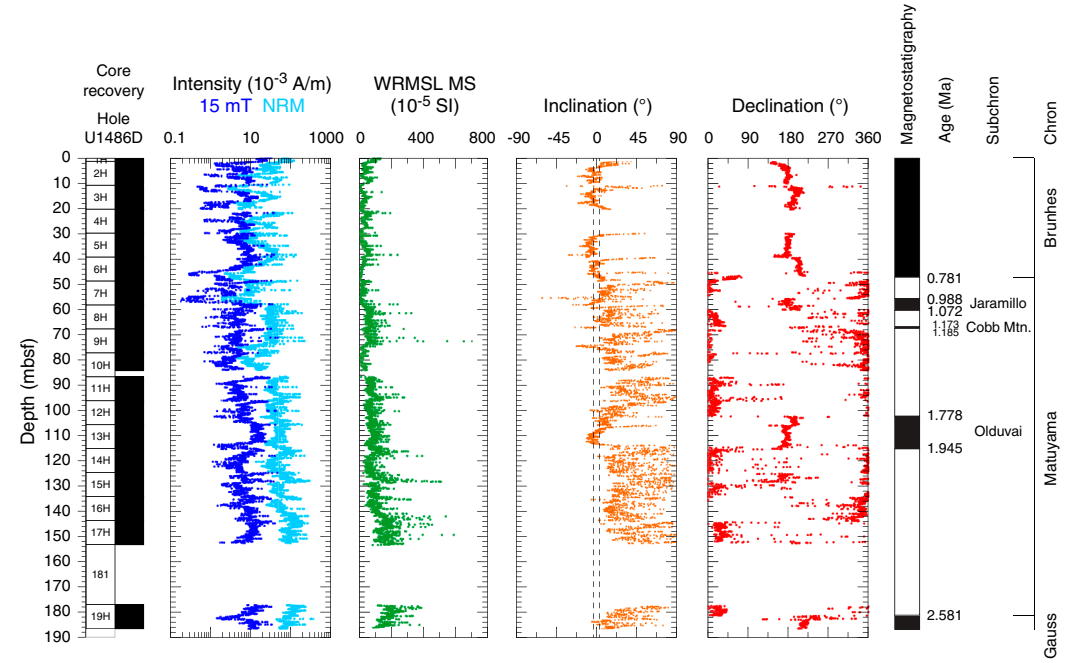

Integrated Ocean Drilling Program Expedition 320/321 where inclination measured during normal polarity intervals yielded steeper than GAD-like values, whereas reversed polarity intervals were relatively unaffected (Pälike et al., 2010). In cores recovered using the XCB system at Integrated Ocean Drilling Program Sites U1331 and U1332, the systematic offset in inclination between different polarities was used to help guide polarity determinations (Pälike et al., 2010).

Table T7. Top and base depths of identified reversal boundaries determined from last and first points of stable polarity in Holes U1486B, U1486C, and U1486D. * = reversal occurs between cores. The midpoint (arithmetic mean) depth and range are also shown. Ages are determined using the geologic timescale of Hilgen et al. (2012). **Download table in CSV format.**

Horizon	Age (Ma)	Top depth (mbsf)	Base depth (mbsf)	Midpoint depth (mbsf)	Range (m)	Avg. sed. rate (cm/ky)
Hole U1486B						
Brunhes/Matuyama	0.781	46.08	47.38	46.73	0.65	6.0
Upper Jaramillo	0.988	53.90	55.43	54.66	0.77	3.8
Lower Jaramillo	1.072	59.20	59.55	59.38	0.17	5.6
Upper Cobb Mtn.	1.173	65.33	65.73	65.53	0.19	6.1
Lower Cobb Mtn.	1.185	68.13	69.05	68.59	0.46	25.5
Upper Olduvai*	1.778	101.08	101.30	101.19	0.11	5.5
Lower Olduvai	1.945	111.78	114.05	112.91	1.14	7.0
Matuyama/Gauss	2.581	182.35	182.70	182.53	0.17	10.9
Hole U1486C						
Brunhes/Matuyama*	0.781	42.90	49.60	46.25	3.35	5.9
Upper Jaramillo	0.988	54.30	54.70	54.50	0.20	4.0
Lower Jaramillo	1.072	59.28	59.48	59.38	0.09	5.8
Upper Cobb Mtn.	1.173	65.83	66.15	65.99	0.16	6.5
Lower Cobb Mtn.*	1.185	67.08	68.63	67.85	0.78	15.5
Upper Olduvai	1.778	101.25	101.95	101.60	0.35	5.7
Lower Olduvai	1.945	114.05	114.55	114.30	0.25	7.6
Matuyama/Gauss*	2.581	181.18	182.65	181.91	0.74	10.6
Hole U1486D						
Brunhes/Matuyama	0.781	46.63	48.25	47.44	0.81	6.1
Upper Jaramillo	0.988	55.65	55.78	55.71	0.06	4.0
Lower Jaramillo	1.072	60.13	60.23	60.18	0.05	5.3
Upper Cobb Mtn.	1.173	66.55	67.00	66.77	0.23	6.5
Lower Cobb Mtn.*	1.185	67.32	67.93	67.62	0.30	7.1
Upper Olduvai	1.778	102.13	102.55	102.34	0.21	5.9
Lower Olduvai	1.945	114.35	115.33	114.84	0.48	7.5
Matuyama/Gauss*	2.581	181.05	182.83	181.94	0.88	10.6

In contrast to inclination, declination appears relatively insensitive to a strong drill string–induced overprint because declination values after 5–10 mT AF demagnetization remain stable through higher AF demagnetization steps (Figure **F20**). Because of the equatorial location of Site U1486, declination was more instructive than inclination for determination of magnetic polarity. Given the lack of a strong overprint in declination, we were hesitant to expose the sediments to AF demagnetization higher than 15 mT to remove the pervasive overprint in inclination for no substantial gain in magnetostratigraphic information. Any future estimates of paleosecular variation (PSV), relative paleointensity (RPI), or VGPs for the site should first use higher AF demagnetization to fully clean the record of any remaining drill-string overprint.

Magnetostratigraphy

Sediment in all holes appears to have been deposited (quasi)continuously with no major hiatuses or erosional surfaces (see **Core description** and **Biostratigraphy**). Across Holes U1486B–U1486D, we observed eight coeval and distinct ~180° changes in declination downhole. These declination shifts occur at the same depth that inclination changes from GAD-like values during normal polarity to steeper, positive, and more overprinted values during reversed polarity. Interpretation of these horizons as pDRM-recorded reversals of the geomagnetic field allows correlation to the geomagnetic polarity timescale (GPTS; Cande and Kent, 1995) of the geologic timescale (Hilgen et al., 2012) and assignment of age. The Matuyama/Brunhes boundary (0.781 Ma) is identified at 46.08–48.25 mbsf (note that these ranges encompass the minimum and maximum mbsf depths across all three holes where the reversal is identified within a single core, not between adjacent cores; see Table **T7** for the depths of each boundary in each hole). Below this boundary, we observed the upper (53.9–55.78 mbsf; 0.988 Ma) and lower (59.2–60.23 mbsf; 1.072 Ma) boundaries of the Jaramillo normal (C1r.1n), the upper (65.33–67 mbsf; 1.173 Ma) and lower (68.13–69.05 mbsf; 1.185 Ma) boundaries of the Cobb Mountain Subchron (C1r.2n), and the upper (101.08–102.55 mbsf; 1.778 Ma) and lower (111.78–114.55 mbsf; 1.945 Ma) boundaries of the Olduvai normal (C2n). At 182.35–182.7 mbsf in Hole U1486B and at 181.05–182.5 mbsf in Hole U1486D, we observed the Gauss/Matuyama boundary (2.581 Ma). Continued normal polarity below this depth in all three holes implies that the recovered sediment is younger than 3.032 Ma, as the upper boundary of the Kaena reversed subchron (C2An.1n) was not observed. The depths of these paleomagnetic reversal boundaries indicate a sedimentation rate of 10.9 cm/ky from the late Pliocene until 1.945 Ma (Table **T7**) and then an approximate halving of sedimentation rate to 5.8 cm/ky, after which the rate remained stable for the rest of the mid- to late Pleistocene. These reversal horizons and estimated sedimentation rates are in excellent agreement with both the calcareous nannofossil and planktonic foraminifer datums (Figure **F18**) (see **Biostratigraphy**).

Physical properties

Physical properties were measured on whole-round cores, split cores, and discrete samples from all four holes drilled at Site U1486 to provide basic information for characterizing the core sections. Because Core 363-U1486A-1H missed the mudline, Hole U1486A was terminated after only one core, and Hole U1486B became the first deep hole (see **Operations**). Therefore, all discrete measurements were performed on Hole U1486B. GRA bulk density and magnetic susceptibility were measured on all core sections from Holes U1486C and U1486D with the Special Task Multisensor Logger (STMSL) immediately after the cores were brought onboard. All core sections were measured with the GRA bulk densitometer, the magnetic susceptibility loop, and the *P*-wave logger (PWL) on the WRMSL. NGR was measured on all whole-round sections (Holes U1486A and U1486B at 10 cm resolution and subsequent holes at 20 cm resolution) as soon as possible after STMSL measurements (see **Physical properties** in the Expedition 363 methods chapter [Rosenthal et al., 2018a]). Furthermore, to aid stratigraphic correlation, Cores 363-U1486D-10H and 11H were also measured at 10 cm resolution. Although protocol generally requires NGR background to be measured between sites that are >1° latitude apart, no background could be measured between Sites U1485 and U1486 because transit time to Site U1486 was limited (<10 h) and cores from Site U1485 were still being run on the NGRL during transit. Point-sensor magnetic susceptibility and color spectrophotometry (color reflectance) were measured on split-core sections using the Section Half Multisensor Logger (SHMSL). Discrete thermal conductivity, *P*-wave velocity, and moisture and density (MAD) measurements were made in Hole U1486B. Discrete *P*-wave measurements (*z*- and *x*-axis) were made using the *P*-wave caliper (PWC) system on the Section Half Measurement Gantry (SHMG). Preconditioning treatments were applied to the records to aid in interpretation of noisy or spiky data (for details, see **Physical properties** in the Expedition 363 methods chapter [Rosenthal et al., 2018a]). Because GRA bulk density showed large variations corresponding to the amount of volcanic material in the sediment, the median-filter method was not

Figure F24. Physical property measurements, Holes U1486B and U1486C. GRA bulk density, magnetic susceptibility and *P*-wave data were measured on the WRMSL. Yellow shading in Hole U1486B magnetic susceptibility marks sections affected by instrumental offset. cps = counts per second.

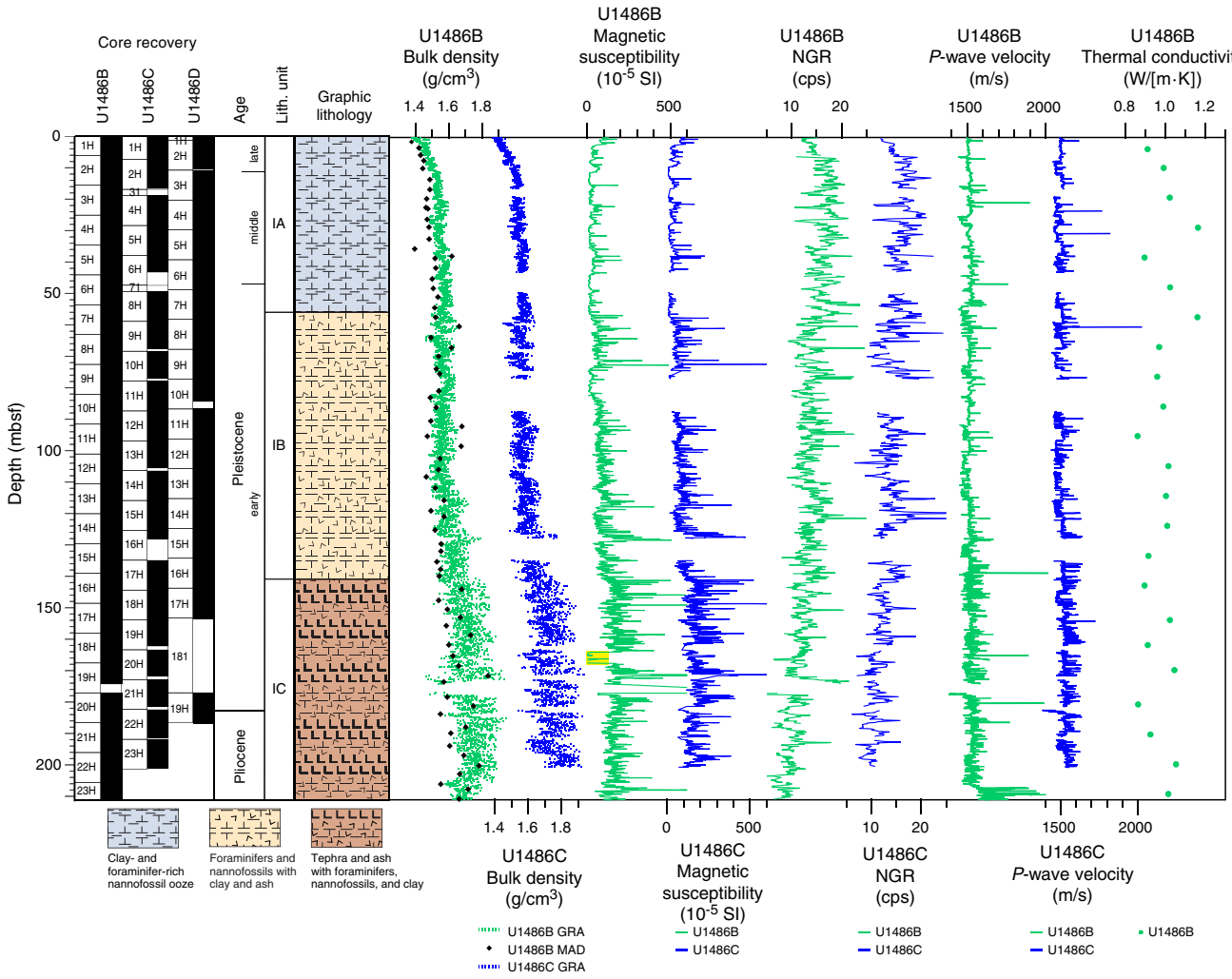

applied because it removed too many of the high GRA bulk density values. Additionally, *P*-wave values were culled above 2050 m/s instead of 1750 m/s to retain high velocity measurements from volcanogenic sediment and hydrothermal precipitates. All data shown in figures are from the preconditioned data sets. Tables presented in this section contain raw and treated data for NGR and WRMSL GRA bulk density, magnetic susceptibility, and *P*-wave velocity. Raw data for all data sets are available from the LIMS database.

GRA bulk density

GRA bulk density reproducibility between holes at Site U1486 is excellent, with all holes showing a general trend of increasing values with depth, most likely due to compaction. Additionally, GRA bulk density shows increasing variance with depth, most likely reflecting variations in lithology (Figure **F24**; Tables **T8**, **T9**, **T10**, **T11**). For description purposes, data from Holes U1486B and U1486C are considered representative for the site because these are the most continuous and deepest holes cored. In all holes, GRA bulk density increases rapidly from ~1.42 g/cm^3 at the seafloor to 1.54 g/cm^3 at ~8 mbsf, reflecting sediment consolidation below the sediment/water interface. Between ~8 and ~140 mbsf, GRA bulk density increases from 1.5 to 1.63 g/cm^3, corresponding to lithologic Subunits IA and IB (see **Core description**). Between ~140 and ~202 mbsf, variance increases by ~30% with values fluctuating around 1.72 g/cm^3. This high-variability interval corresponds to Subunit IC, which is marked by a color change from dark to very dark layers and a change in dominant lithology to volcanogenic particles (see **Core description**). One of the largest peaks in GRA bulk density at ~128

Table T8. Raw and cleaned Whole-Round Multisensor Logger gamma ray attenuation (GRA) bulk density data. Hole U1486A. **Download table in CSV format**.

Table T9. Raw, cleaned, and detrended Whole-Round Multisensor Logger gamma ray attenuation (GRA) bulk density data. Hole U1486B. **Download table in CSV format**.

Table T10. Raw and cleaned Whole-Round Multisensor Logger gamma ray attenuation (GRA) bulk density data, Hole U1486C. **Download table in CSV format**.

Table T11. Raw, cleaned, and detrended Whole-Round Multisensor Logger gamma ray attenuation (GRA) bulk density data, Hole U1486D. **Download table in CSV format**.

Figure F25. MAD and WRMSL bulk density, WRMSL MS, NGR, and WRMSL *P*-wave velocity overlaid on core photos (generated using Code for Ocean Drilling Data [CODD] [Wilkens et al., 2017]), Hole U1486B. A. 45–80 mbsf. B. 125–140 mbsf.

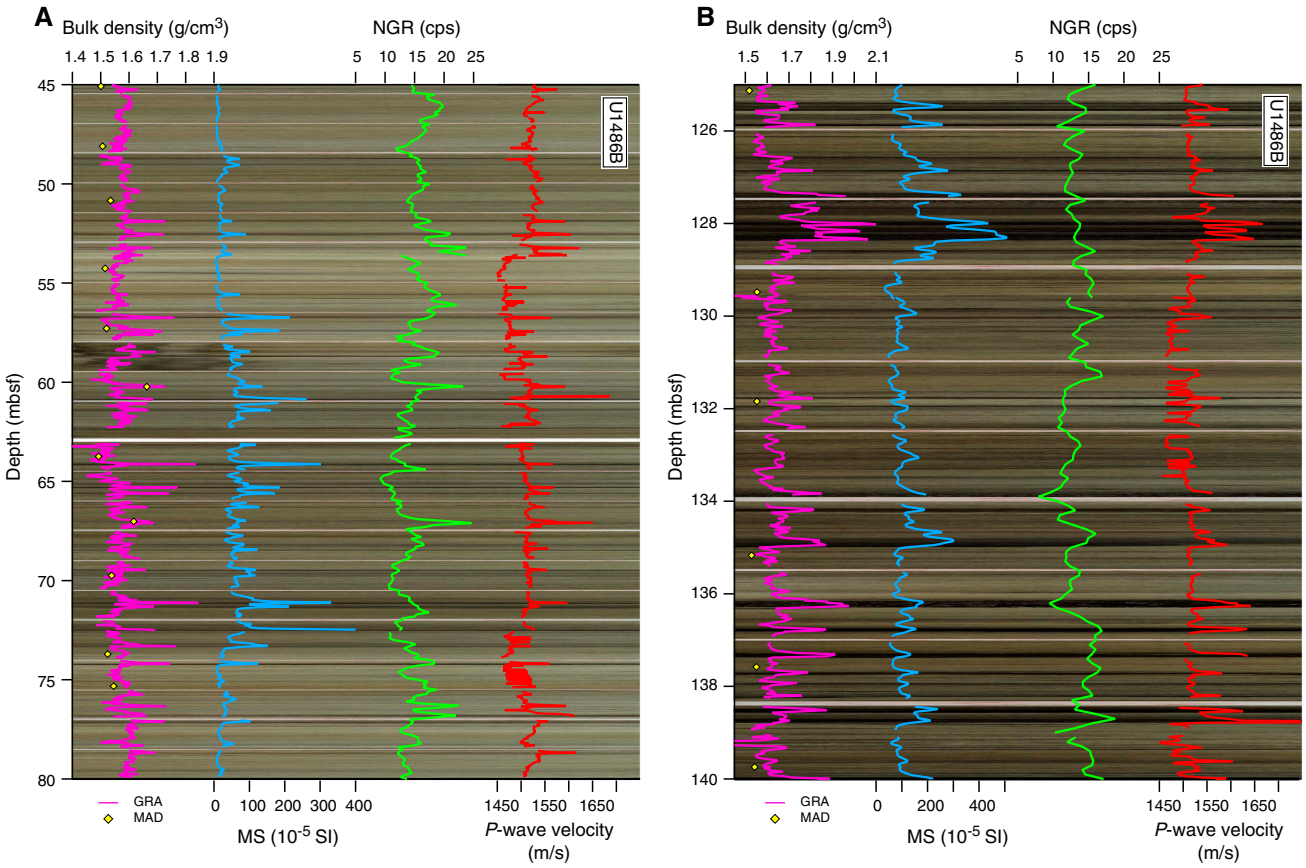

mbsf corresponds to a distinct tephra layer (Figure **F25B**). This peak is also evident in the magnetic susceptibility and *P*-wave records but not in the NGR. From ~202 mbsf to the bottom of the hole, GRA bulk density decreases from 1.8 to 1.7 g/cm^3, coincident with an increase in *P*-wave velocity. This change in GRA density and *P*-wave velocity corresponds to an interval of sediments containing authigenic zeolites and basalt fragments (see **Core description**).

Magnetic susceptibility

Site U1486 exhibits three distinct patterns of magnetic susceptibility variability. In the uppermost 57 mbsf, background values fluctuate between 20 × 10^{-5} and 50 × 10^{-5} SI, with peaks from 100 × 10^{-5} to 200 × 10^{-5} SI corresponding to dark layers in Subunit IA (Figures **F24**, **F25A**; Tables **T12**, **T13**, **T14**, **T15**). Between ~57 and ~140 mbsf, background values increase to 75 × 10^{-5} to 100 × 10^{-5} SI with frequent peaks of 200 × 10^{-5} to 400 × 10^{-5} SI (Figure **F25B**). This interval corresponds to lithologic Subunit IB, which marks an overall increase in abundance of volcanogenic material compared to Subunit IA, making the sediment darker in color. From ~140 mbsf to the bottom of the hole (lithologic Subunit IC), the sediments are dominated by volcanogenic material, with a significant downhole decrease in the biogenic component, and are therefore predominantly dark in color. In this interval, magnetic susceptibility is characterized by background levels of ~200 × 10^{-5} SI with high-frequency variability in the 300 × 10^{-5} to 400 × 10^{-5} SI range. Some peaks reach 600 × 10^{-5} SI in the darkest sediment layers, which contain high amounts of volcanogenic material. These variations in intensity may reflect the different sedimentary processes that are involved in the formation of volcanogenic-rich layers, including direct deposition of volcanogenic material from various sources (tephra layers), redeposition (e.g., mass gravity flows), and/or mixing with biogenic sediments (e.g., through bioturbation) (see **Core description**).

Sections 363-U1486B-18H-5, 18H-6, and 18H-7 are artificially offset to low values (see yellow shading in Figure **F24**) due to obstruction of the WRMSL magnetic susceptibility loop immediately prior to measurement, which meant the loop was zeroed incorrectly (see **Physical properties** in the Expedition 363 methods chapter [Rosenthal et al., 2018a]). Because of the excellent reproducibility among holes and the general consistency of STMSL and SHMSL

Table T12. Raw and cleaned Whole-Round Multisensor Logger magnetic susceptibility (MS) data, Hole U1486A. **Download table in CSV format**.

Table T13. Raw and cleaned Whole-Round Multisensor Logger magnetic susceptibility (MS) data, Hole U1486B. **Download table in CSV format**.

Table T14. Raw and cleaned Whole-Round Multisensor Logger magnetic susceptibility (MS) data, Hole U1486C. **Download table in CSV format**.

Table T15. Raw and cleaned Whole-Round Multisensor Logger magnetic susceptibility (MS) data, Hole U1486D. **Download table in CSV format**.

Table T16. Raw and cleaned Natural Gamma Radiation Logger natural gamma radiation (NGR) data, Hole U1486A. **Download table in CSV format.**

Table T17. Raw and cleaned Natural Gamma Radiation Logger natural gamma radiation (NGR) data, Hole U1486B. **Download table in CSV format.**

Table T18. Raw and cleaned Natural Gamma Radiation Logger natural gamma radiation (NGR) data, Hole U1486C. **Download table in CSV format.**

Table T19. Raw and cleaned Natural Gamma Radiation Logger natural gamma radiation (NGR) data, Hole U1486D. **Download table in CSV format.**

magnetic susceptibility measurements, these artificially offset values can be corrected during postcruise research.

Natural gamma radiation

NGR increases downhole in the uppermost 8 mbsf of all holes from ~11 to ~17 count/s. Below ~8 mbsf, NGR exhibits a long-term decreasing trend with depth, consistent throughout all holes, which is unlike patterns observed at previous sites (Figure **F24**; Tables **T16**, **T17**, **T18**, **T19**). Maximum values of ~20 counts/s are recorded at 25 mbsf and progressively decrease to 8 counts/s at the base of the deepest hole. We also observed ~5–10 m cycles superimposed on the decreasing trend and on longer ~30 m cycles. The NGR relationship to the dark layers is more ambiguous than for magnetic susceptibility. Some dark layers that have high ash content correspond to distinct NGR peaks, whereas other tephra layers with distinct magnetic susceptibility peaks show no corresponding NGR change (e.g., ~128 mbsf in Figure **F25B**). This difference could be due to the lower resolution of the NGR data compared to the magnetic susceptibility data or may indicate mixing of ash particles with the surrounding sediment through bioturbation. The 5–10 m cycles in NGR may correspond to variations in the overall clay content of the sediment (see **Core description**).

P-wave velocity

Measurements of PWL and PWC *P*-wave velocity were obtained to the base of the cored section at Site U1486, unlike at the previous sites where the *P*-wave measurements were stopped at shallower depths due to unreliable values. Overall, *P*-wave velocities at Site U1486 show a slight, long-term increasing trend with depth (slope = 0.17) in all holes (Figures **F24**, **F26**; Tables **T20**, **T21**, **T22**, **T23**). *P*-wave velocity in Holes U1486B and U1486C display short-term (~30 m) cycles punctuating a long-term increase from ~1500 to ~1650 m/s. The most prominent *P*-wave peaks (up to 1950 m/s) generally correspond to dark layers (Figure **F25**). Deeper than ~140 mbsf, *P*-wave velocity variability increases, coincident with an increase in the number of dark layers in Subunit IC (Figure **F24**). *P*-wave velocity on the PWC *x*-axis is generally ~10–30 m/s lower than PWL *P*-wave velocity (Figure **F26**). The slope of the linear trend of *P*-wave velocity versus depth for the PWC *x*-axis is 0.24 including the unusually high measurements at the bottom of the hole, whereas the slope is only 0.076 when values from deeper than ~207 mbsf are excluded. The PWC *z*-axis *P*-wave velocity gives lower values than the *x*-axis. The slope of the downhole *z*-axis linear trend is 0.187. Three outliers have very low values: 1347 m/s at 36.96 mbsf (interval 363-U1486B-5H-2, 96 cm), 1330 m/s at 42.90 mbsf (interval 6H-6, 90 cm), and 1258 m/s at 65.80 mbsf (interval 8H-2, 130 cm) (these data are not shown in Figure **F26**). The linear trend slope is 0.04 when excluding these three outliers.

A prominent feature in Hole U1486B is that *P*-wave velocities are markedly higher at the base of the hole (Figures **F24**, **F26**, **F27**). WRMSL *P*-wave velocities increase from ~1570 m/s at 207 mbsf to

Figure F26. Discrete and whole-round *P*-wave measurements, Site U1486.

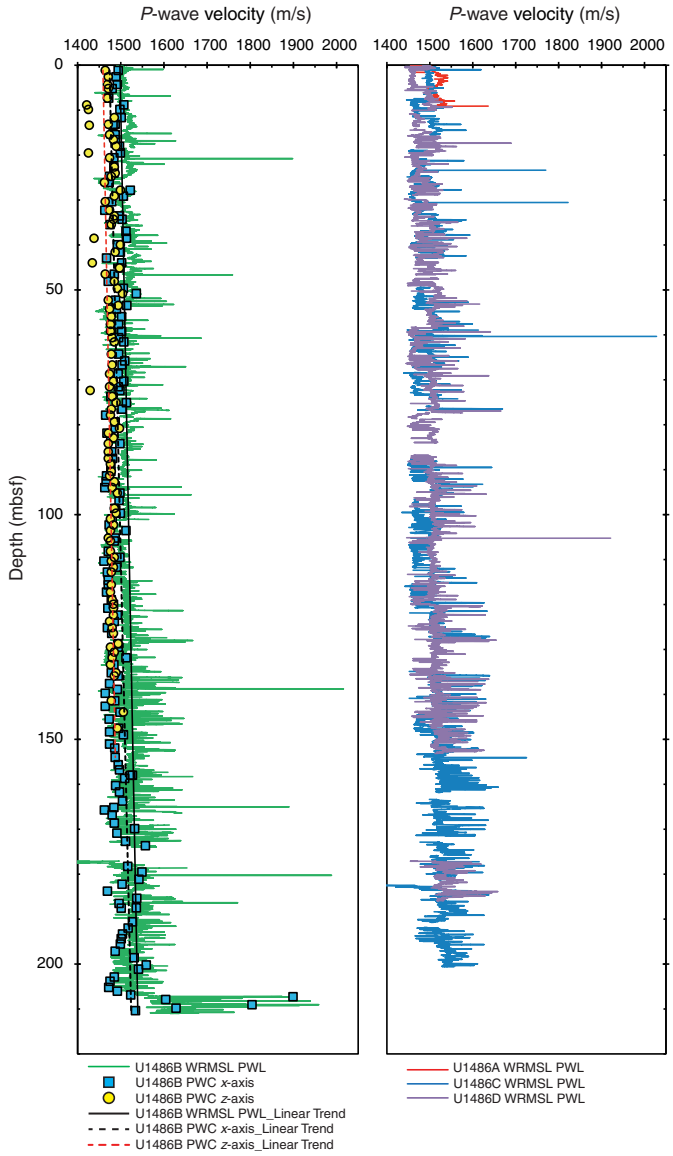

Table T20. Raw and cleaned Whole-Round Multisensor Logger *P*-wave logger data, Hole U1486A. **Download table in CSV format.**

Table T21. Raw and cleaned Whole-Round Multisensor Logger *P*-wave logger data, Hole U1486B. **Download table in CSV format.**

Table T22. Raw and cleaned Whole-Round Multisensor Logger *P*-wave logger data, Hole U1486C. **Download table in CSV format.**

Table T23. Raw and cleaned Whole-Round Multisensor Logger *P*-wave logger data, Hole U1486D. **Download table in CSV format.**

Figure F27. Discrete and whole-round *P*-wave velocity measurements plotted on core photos (generated using CODD [Wilkens et al., 2017]) for the bottom of Hole U1486B (204–211 mbsf). Blue and yellow boxes highlight regions of unusually high PWC measurements. PWC measurements from Sections 23H-2 and 23H-3 were taken from intervals containing authigenic zeolite cement precipitated from alteration of volcanic glass by hydrothermal fluids.

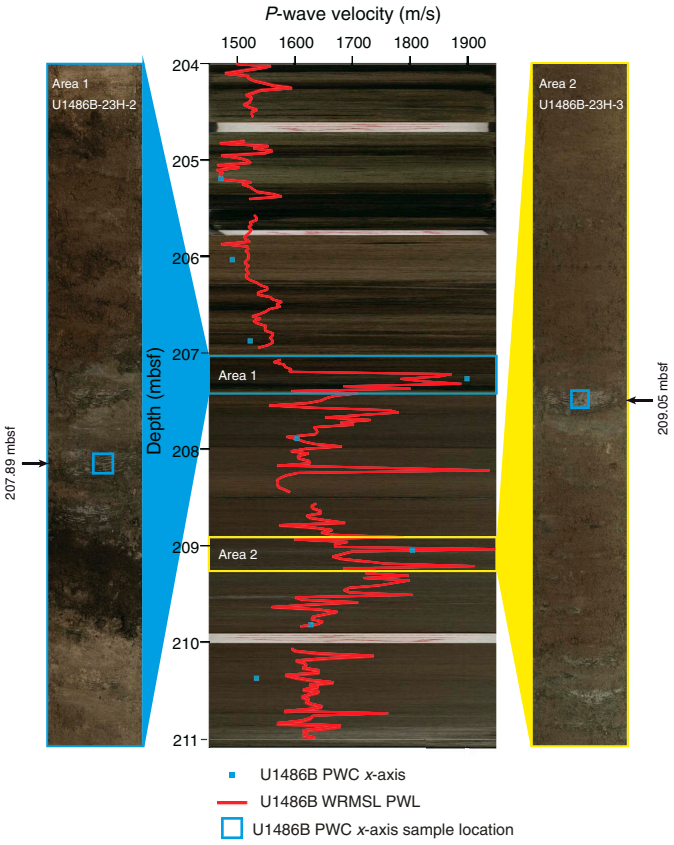

1950 m/s at the bottom of the hole. Out of the five PWC *x*-axis measurements deeper than 207 mbsf, four are >1600 m/s, with two extremely high values of 1804 m/s (interval 363-U1486B-23H-3, 55 cm [209.05 mbsf]) and 1899 m/s (interval 23H-2, 27 cm [207.27 mbsf]) (Figures **F26**, **F27**). The increase below 207 mbsf coincides with the appearance of more indurated sediments that are altered by hydrothermal fluids and partially cemented by authigenic precipitates, including zeolites (see **Core description**). The discrete *x*-axis *P*-wave velocity from these basal sections ranges between ~1650 and 1950 m/s, which is higher than observed at previous sites. This large range could reflect the patchiness of the cementation in the lowermost 4 m of the site, which would produce alternations between more and less indurated intervals.

Moisture and density

Bulk density calculated using the MAD method corresponds well with trends in bulk density estimated from GRA but is offset to lower values through much of the record (Figure **F28**), probably due to water loss. As with magnetic susceptibility and GRA bulk density, MAD density variability increases downhole. Apparent outliers (black arrows in Figure **F28**) mostly occur where volcanogenic sediment layers were sampled and reflect the varying composition of these deposits throughout the hole. The majority of MAD samples reflect the density of the background clay and biogenic ooze. Porosity decreases from ~80% at the top of the hole to ~55%–60% at the bottom because of compaction, but porosity is generally ~10% higher compared with Sites U1484 and U1485, where porosity values are only ~50%–60%. Porosity at the bottom of the hole is difficult to constrain because of the scatter of data. Volcanogenic sediment layers are generally characterized by low porosity and low density, but the variability of the physical properties at the site highlights the complexity and the differences in the composition of the volcanogenic components.

Thermal conductivity

A thermal conductivity profile was obtained at ~10 m resolution in Hole U1486B using a thermal conductivity needle (Figures **F24**, **F28**). Thermal conductivity measurements demonstrate virtually no long-term trend. Instead, values vary between 0.85 and 1.12 W/(m·K) from the seafloor to 66 mbsf and between 0.85 and 1.00 W/(m·K) deeper than 66 mbsf. The large variability in the thermal conductivity measurements and absence of expected downhole increasing trend probably reflect the highly variable lithology and small-scale changes between biogenic- and volcanogenic-rich layers (see **Core description**). Deeper than ~140 mbsf, both thermal conductivity and porosity display increased variability, corresponding with Subunit IC, which includes the darkest layers with highly variable amounts of volcanogenic material.

Downhole temperature measurements

Downhole temperature measurements were made on Cores 363-U1486B-4H (34.5 mbsf), 7H (63.0 mbsf), 10H (91.5 mbsf), and 13H (120.0 mbsf) using the APCT-3. An exponential decrease in temperature was observed between 60 and 600 s after penetration and was used to estimate ambient temperature (unshaded area in Figure **F29**). Temperature increases with depth from 6.51°C at 34.5 mbsf to 13.63°C at 120 mbsf. The correlation of the four downhole temperatures with depth is very high (R^2 = 0.99995). Using the slope of the temperature-depth relationship, we estimate that the bottom water temperature at Site U1486 is 3.60°C, yielding a geothermal gradient of 83°C/km (Figure **F30**).

We generated a thermal conductivity profile (with ~10 m resolution) (Figure **F30**) using laboratory-determined thermal conductivity data (see **Physical properties** in the Expedition 363 methods chapter [Rosenthal et al., 2018a]). Based on the in situ condition correction, thermal resistance was calculated using the "linear approach" outlined in Pribnow et al. (2000) based on the average thermal conductivity of 0.96 W/(m·K). The thermal conductivity is offset relative to uncorrected values by ~0.04 W/(m·K) at the top of the hole; this offset decreases with depth to converge at 180 mbsf. Based on the classic method of Stein and Stein (1992), the slope of the linear fit between temperature and thermal resistance indicates a heat flow of 80 mW/m^2 at Site U1486 (see **Physical properties** in the Expedition 363 methods chapter [Rosenthal et al., 2018a]). However, the classic approach for calculating the ocean crust age using heat flow is inappropriate at Site U1486 because of the high hydrothermal activity, which leads to underestimation of heat flow by ~50% (see figure 4 in Stein and Stein, 1992).

Figure F28. MAD discrete sample dry, bulk, and grain densities and porosity, WRMSL GRA bulk density, and thermal conductivity, Hole U1486B. Arrows = outliers in dry density measured on samples from volcanogenic-rich layers. Outliers are propagated through MAD calculations and are evident in other MAD properties, although they are not explicitly marked. Shading highlights Subunit IC, which shows increased variability in density and porosity measurements.

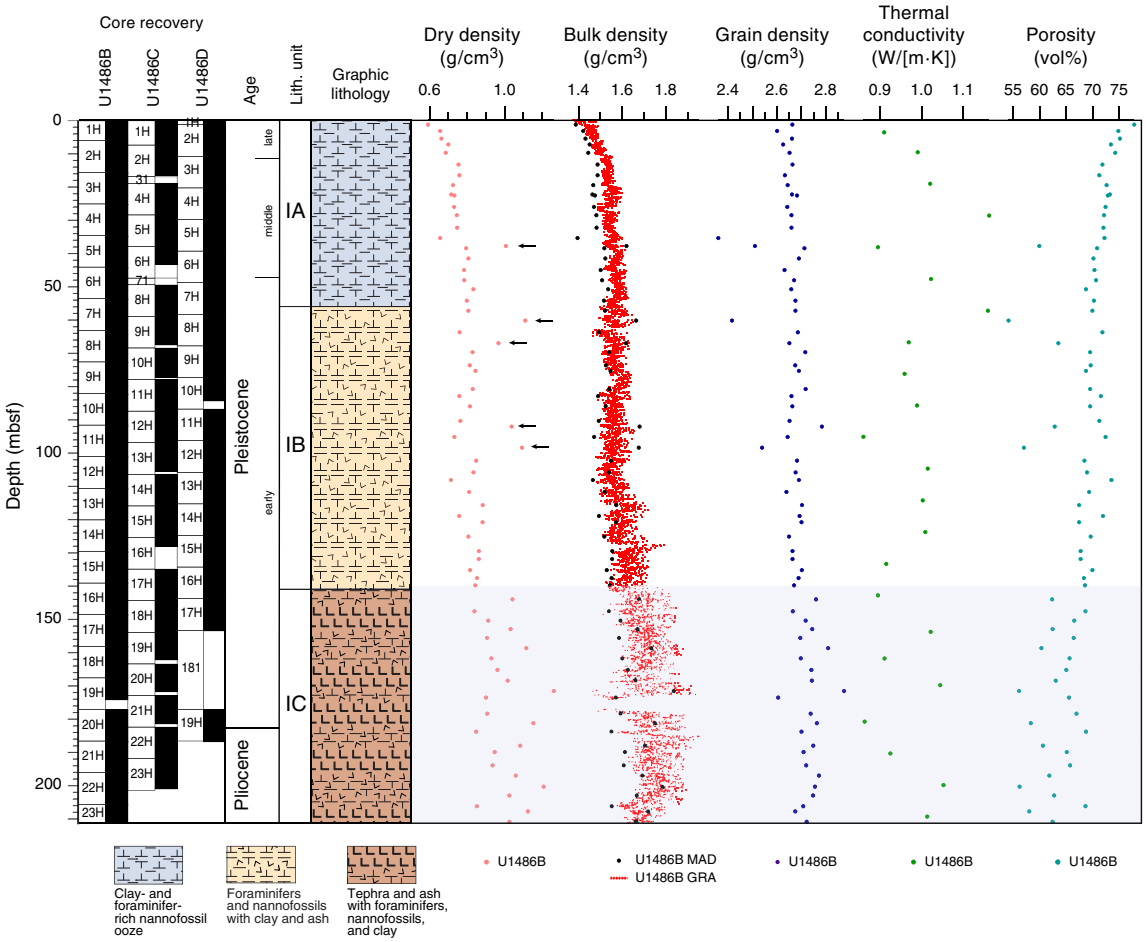

Figure F29. APCT-3 temperature-time series, Hole U1486B. Unshaded area = time interval with exponential decrease in temperature.

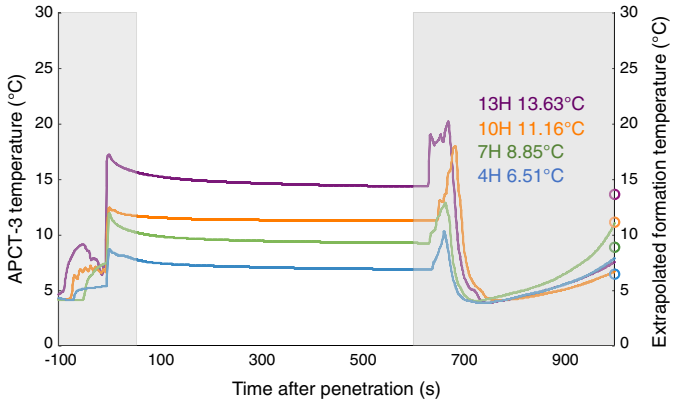

Figure F30. Heat flow calculations, Hole U1486B. Green line = calculated thermal resistance, gray vertical line = average thermal conductivity value used for calculation of thermal resistance, solid diamonds and dashed line = corrected thermal conductivity, open diamonds = uncorrected thermal conductivity.

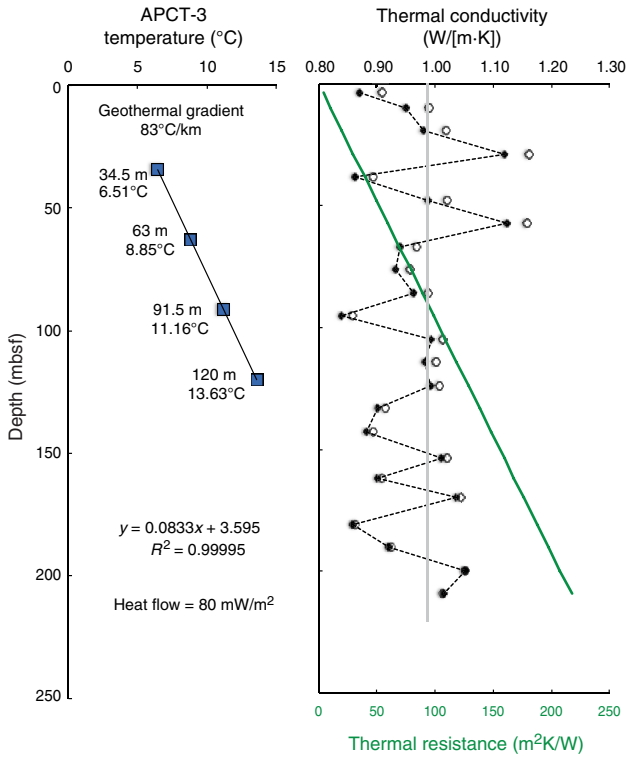

Stratigraphic correlation

Correlations between holes at Site U1486 were accomplished using Correlator software (version 2.1). Tie points were established almost exclusively with WRMSL magnetic susceptibility data (Table **T24**; Figure **F31**). In addition, we used NGR data to aid in making correlations. We constructed a splice for the entire site using Holes U1486B, U1486C, and U1486D (Table **T25**; Figures **F31**, **F32**, **F33**). The splice is continuous and well constrained from 0 to 222.59 m core composite depth below seafloor (CCSF). Below this depth, the offset of the last core of Hole U1486B is set using a growth factor and added to the end of the splice.

The CCSF scale is anchored to the mudline of Core 363-U1486C-1H, which is assigned a depth of 0 m CCSF. From this anchor, we worked downhole, using Correlator to establish a composite stratigraphy on a core-by-core basis. The upper 150 mbsf of Hole U1486B was heavily sampled (one 5 or 10 cm whole-round sample per section) for high-resolution interstitial water analyses (see **Geochemistry**), so our general approach was to avoid using material from 0 to 150 mbsf in Hole U1486B. However, because of poor recovery in a few intervals we had to use some short spliced intervals from Hole U1486B, which resulted in having to piece together the splice using all three holes. Hole U1486A only had one core (363-U1486A-1H), which did not correlate well to any of the cores in the other holes, but we determined its offset with a tentative tie point to Core 363-U1486C-1H and did not use it in the splice. We also avoided using Core U1486D-19H in the splice because preliminary work (see **Paleomagnetism**) suggested that it contains the Gauss/Matuyama reversal and we wanted to protect this interval from the high-resolution sampling that typically occurs in splice intervals. The splice is continuous with no gaps from 0 to 222.59 m CCSF. At the bottom of the splice, we used the Hole U1486B growth factor of 1.085 to set the offset of Core 363-U1486B-23H, which is the deepest core collected at Site U1486. This core contains basalt fragments and is presumed to be within meters of the basement (see **Operations** and **Core description**).

The splice interval table (Table **T25**) is intended to provide a sampling plan that can be used to generate high-resolution continuous records with minimal gaps; however, an "off-splice" sampling plan was also designed mainly for low-resolution studies. An explanation of the strategy used to determine the off-splice sampling plan, and a table of core intervals that should be used for off-splice sampling can be found in OFFSPLICE in **Supplementary material**.

The cumulative offset between mbsf and CCSF depth scales is nearly linear (Figure **F34A**). The growth factor is relatively low (8%–9%), which is expected from sediment that expands due to release of overburden but has minimal gas expansion due to low concentrations of methane and other gases (see **Geochemistry**). There are small changes in the growth factor and therefore in the cumulative offset with depth (Figure **F34B**) because of incomplete recovery in a few cores. IODP procedure places the sediment in a core with incomplete recovery at the top of the cored interval, which is assigned a mbsf depth using the drilling depth below seafloor (DSF), which is based on the length of the drill string deployed (see **Stratigraphic correlation** in the Expedition 363 methods chapter (Rosenthal et al., 2018a). However, the exact position of the recovered sediment in mbsf is unknown, and thus the process of correlation can potentially move the cores with incomplete recovery to a position on the CCSF scale that may not represent sediment expansion. Calculation of mass accumulation rates based on the CCSF scale should account for differential expansion by dividing apparent depth intervals by the appropriate growth factor.

Table T24. Affine table, Site U1486. MS = magnetic susceptibility, GF = growth factor. **Download table in CSV format.**

Core	Depth (mbsf)	Depth CCSF (m)	Offset (m)	Tie point depth CCSF (m)	Shift type	Data used	Reference hole, core
363-U1486A-							363-
1H	0.00	–0.11	–0.11	6.07	Tied to	MS	U1486C-1H
363-U1486B-							363-
1H	0.00	–0.02	–0.02	3.68	Tied to	MS	U1486C-1H
2H	6.00	5.51	–0.49	13.56	Tied to	MS	U1486C-2H
3H	15.50	17.25	1.75	20.42	Tied to	MS	U1486D-3H
4H	25.00	27.21	2.21	30.29	Tied to	MS	U1486C-4H
5H	34.50	37.71	3.21	41.58	Tied to	MS	U1486D-5H
6H	44.00	48.25	4.25	51.73	Tied to	MS	U1486D-6H
7H	53.50	59.08	5.58	63.34	Tied to	MS	U1486C-8H
8H	63.00	69.03	6.03	72.68	Tied to	MS	U1486C-9H
9H	72.50	78.75	6.25	82.71	Tied to	MS	U1486D-9H
10H	82.00	89.19	7.19	89.70	Tied to	MS	U1486D-10H
11H	91.50	99.47	7.97	102.20	Tied to	MS	U1486D-11H
12H	101.00	110.08	9.08	112.71	Tied to	MS	U1486D-12H
13H	110.50	120.31	9.81	125.19	Tied to	MS	U1486C-14H
14H	120.00	130.54	10.54	135.60	Tied to	MS	U1486D-15H
15H	129.50	141.22	11.72	144.57	Tied to	MS	U1486D-15H
16H	139.00	151.08	12.08	155.86	Tied to	MS	U1486C-17H
17H	148.50	161.24	12.74	165.08	Tied to	MS	U1486D-17H
18H	158.00	171.52	13.52	175.24	Tied to	MS	U1486C-19H
19H	167.50	181.97	14.47	182.97	Tied to	MS	U1486C-20H
20H	177.00	191.02	14.02	195.45	Tied to	MS	U1486C-21H
21H	186.50	202.26	15.76	205.58	Tied to	MS	U1486C-22H
22H	196.00	213.07	17.07	216.33	Tied to	MS	U1486C-23H
23H	205.50	222.97	17.47		Set; GF = 1.085		U1486B-22H
363-U1486C-							363-
1H	0.00	0.00	0.00	Mudline			
2H	7.30	8.80	1.50	9.94	Tied to	MS	U1486D-2H
4H	18.80	21.30	2.50	21.91	Tied to	MS	U1486B-3H
5H	28.30	31.52	3.22	32.55	Tied to	MS	U1486B-4H
6H	37.80	41.88	4.08	43.31	Tied to	MS	U1486B-5H
8H	49.30	53.95	4.65	61.34	Tied to	MS	U1486D-7H
9H	58.80	64.43	5.63	65.33	Tied to	MS	U1486B-7H
10H	68.30	74.30	6.00	80.05	Tied to	MS	U1486D-9H
12H	87.30	95.38	8.08	102.20	Tied to	MS	U1486D-11H
13H	96.80	104.97	8.17	106.65	Tied to	MS	U1486D-12H
14H	106.30	115.91	9.61	123.13	Tied to	MS	U1486D-13H
15H	115.80	126.28	10.48	133.90	Tied to	MS	U1486D-14H
16H	125.30	136.70	11.40	137.81	Tied to	MS	U1486B-14H
17H	134.80	147.05	12.25	154.90	Tied to	MS	U1486D-16H
18H	144.30	157.55	13.25	165.08	Tied to	MS	U1486D-17H
19H	153.80	167.70	13.90	168.40	Tied to	MS	U1486B-17H
20H	163.30	177.73	14.43	178.29	Tied to	MS	U1486B-18H
21H	172.80	187.75	14.95	188.37	Tied to	MS	U1486B-19H
22H	182.30	197.77	15.47	198.76	Tied to	MS	U1486B-20H
23H	191.80	207.73	15.93	208.58	Tied to	MS	U1486B-21H
363-U1486D-							363-
1H	0.00	0.00	0.00	Mudline			
2H	1.20	1.59	0.39	3.68	Tied to	MS	U1486C-1H
3H	10.70	11.73	1.03	13.56	Tied to	MS	U1486C-2H
4H	20.20	21.97	1.77	22.90	Tied to	MS	U1486C-4H
5H	29.70	32.31	2.61	32.55	Tied to	MS	U1486B-4H
6H	39.20	42.86	3.66	43.31	Tied to	MS	U1486B-5H
7H	48.70	52.88	4.18	53.47	Tied to	MS	U1486B-6H
8H	58.20	63.09	4.89	65.33	Tied to	MS	U1486B-7H
9H	67.70	73.32	5.62	73.85	Tied to	MS	U1486B-8H
10H	77.20	83.29	6.09	83.92	Tied to	MS	U1486B-9H
11H	86.70	93.09	6.39	93.71	Tied to	MS	U1486B-10H
12H	96.20	103.59	7.39	104.47	Tied to	MS	U1486C-12H
13H	105.70	113.77	8.07	114.22	Tied to	MS	U1486B-12H
14H	115.20	124.77	9.57	126.18	Tied to	MS	U1486B-13H
15H	124.70	135.28	10.58	136.26	Tied to	MS	U1486B-14H
16H	134.20	145.60	11.40	146.26	Tied to	MS	U1486B-15H
17H	143.70	156.35	12.65	157.18	Tied to	MS	U1486B-16H
19H	177.00	192.32	15.32	196.47	Tied to	MS	U1486B-20H

Figure F31. WRMSL MS data for Holes U1486B–U1486D divided into 50 m intervals. Upper panel shows the MS splice constructed by combining data from all holes. (Continued on next two pages.)

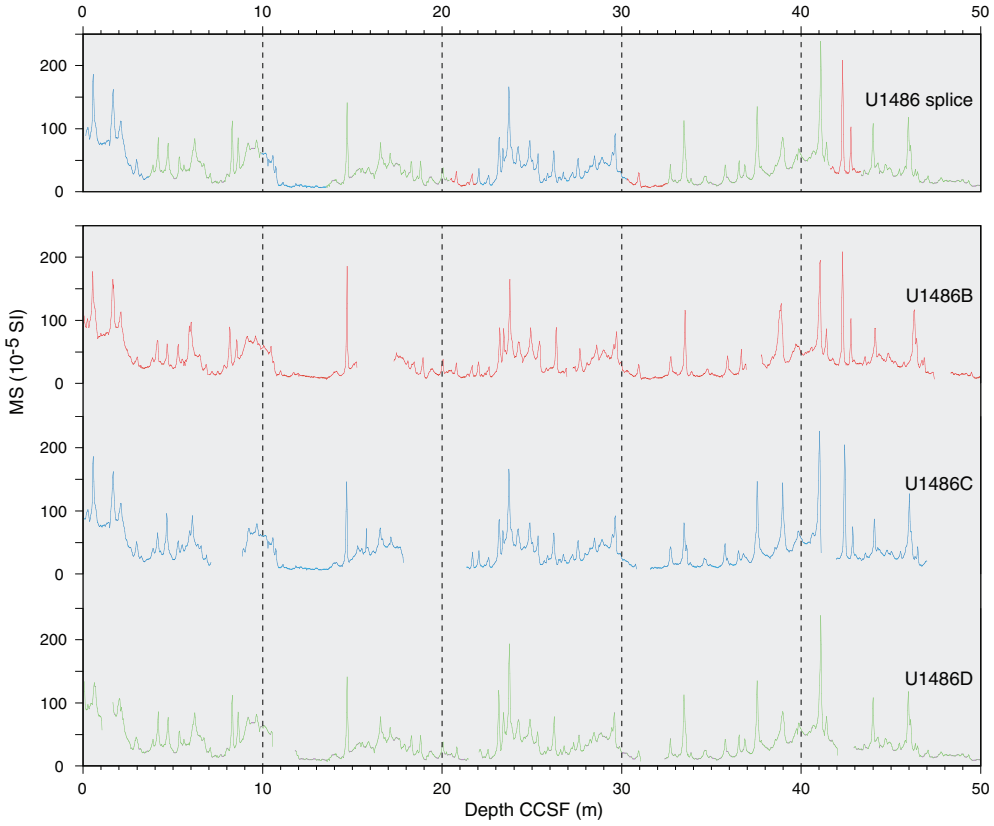

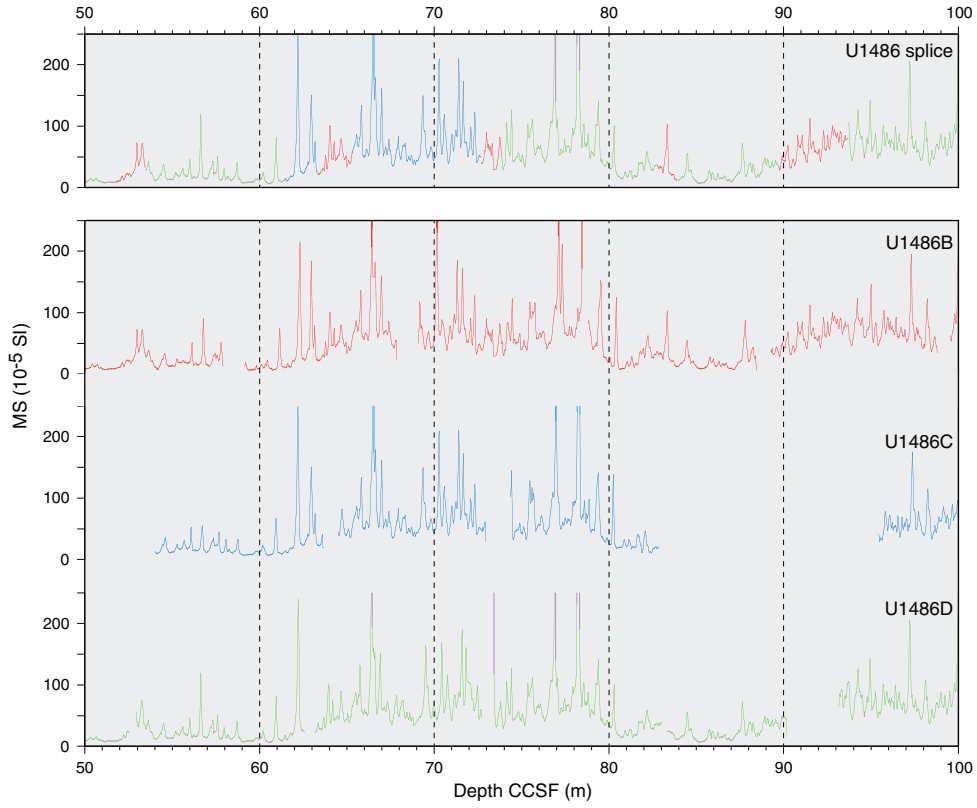

Figure F31 (continued). (Continued on next page.)

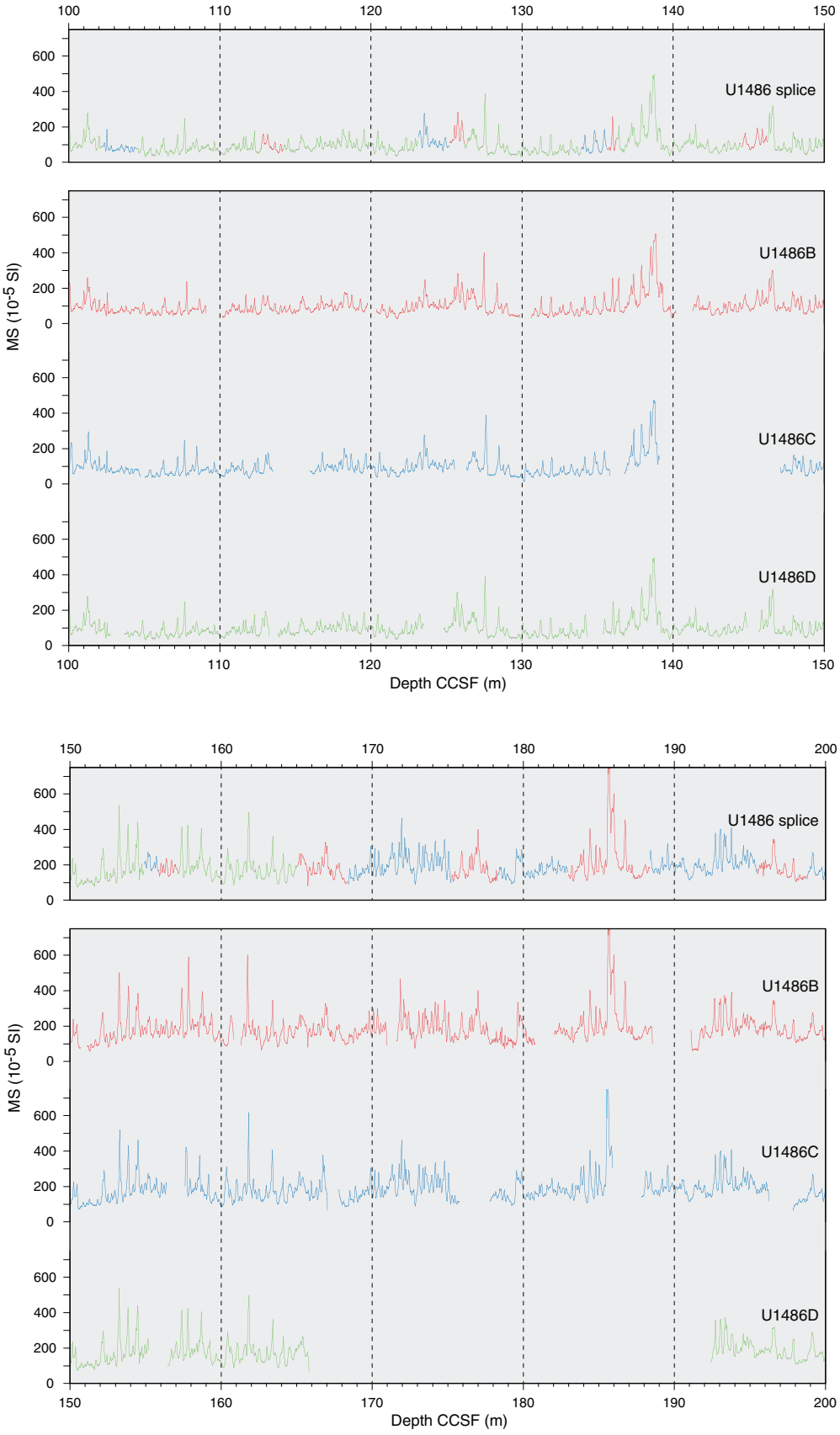

Figure F31 (continued).

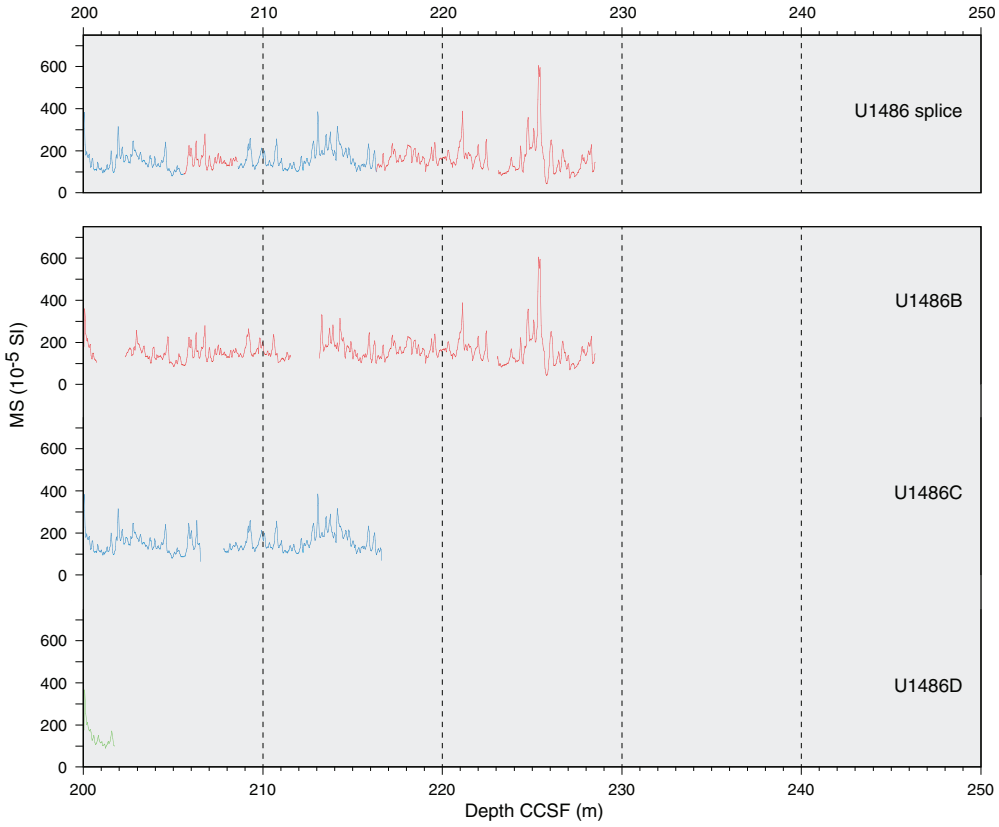

Table T25. Splice intervals, Site U1486. (Continued on next page.) **Download table in CSV format.**

Top of splice interval			Bottom of splice interval				
Core, section, interval (cm)	Depth (mbsf)	Depth CCSF (m)	Core, section, interval (cm)	Depth (mbsf)	Depth CCSF (m)	Splice type	Data used
363-			363-				
U1486C-1H-1, 0.0	0.00	0.00	U1486C-1H-3, 67.9	3.68	3.68	Tie	MS
U1486D-2H-2, 74.5	3.29	3.68	U1486D-2H-7, 9.8	9.55	9.94	Tie	MS
U1486C-2H-1, 113.9	8.44	9.94	U1486C-2H-4, 25.2	12.05	13.56	Tie	MS
U1486D-3H-2, 32.6	12.53	13.56	U1486D-3H-6, 119.4	19.39	20.42	Tie	MS
U1486B-3H-3, 22.7	18.68	20.42	U1486B-3H-4, 26.6	20.17	21.91	Tie	MS
U1486C-4H-1, 61.6	19.42	21.91	U1486C-4H-6, 149.6	27.80	30.29	Tie	MS
U1486B-4H-3, 8.4	28.08	30.29	U1486B-4H-4, 83.9	30.34	32.55	Tie	MS
U1486D-5H-1, 24.1	29.94	32.55	U1486D-5H-7, 27.8	38.98	41.58	Tie	MS
U1486B-5H-3, 87.6	38.38	41.58	U1486B-5H-4, 110.6	40.11	43.31	Tie	MS
U1486D-6H-1, 45.7	39.66	43.31	U1486D-6H-6, 137.3	48.07	51.73	Tie	MS
U1486B-6H-3, 48.1	47.48	51.73	U1486B-6H-4, 72.5	49.23	53.47	Tie	MS
U1486D-7H-1, 59.3	49.29	53.47	U1486D-7H-6, 95.5	57.16	61.34	Tie	MS
U1486C-8H-5, 138.8	56.69	61.34	U1486C-8H-7, 38.8	58.69	63.34	Tie	MS
U1486B-7H-3, 126.0	57.76	63.34	U1486B-7H-5, 25.2	59.75	65.33	Tie	MS
U1486C-9H-1, 89.8	59.70	65.33	U1486C-9H-6, 74.9	67.05	72.68	Tie	MS
U1486B-8H-3, 65.3	66.65	72.68	U1486B-8H-4, 32.0	67.82	73.85	Tie	MS
U1486D-9H-1, 52.3	68.22	73.85	U1486D-9H-7, 38.4	77.08	82.71	Tie	MS
U1486B-9H-3, 96.1	76.46	82.71	U1486B-9H-4, 66.9	77.67	83.92	Tie	MS
U1486D-10H-1, 62.6	77.83	83.92	U1486D-10H-5, 41.1	83.61	89.70	Tie	MS
U1486B-10H-1, 51.1	82.51	89.70	U1486B-10H-4, 2.1	86.52	93.71	Tie	MS
U1486D-11H-1, 62.4	87.32	93.71	U1486D-11H-7, 11.3	95.81	102.20	Tie	MS
U1486C-12H-5, 81.9	94.12	102.20	U1486C-12H-7, 19.8	96.39	104.47	Tie	MS
U1486D-12H-1, 87.3	97.07	104.47	U1486D-12H-7, 11.9	105.32	112.71	Tie	MS
U1486B-12H-2, 113.5	103.64	112.71	U1486B-12H-3, 114.2	105.14	114.22	Tie	MS
U1486D-13H-1, 44.8	106.15	114.22	U1486D-13H-7, 33.4	115.05	123.13	Tie	MS
U1486C-14H-5, 121.3	113.51	123.13	U1486C-14H-7, 27.8	115.58	125.19	Tie	MS
U1486B-13H-4, 38.0	115.38	125.19	U1486B-13H-4, 136.6	116.37	126.18	Tie	MS
U1486D-14H-1, 140.9	116.61	126.18	U1486D-14H-7, 12.6	124.33	133.90	Tie	MS
U1486C-15H-6, 11.7	123.42	133.90	U1486C-15H-7, 32.3	125.12	135.60	Tie	MS

Table T25 (continued).

Top of splice interval			Bottom of splice interval				
Core, section, interval (cm)	Depth (mbsf)	Depth CCSF (m)	Core, section, interval (cm)	Depth (mbsf)	Depth CCSF (m)	Splice type	Data used
U1486B-14H-4, 56.4	125.06	135.60	U1486B-14H-4, 121.8	125.72	136.26	Tie	MS
U1486D-15H-1, 98.0	125.68	136.26	U1486D-15H-7, 29.1	133.99	144.57	Tie	MS
U1486B-15H-3, 34.7	132.85	144.57	U1486B-15H-4, 53.8	134.54	146.26	Tie	MS
U1486D-16H-1, 66.0	134.86	146.26	U1486D-16H-7, 30.0	143.50	154.90	Tie	MS
U1486C-17H-6, 34.5	142.65	154.90	U1486C-17H-7, 29.5	143.61	155.86	Tie	MS
U1486B-16H-4, 28.0	143.78	155.86	U1486B-16H-5, 10.3	145.10	157.18	Tie	MS
U1486D-17H-1, 82.8	144.53	157.18	U1486D-17H-6, 122.8	152.43	165.08	Tie	MS
U1486B-17H-3, 83.6	152.34	165.08	U1486B-17H-5, 115.2	155.65	168.40	Tie	MS
U1486C-19H-1, 70.0	154.50	168.40	U1486C-19H-6, 3.9	161.34	175.24	Tie	MS
U1486B-18H-3, 71.7	161.72	175.24	U1486B-18H-5, 77.4	164.77	178.29	Tie	MS
U1486C-20H-1, 56.6	163.87	178.29	U1486C-20H-4, 74.4	168.54	182.97	Tie	MS
U1486B-19H-1, 99.5	168.50	182.97	U1486B-19H-5, 64.4	173.89	188.37	Tie	MS
U1486C-21H-1, 61.6	173.42	188.37	U1486C-21H-6, 20.1	180.50	195.45	Tie	MS
U1486B-20H-3, 143.1	181.43	195.45	U1486B-20H-6, 23.4	184.73	198.76	Tie	MS
U1486C-22H-1, 99.2	183.29	198.76	U1486C-22H-6, 31.7	190.12	205.58	Tie	MS
U1486B-21H-3, 32.7	189.83	205.58	U1486B-21H-5, 32.9	192.83	208.58	Tie	MS
U1486C-23H-1, 85.3	192.65	208.58	U1486C-23H-6, 109.4	200.39	216.33	Tie	MS
U1486B-22H-3, 25.2	199.25	216.33	U1486B-22H-7, 80.0	205.52	222.59	Set	MS
U1486B-23H-1, 0.0	205.50	222.97	U1486B-23H-4, 108.0	211.09	228.56		

Figure F32. Spliced SHMSL L*, NGR, and WRMSL MS and GRA bulk density data, Site U1486.

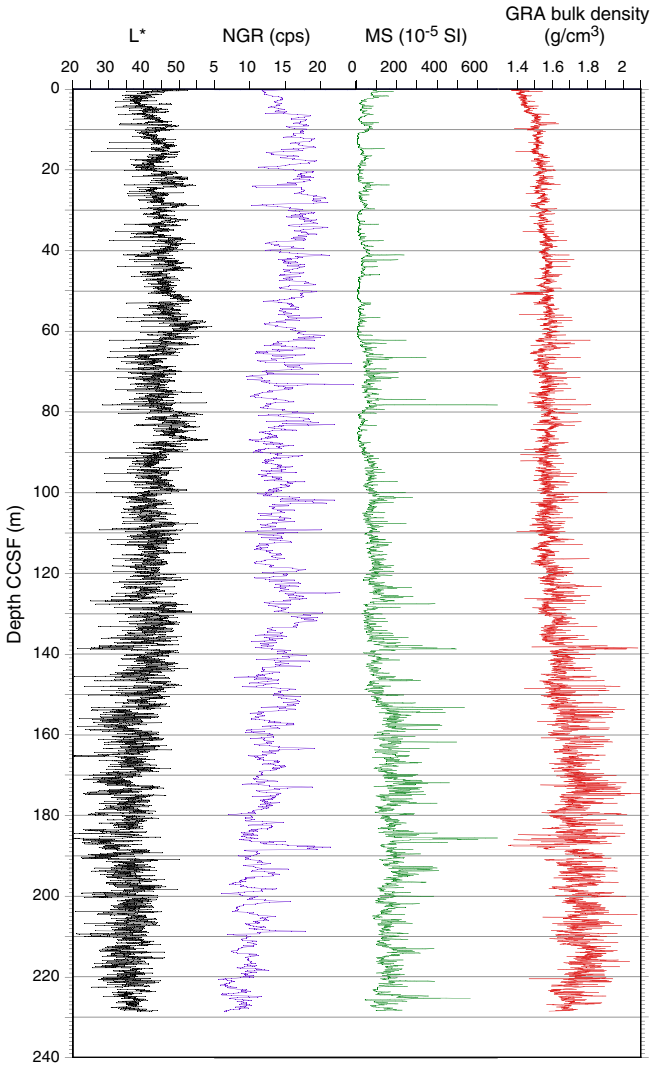

Figure F33. Spliced MS data for Holes U1486B (red), U1486C (blue), and U1486D (green) plotted on spliced core images (core photo generated using CODD; Wilkens et al., 2017).

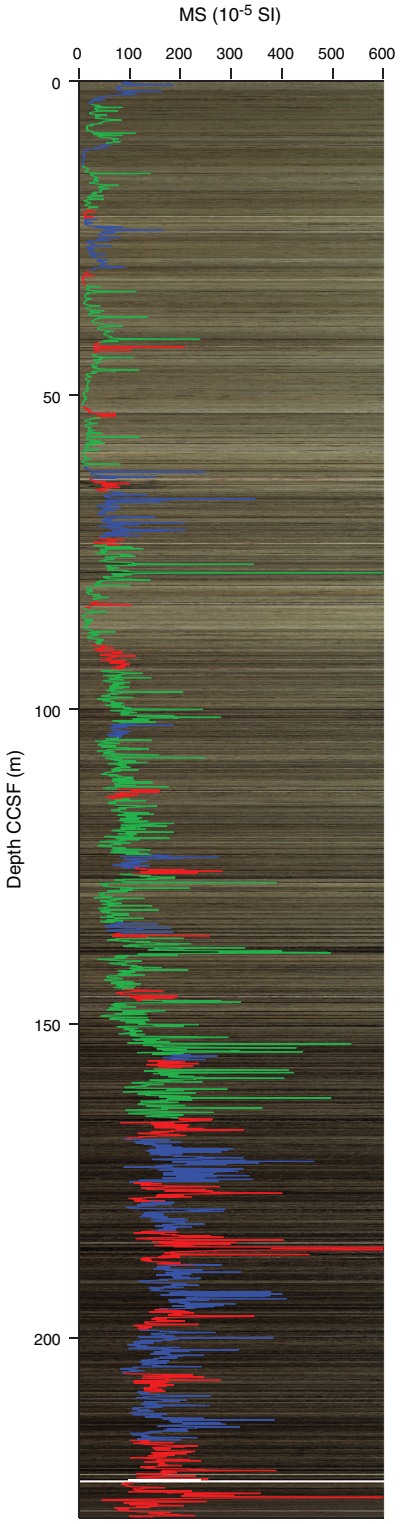

Figure F34. A. Comparison of mbsf and composite depth scales in the Site U1486 splice. B. Comparison of the growth of cumulative depth offset and mbsf depth scale.

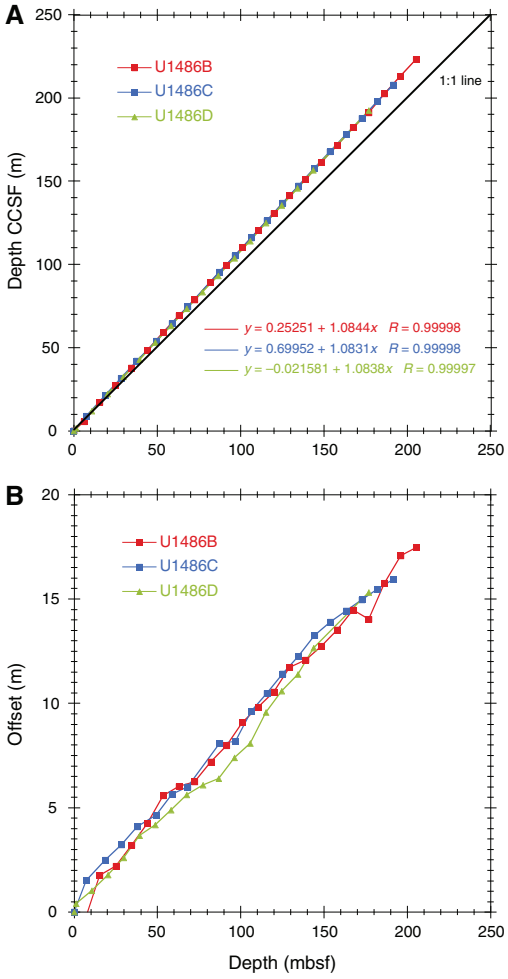

Geochemistry

At Site U1486, geochemical analyses were carried out on Hole U1486B to 210.0 mbsf. High-resolution interstitial water sampling was conducted in the upper ~150 mbsf with the goal of reconstructing the chloride (Cl) concentration and $\delta^{18}O$ of Antarctic Intermediate Water (AAIW) during the Last Glacial Maximum (LGM). The interstitial water geochemical profiles at this site reflect the variable sedimentation and tectonic evolution of this setting over the past ~2 million years. Profiles in the uppermost sediments reflect a modest degree of organic matter remineralization, whereas deeper than ~60 mbsf (Subunit IB) they are dominated by interaction of interstitial water with volcanogenic sediment, including abundant tephras, dispersed ash, and discrete volcanogenic layers throughout the sediment column. The profiles in the lowermost 40 m of the succession suggest possible oceanic crustal fluid influence on the interstitial water geochemical signatures. Carbonate ($CaCO_3$) con-

Table T26. Volatile hydrocarbon concentrations, Hole U1486B. **Download table in CSV format.**

Figure F35. Methane, $CaCO_3$, TOC, and TN profiles, Hole U1486B.

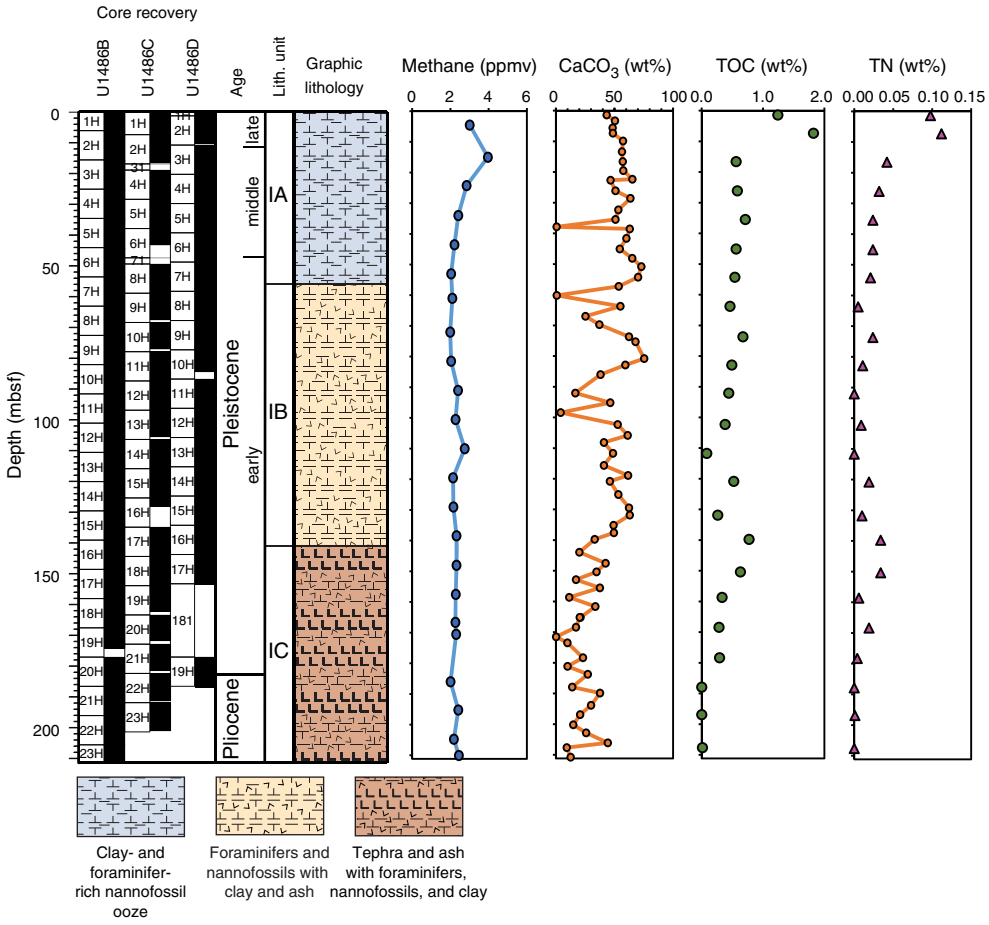

tent throughout the hole is highly variable (0.3–75.4 wt%). Total organic carbon (TOC) content ranges between 0 and 1.8 wt% and decreases downhole. For detailed background on organic matter remineralization and clay mineral alteration, see **Geochemistry** in the Site U1482 chapter (Rosenthal et al., 2018b).

Results

Volatile hydrocarbons

Headspace gas samples were taken at a frequency of one sample per core in Hole U1486B as part of the routine environmental protection and safety-monitoring program (Table **T26**; Figure **F35**). Methane concentration was low (<4 ppmv) throughout Hole U1486B, consistent with the interstitial water analyses that show abundant sulfate (SO_4) to the bottom of the hole (see **Sulfate and barium**). Ethane and propane were below detection limit.

Bulk sediment geochemistry

$CaCO_3$, inorganic carbon (IC), TOC, and total nitrogen (TN) were measured on sediment samples from Hole U1486B (Table **T27**; Figure **F35**). The $CaCO_3$ content is highly variable, ranging from 0.3 to 75.4 wt%, with an average of 40.5 wt%. Overall, $CaCO_3$ content is higher in the upper ~140 mbsf, corresponding to lithologic Subunits IA and IB. Ash and silt samples have extremely low $CaCO_3$ content.

Table T27. Calcium carbonate ($CaCO_3$), total organic carbon (TOC), and total nitrogen (TN), Hole U1486A. **Download table in CSV format.**

TOC content ranges between 0 and 1.8 wt% with an average of 0.5 wt% and exhibits a decreasing trend downhole. TN content is very low (average 0.03 wt%) and shows a similar decreasing trend with depth. Because TN is below the detection limit in a number of samples, we conclude that the ratio of TOC to total nitrogen (C/N ratio) might not be reliable at Site U1486.

Interstitial water chemistry

Site U1486 was sampled at high resolution (one whole-round sample per section for Sections 1–6 downhole to ~150 mbsf) for interstitial water geochemistry to facilitate reconstruction of the density of AAIW during the LGM (e.g., McDuff, 1985; Adkins et al., 2002; Adkins and Schrag, 2003). A total of 106 whole-round samples were taken from Hole U1486B. Of these, 39 interstitial water samples and 1 mudline sample were processed for all standard shipboard analyses following the procedures described in **Geochemistry** in the Expedition 363 methods chapter (Rosenthal et al., 2018a). The remainder were split and processed for shore-based analyses. Interstitial water chemistry data are reported in Table **T28**.

Chlorinity and salinity

The Cl interstitial water profile at Site U1486 displays a variable but continuous increase from a mudline concentration of 553.7 mM to a maximum value of 572.0 mM at 210.0 mbsf (Figure **F36**). From the surface to 170.4 mbsf, small variations of ~4 to ~8 mM from sample to sample are superimposed on the increasing trend, whereas from 170.4 mbsf to the base of the hole, variability is reduced. The Cl profile at this site is likely influenced by two processes. The first is the interaction between interstitial water and volcanogenic material, which is abundant throughout the recovered sediment sequence at Site U1486, particularly deeper than ~60 mbsf (see **Core description**). Decoupling of the Cl and sodium (Na) profiles (Figures **F36**, **F37**) indicates that the observed changes in Cl are likely due to hydration reactions involving volcanic or clay minerals. The second likely influence on Cl is diffusion and communi-

Table T28. Interstitial water geochemical data, Hole U1486B. **Download table in CSV format.**

Figure F36. Interstitial water concentration profiles, Hole U1486B. Black stars = mudline samples. Fe, Mn, and Ba mudline concentrations were below detection limit and are not plotted.

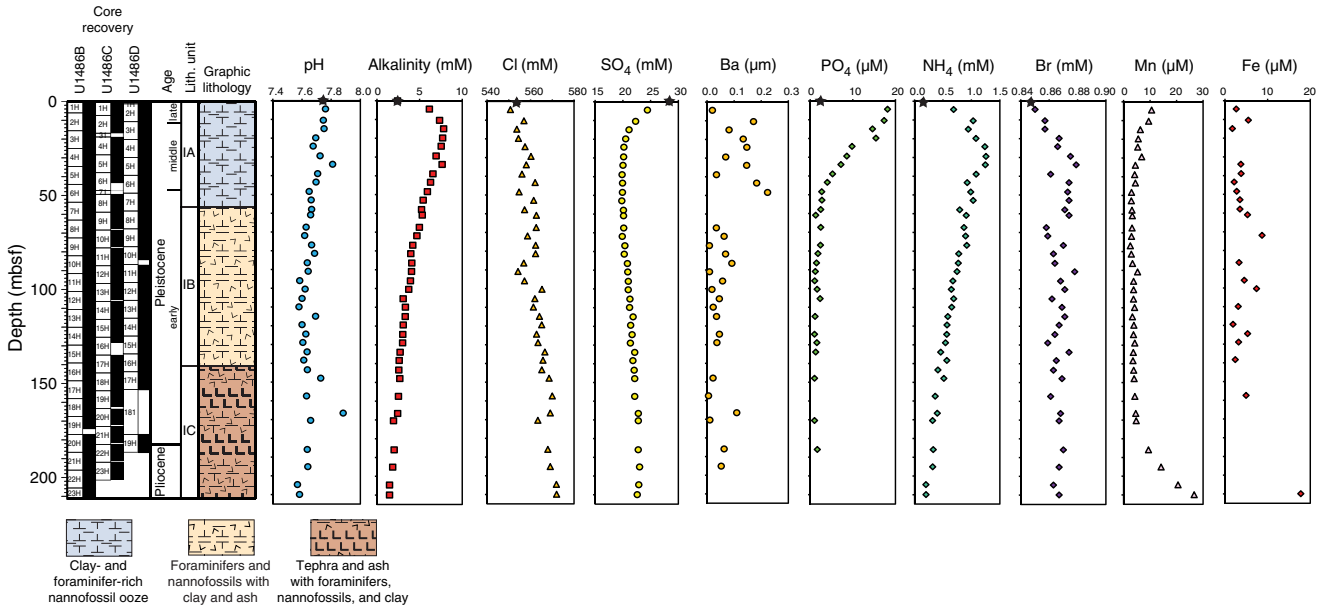

Figure F37. Interstitial water concentration profiles, Hole U1486B. Black stars = mudline samples.

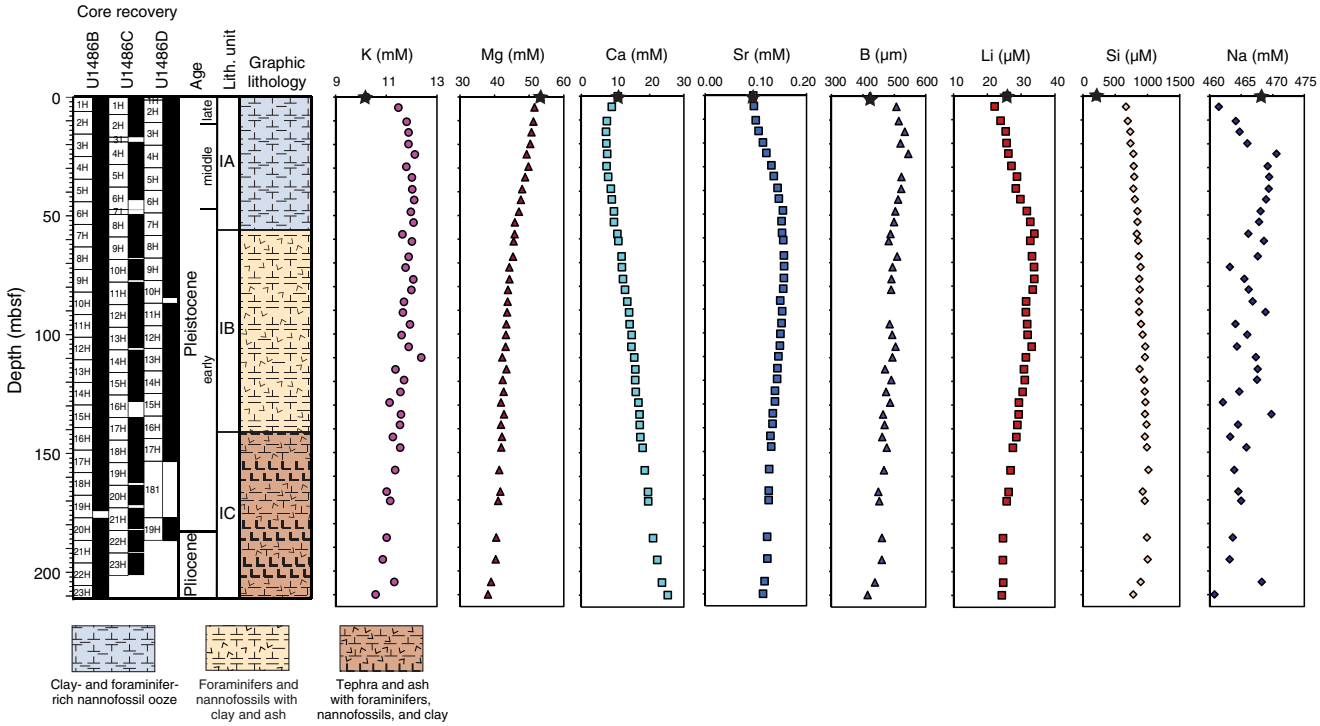

cation between sediment interstitial water and water from the relatively young oceanic basement (see **Discussion**). Salinity (not shown) is less variable than Cl but shows the same general trend of increasing values downhole. Salinity is 36 at the mudline and increases slightly to 37 at depth.

Reconstruction of salinity and $\delta^{18}O$ of bottom water during the LGM requires that advection and diffusion dominate interstitial water profiles of Cl and $\delta^{18}O$ (Adkins and Schrag, 2003). The low-resolution shipboard Cl data suggest that in situ and crustal alteration reactions strongly affect the interstitial water chemistry at Site U1486, which may complicate the reconstruction of the salinity and $\delta^{18}O$ of AAIW during the LGM at this site.

Alkalinity and pH

Alkalinity at Site U1486 increases sharply from a mudline concentration of 2.4 mM to maximum values of 7.7 to 7.8 mM between 14.9 and 19.8 mbsf (Figure **F36**). Below 19.8 mbsf, alkalinity decreases downhole to a minimum of 1.46 mM at the base of the hole. The minor increase in alkalinity in the upper part of the profile is likely the result of organic matter remineralization by SO_4 reduction. This idea is supported by a nearly identical trend in the ammonium (NH_4) profile (Figure **F36**) and a slight reduction in SO_4 concentration at the depth of the alkalinity maximum. Below this depth, the decreasing trend likely reflects interactions between interstitial water, oceanic crust, and volcanogenic material (see **Discussion**).

The pH generally decreases downhole, from 7.7 at the mudline to 7.6 at the base of the hole (Figure **F36**). As with Cl, small-scale variations in pH are superimposed on this overall trend, possibly related to weathering of volcanogenic sediment (see **Geochemistry** in the Site U1484 chapter [Rosenthal et al., 2018d]). High pH (7.88) is observed at 166.5 mbsf, which is roughly coincident with a transition to darker, coarser sediment that has possibly been altered by hydrothermal processes (see **Core description**).

Sulfate and barium

The SO_4 profile in Hole U1486B is typical of an open-ocean setting as opposed to a continental margin site in that SO_4 is not completely depleted but is present at elevated concentrations (~20 mM) downhole. SO_4 decreases steeply from a mudline concentration of 28.3 mM to 20.2 mM at 24.2 mbsf, reaches a minimum concentration (19.8 mM) by 52.9 mbsf, and then increases gradually to 23 mM by the base of the hole (Figure **F36**). This profile indicates that although SO_4 reduction is taking place in the upper portion of the sediment column, the intensity of organic matter remineralization is not high enough to facilitate complete consumption of SO_4 and a switch to organic matter fermentation and methanogenesis. This is supported by the phosphate (PO_4), ammonium (NH_4), and methane profiles (Figures **F35**, **F36**). The increase in SO_4 concentration deeper than ~53 mbsf is most likely due to upward diffusion from the oceanic crust (see **Discussion**).

The interstitial water barium (Ba) profile displays considerable scatter and very low values (<1 µM) compared with Ba concentrations of 5–10 µM at nearby Sites U1484 and U1485 (Figure **F36**). In the solid phase, Ba is associated with organic matter, which at this site is relatively low. During organic matter degradation, Ba can be reprecipitated as barite ($BaSO_4$), which remains in the solid phase in the presence of dissolved SO_4. Thus, the overall low organic matter contents and presence of dissolved SO_4 at Site U1486 act together to keep the dissolved Ba concentration low.

Phosphate, ammonium, and bromide

PO_4 concentration increases abruptly from the mudline concentration of 2.2 µM to a maximum of 18.1 µM at 4.4 mbsf. Between 4.4 and 60.9 mbsf, PO_4 concentration decreases steeply and remains stable (<1% variability) and low (average concentration of 0.9 µM) to the base of the hole (Figure **F36**). Overall, PO_4 concentration is markedly lower than observed at Sites U1484 and U1485, reflecting the lower organic matter content of the sediment.

The NH_4 profile closely resembles the alkalinity profile, with an increase over the upper ~24 mbsf from a mudline concentration of 0.2 mM to a maximum concentration of 1.24–1.25 mM between 24.2 and 33.9 mbsf (Figure **F36**). Deeper than 33.9 mbsf, NH_4 concentration decreases to a minimum of 0.2 mM at the base of the hole. As with PO_4, NH_4 concentration is lower at this site compared to Sites U1484 and U1485. The downhole increase in NH_4 in the upper ~40 mbsf most likely reflects organic matter remineralization, whereas below this depth the downhole decrease probably reflects NH_4 uptake during clay alteration (see **Geochemistry** in the Site U1482 chapter [Rosenthal et al., 2018b]).

Bromide (Br) interstitial water concentration is relatively constant, ranging between 0.85 and 0.88 µM over the entire profile (Figure **F36**). Most of the change in the Br profile occurs in the upper 33.9 mbsf, with an increase from 0.85 µM at the mudline to 0.88 µM at 33.9 mbsf, consistent with a minor to moderate amount of organic matter remineralization within this interval. Deeper than 33.9 mbsf, Br concentration is relatively constant. Small-scale variations (~1%) in Br show an inverse relationship with similar scale variations (~1%) in the PO_4 profile, suggesting a small degree of variability in organic matter content downhole.

Manganese and iron

Manganese (Mn) concentration is below detection limit at the mudline, increases to 10.6 µM at 4.4 mbsf, likely reflecting the transition from oxic to suboxic organic matter degradation, and then decreases to ~3 µM by 48.4 mbsf where SO_4 reduction occurs (Figure **F36**). Between 48.4 and 170.4 mbsf, Mn concentration is low and invariant; however, at 170.4 mbsf, Mn increases abruptly and reaches a maximum concentration of 26.7 µM at the base of the hole. This pronounced downhole increase likely reflects the interaction of interstitial water with the oceanic crust and Mn- and Fe-rich basalts (see **Discussion**).

The Fe concentration profile displays some scatter downhole (Figure **F36**). In the upper ~160 mbsf, Fe concentration ranges between 1.7 and 8.7 µM, with one-third of measured samples below the detection limit. A maximum Fe concentration (17.8 µM) occurs in the deepest sample (210.0 mbsf). The overall low Fe concentration is likely due to precipitation of pyrite in the zone of SO_4 reduction (upper ~30 mbsf; see observations of sulfides in **Core description**) and scavenging by other secondary minerals (e.g., clays) that may be produced within the sediment. Peaks of dissolved Fe concentration in the upper portion of the sediment sequence may reflect weathering of volcanogenic sediment, whereas the single high value at the base of the hole is likely due to leaching of Fe and Mn from basalt or addition of these elements from basement fluids.

Potassium, magnesium, and calcium

Potassium (K) concentration increases from a mudline concentration of 10.2 to 11.8 mM in the upper 10.4 mbsf. K concentration is relatively constant, with some small variability (~5%) down to

~120 mbsf. K concentration slowly decreases from 11.7 mM at 119.4 mbsf to 10.6 mM at 210.0 mbsf (Figure **F37**). The decreasing trend in the lower 90 m of the hole suggests a possible basement sink for K, such as clay mineral authigenesis or interaction with oceanic crust and diffusion (see **Discussion**).

Ca and magnesium (Mg) profiles at Site U1486 show an inverse relationship (Figure **F37**). Ca concentration decreases slightly (10.7–10.4 mM) between 0 and 7.5 mbsf before increasing steadily to the bottom of the hole to a maximum concentration of 25.3 mM. Mg concentration shows a downhole decrease over the entire hole, from a mudline concentration of 53.3 mM to a minimum of 38.1 mM. Slight curvature in both profiles is noted between 185.9 and 210.0 mbsf, which is close to the acoustic basement observed on the seismic profile (Figure **F3**). This type of inverse relationship between Ca and Mg concentrations was previously observed at several sites that were drilled close to basement (Kastner and Gieskes, 1976; McDuff and Gieskes, 1976; Gieskes and Lawrence, 1981; McDuff, 1981) and can be explained by weathering of oceanic basalt and sediments directly overlying the basement (see **Discussion**).

Strontium and boron

Strontium (Sr) concentration increases from a mudline value of 0.09 mM to a maximum concentration of 0.15–0.16 mM between 48.4 and 81.4 mbsf (Figure **F37**). This increase in Sr concentration occurs in a foraminifer- and nannofossil-rich ooze and clay in the upper ~60 mbsf, suggesting that the Sr trend here reflects dissolution and precipitation of carbonates (Baker et al., 1982). Deeper than 81.4 mbsf, Sr concentration decreases to 0.11 mM at the base of the hole indicating a sink for Sr toward the base of the hole and the influence of diffusion. As with Ca, Mg, Mn, and Fe, the slope of the Sr profile is steeper in the lower ~25 m of sediment.

Boron (B) concentration increases rapidly from the mudline (421.6 µM) to 4.4 mbsf (506.6 µM) and then increases slightly to a maximum concentration of 533.2 µM at 14.9 mbsf (Figure **F37**). Below 14.9 mbsf, B decreases steadily downhole to a minimum of 415.2 µM at 210.0 mbsf. Similar to a number of other interstitial water profiles (pH, Cl, K, PO_4, and Br) at this site, small-scale variations in B concentration (20–40 µM) are superimposed on the overall decreasing trend. Both leaching of terrigenous material and weathering of volcanic ash have been suggested to increase interstitial water B concentration (Deyhle and Kopf, 2002; James et al., 2003).

Lithium, silica, and sodium

Lithium (Li) concentration decreases slightly from the mudline (25.8 µM) to a minimum (22.1 µM) at 4.4 mbsf and increases to 33.9 µM at 57.9 mbsf, where it remains constant until 81.4 mbsf (Figure **F37**). Below that, Li concentration decreases downhole to 24.3 µM at 210.0 mbsf. The similarity between the Li and Sr profiles suggests a link between Li concentration and carbonate dissolution and reprecipitation over the upper ~60 mbsf and possibly a sink for Li or a diffusion-controlled profile below this depth.

Silica (Si) concentration increases markedly from 206.3 µM at the mudline to 666.1 µM at 4.4 mbsf (Figure **F37**). Between 4.4 and 195.1 mbsf, Si concentration gradually increases from 666.1 to 1002.8 µM and then rapidly decreases to 778.5 µM at the base of the hole. The linear increase of Si over much of the hole suggests a profile that is strongly influenced by diffusion. The sharp decrease of Si between 185.0 and 210.0 mbsf likely reflects the weathering of oceanic crust that also influences the Cl, Mn, Fe, K, Ca, and Mg profiles.

The sodium (Na) profile displays a great deal of scatter downhole (Figure **F37**) to 461.5 mM at 4.4 mbsf, below which depth it varies between ~460 and 471 mM. There is not good agreement between the Cl and Na profiles, indicating that if weathering of ash or clay minerals is influencing the two ions, it is through different processes (i.e., hydration/dehydration reactions that release or take up water versus ion-exchange reactions that release or take up Na).

Discussion

The sedimentary sequence at Site U1486 captures several transitions that are likely related to the tectonic evolution and volcanic history of this setting (see **Background and objectives** and **Core description**) and are in turn reflected in the interstitial water profiles. Based on recovery of some pieces of basalt and the occurrence of APC refusal at the base of Hole U1486B (see **Core description** and **Operations**), this site may contain a (nearly) complete record of sedimentation since ocean crust formation, providing an excellent opportunity to study the geochemical interactions between basaltic crust and sediment.

In the upper ~60 mbsf (predominantly lithologic Subunit IA), the sediment consists mostly of foraminifer-rich nannofossil ooze with variable amounts of clay and minimal amounts of volcanogenic material. The interstitial water profiles in this interval are dominated by changes in alkalinity, SO_4, PO_4, NH_4, and Br that reflect a modest degree of organic matter remineralization.

Below ~60 mbsf, there is a notable increase in the abundance of volcanogenic material (see **Core description**). Deeper than 60 mbsf, the interstitial water profiles show steeper linear gradients (both increasing and decreasing toward the base of the hole) suggesting that upward diffusion of crustal fluid influences the interstitial water profiles, which is further discussed below. Superimposed on these linear gradients are smaller scale trends of variability, particularly noticeable in K, B, Na, pH, Cl, and Fe, which can be explained by the interaction of interstitial water with reactive volcanogenic sediments/minerals and clay mineral alteration (see **Geochemistry** in the Site U1482 chapter, **Geochemistry** in the Site U1484 chapter, and **Geochemistry** in the Site U1485 chapter [Rosenthal et al., 2018b, 2018d, 2018e]). Specifically, clay mineral authigenesis and hydration can help explain the Cl, B, K, Na, and Fe profiles, whereas weathering of volcanogenic sediments can contribute to the K, pH, and Fe profiles. Preliminary examination of the layers composed of volcanogenic particles within lithologic Subunit IB (the lithology composing the interval between ~60 and ~140 mbsf) suggests a slightly more felsic composition than the sediments below 140 mbsf in lithologic Subunit IC (see **Core description**), which may explain why variability is more evident in the K record than in the Fe record.

Deeper than ~140 mbsf, the sediments are noticeably darker in color, coarser grained, and contain a high amount of mafic volcanic material (see **Core description**). The crustal age at this site is presumed to be fairly young (~3.5 Ma; see **Background and objectives**), which would suggest ample opportunity for interaction between the oceanic crust, crustal fluids, the sedimentary sequence, and interstitial water at this site. This interaction is clearly reflected in several interstitial water profiles, including Ca, Mg, Fe, Si, Cl, and SO_4.

The inverse relationship between Ca and Mg profiles downhole is a common feature for sites that have been drilled to basement (Gieskes and Lawrence, 1981). The increase in Ca is attributed to submarine weathering of basal sediment and basalt, whereas the

formation of authigenic smectites near the basement can serve as a sink for Mg (Kastner and Gieskes, 1976). At this site, decreases in K, Mg, and alkalinity are consistent with the occurrence of these two processes in the ~30 m above the base of Hole U1486B. The mostly linear concentration gradients observed above this interval in K, Mg, and Ca reflect the influence of diffusion.

A noticeable change in the shape of the Cl profile at ~170 mbsf may be attributable to hydration/dehydration reactions. The coarser sediment at this interval could also facilitate more rapid diffusion, explaining the change in interstitial water gradient. Alternatively, interaction between interstitial water and the crustal material at Site U1486 may not be limited to alteration reactions but could also include the mixing of sedimentary and crustal fluids. This hypothesis is supported by the gradual increase of SO_4 concentration at depth, suggesting upward diffusion of water with a relatively high SO_4 concentration originating from the oceanic crust. The marked increases in iron and manganese concentrations and the decrease in silica concentration could similarly be attributed either to weathering of mafic oceanic crustal sediments or interaction between interstitial water bearing more traditional sedimentary signatures and crustal fluids. The influence of crustal fluids on the lowermost sediments at this site is supported by the observation of zeolites (see **Core description**), which can form as low-temperature hydrothermal alteration products of oceanic crust (e.g., Alt et al., 1986; Hay and Sheppard, 2001).

References

Adkins, J.F., and Schrag, D.P., 2003. Reconstructing Last Glacial Maximum bottom water salinities from deep-sea sediment pore fluid profiles. *Earth and Planetary Science Letters,* 216(1–2):109–123. **https://doi.org/10.1016/S0012-821X(03)00502-8**

Alt, J.C., Honnorez, J., Laverne, C., and Emmermann, R., 1986. Hydrothermal alteration of a 1 km section through the upper oceanic crust, Deep Sea Drilling Project Hole 504B: mineralogy, chemistry, and evolution of seawater-basalt interactions. *Journal of Geophysical Research: Solid Earth,* 91(B10):10309–10335. **https://doi.org/10.1029/JB091iB10p10309**

Baker, P.A., Gieskes, J.M., and Elderfield, H., 1982. Diagenesis of carbonates in deep-sea sediments: evidence from Sr/Ca ratios and interstitial dissolved Sr^{2+} data. *Journal of Sedimentary Research,* 52(1):71–82. **https://doi.org/10.1306/212F7EE1-2B24-11D7-8648000102C1865D**

Baldwin, S.L., Fitzgerald, P.G., and Webb, L.E., 2012. Tectonics of the New Guinea region. *Annual Review of Earth and Planetary Sciences,* 40(1):495–520. **https://doi.org/10.1146/annurev-earth-040809-152540**

Berggren, W.A., Kent, D.V., Swisher, C.C., III, and Aubry, M.-P., 1995. A revised Cenozoic geochronology and chronostratigraphy. *In* Berggren, W.A., Kent, D.V., Aubry, M.-P., and Hardenbol, J. (Eds.), *Geochronology, Time Scales and Global Stratigraphic Correlation.* Special Publication - SEPM (Society for Sedimentary Geology), 54:129–212. **https://doi.org/10.2110/pec.95.04.0129**

Cande, S.C., and Kent, D.V., 1995. Revised calibration of the geomagnetic polarity timescale for the Late Cretaceous and Cenozoic. *Journal of Geophysical Research: Solid Earth,* 100(B4):6093–6095. **https://doi.org/10.1029/94JB03098**

Chaisson, W.P., and Pearson, P.N., 1997. Planktonic foraminifer biostratigraphy at Site 925: middle Miocene–Pleistocene. *In* Shackleton, N.J., Curry, W.B., Richter, C., and Bralower, T.J. (Eds.), *Proceedings of the Ocean Drilling Program, Scientific Results,* 154: College Station, TX (Ocean Drilling Program), 3–31. **https://doi.org/10.2973/odp.proc.sr.154.104.1997**

Deyhle, A., and Kopf, A., 2002. Strong B enrichment and anomalous $\delta^{11}B$ in pore fluids from the Japan Trench forearc. *Marine Geology,* 183(1–4):1–15. **https://doi.org/10.1016/S0025-3227(02)00186-X**

Dowsett, H.J., 1988. Diachroneity of late Neogene microfossils in the southwest Pacific Ocean: application of the graphic correlation method. *Paleoceanography,* 3(2):209–222. **https://doi.org/10.1029/PA003i002p00209**

Expedition 339 Scientists, 2013. Expedition 339 summary. *In* Stow, D.A.V., Hernández-Molina, F.J., Alvarez Zarikian, C.A., and the Expedition 339 Scientists, *Proceedings of the Integrated Ocean Drilling Program,* 339: Tokyo (Integrated Ocean Drilling Program Management International, Inc.). **https://doi.org/10.2204/iodp.proc.339.101.2013**

Gieskes, J.M., and Lawrence, J.R., 1981. Alteration of volcanic matter in deep-sea sediments: evidence from the chemical composition of interstitial waters from deep sea drilling cores. *Geochimica Cosmochimica Acta,* 45(10):1687–1703. **https://doi.org/10.1016/0016-7037(81)90004-1**

Hay, R.L., and Sheppard, R.A., 2001. Occurrence of zeolites in sedimentary rocks: an overview. *Reviews in Mineralogy and Geochemistry,* 45(1):217–234. **https://doi.org/10.2138/rmg.2001.45.6**

Hilgen, F.J., Lourens, L.J., and Van Dam, J.A., 2012. The Neogene period. With contributions by A.G. Beu, A.F. Boyes, R.A. Cooper, W. Krijgsman, J.G. Ogg, W.E. Piller, and D.S. Wilson. *In* Gradstein, F.M., Ogg, J.G., Schmitz, M.D., and Ogg, G.M. (Eds.), *The Geologic Time Scale:* Oxford, United Kingdom (Elsevier), 923–978. **https://doi.org/10.1016/B978-0-444-59425-9.00029-9**

Iijima, A., 1980. Geology of natural zeolites and zeolitic rocks. *Pure and Applied Chemistry*, 52(9):2115–2130. **https://doi.org/10.1351/pac198052092115**

James, R.H., Allen, D.E., and Seyfried, W.E., Jr., 2003. An experimental study of alteration of oceanic crust and terrigenous sediments at moderate temperatures (51 to 350°C): insights as to chemical processes in near-shore ridge-flank hydrothermal systems. *Geochimica et Cosmochimica Acta,* 67(4):681–691. **https://doi.org/10.1016/S0016-7037(02)01113-4**

Jones, R.W., 1994. *The Challenger Foraminifera:* New York (Oxford University Press USA).

Karlin, R., and Levi, S., 1983. Diagenesis of magnetic minerals in recent hemipelagic sediments. *Nature,* 303(5915):327–330. **https://doi.org/10.1038/303327a0**

Kastner, M., and Gieskes, J.M., 1976. Interstitial water profiles and sites of diagenetic reactions, Leg 35, DSDP, Bellingshausen Abyssal Plain. *Earth and Planetary Science Letters,* 33(1):11–20. **https://doi.org/10.1016/0012-821X(76)90152-7**

Le Friant, A., Ishizuka, O., Stroncik, N.A., and the Expedition 340 Scientists, 2013. *Proceedings of the Integrated Ocean Drilling Program,* 340: Tokyo (Integrated Ocean Drilling Program Management International, Inc.). **https://doi.org/10.2204/iodp.proc.340.2013**

Maher, B.A., 1988. Magnetic properties of some synthetic submicron magnetites. *Geophysics Journal of the Royal Astronomical Society,* 94:83–96.

McDuff, R.E., 1981. Major cation gradients in DSDP interstitial waters: the role of diffusive exchange between seawater and upper oceanic crust. *Geochimica et Cosmochimica Acta,* 45(10):1705–1713. **https://doi.org/10.1016/0016-7037(81)90005-3**

McDuff, R.E., 1985. The chemistry of interstitial waters, Deep Sea Drilling Project Leg 86. *In* Heath, G.R., Burckle, L.H., et al., *Initial Reports of the Deep Sea Drilling Project,* 86: Washington, DC (U.S. Government Printing Office), 675–687. **https://doi.org/10.2973/dsdp.proc.86.131.1985**

McDuff, R.E., and Gieskes, J.M., 1976. Calcium and magnesium profiles in DSDP interstitial waters: diffusion or reaction? *Earth and Planetary Science Letters,* 33(1):1–10. **https://doi.org/10.1016/0012-821X(76)90151-5**

McNeill, L.C., Dugan, B., Petronotis, K.E., Backman, J., Bourlange, S., Chemale, F., Chen, W., Colson, T.A., Frederik, M.C.G., Guèrin, G., Hamahashi, M., Henstock, T., House, B.M., Hüpers, A., Jeppson, T.N., Kachovich, S., Kenigsberg, A.R., Kuranaga, M., Kutterolf, S., Milliken, K.L., Mitchison, F.L., Mukoyoshi, H., Nair, N., Owari, S., Pickering, K.T., Pouderoux, H.F.A., Yehua, S., Song, I., Torres, M.E., Vannucchi, P., Vrolijk, P.J., Yang, T., and Zhao, X., 2017. Expedition 362 summary. *In* McNeill, L.C., Dugan, B., Petronotis, K.E., and the Expedition 362 Scientists, *Sumatra Subduction Zone.* Proceedings of the International Ocean Discovery Program, 362: College Station, TX (International Ocean Discovery Program). **https://doi.org/10.14379/iodp.proc.362.101.2017**

Mohtadi, M., Bergmann, F., Blanquera, R.V.C., Buleka, J., Carag, J.W.M., Carriére-Garwood, J., et al., 2013. Report and preliminary results of RV *SONNE* cruise SO-228, Kaohsiung-Townsville, 04.05.2013-23.06.2013, EISPAC-WESTWIND-SIODP. *Berichte, MARUM - Zentrum für Marine Umweltwissenschaften, Fachbereich Geowissenschaften, Universität Bremen,* 295. **https://www.marum.de/en/Research/RV-SONNE-SO-228.html**

Pälike, H., Nishi, H., Lyle, M., Raffi, I., Gamage, K., Klaus, A., and the Expedition 320/321 Scientists, 2010. Expedition 320/321 summary. *In* Pälike, H., Lyle, M., Nishi, H., Raffi, I., Gamage, K., Klaus, A., and the Expedition 320/321 Scientists, *Proceedings of the Integrated Ocean Drilling Program,* 320/321: Tokyo (Integrated Ocean Drilling Program Management International, Inc.). **https://doi.org/10.2204/iodp.proc.320321.101.2010**

Pribnow, D., Kinoshita, M., and Stein, C., 2000. *Thermal Data Collection and Heat Flow Recalculations for Ocean Drilling Program Legs 101–180:* Hanover, Germany (Institute for Joint Geoscientific Research, Institut für Geowissenschaftliche Gemeinschaftsaufgaben [GGA]). **http://www-odp.tamu.edu/publications/heatflow/ODPReprt.pdf**

Raffi, I., and Flores, J.-A., 1995. Pleistocene through Miocene calcareous nannofossils from eastern equatorial Pacific Ocean (Leg 138). *In* Pisias, N.G., Mayer, L.A., Janecek, T.R., Palmer-Julson, A., and van Andel, T.H. (Eds.), *Proceedings of the Ocean Drilling Program, Scientific Results,* 138: College Station, TX (Ocean Drilling Program), 233–286. **https://doi.org/10.2973/odp.proc.sr.138.112.1995**

Resig, J.M., Frost, G.M., Ishikawa, N., and Perembo, R.C.B., 2001. Micropaleontological and paleomagnetic approaches to stratigraphic anomalies in rift basins: ODP Site 1109, Woodlark Basin. *In* Wilson, R.C.L., Whitmarsh, R.B., Taylor, B., and Froitzheim, N. (Eds.), *Non-Volcanic Rifting of Continental Margins: A Comparison of Evidence from Land and Sea.* Geological Society Special Publication, 187(1):389–404. **https://doi.org/10.1144/GSL.SP.2001.187.01.19**

Richter, C., Acton, G., Endris, C., and Radsted, M., 2007. *Technical Note 34: Handbook for Shipboard Paleomagnetists.* Ocean Drilling Program. **https://doi.org/10.2973/odp.tn.34.2007**

Rosenthal, Y., Holbourn, A., and Kulhanek, D.K., 2016. *Expedition 363 Scientific Prospectus: Western Pacific Warm Pool.* International Ocean Discovery Program. **https://doi.org/10.14379/iodp.sp.363.2016**

Rosenthal, Y., Holbourn, A.E., Kulhanek, D.K., Aiello, I.W., Babila, T.L., Bayon, G., Beaufort, L., Bova, S.C., Chun, J.-H., Dang, H., Drury, A.J., Dunkley Jones, T., Eichler, P.P.B., Fernando, A.G.S., Gibson, K.A., Hatfield, R.G., Johnson, D.L., Kumagai, Y., Li, T., Linsley, B.K., Meinicke, N., Mountain, G.S., Opdyke, B.N., Pearson, P.N., Poole, C.R., Ravelo, A.C., Sagawa, T., Schmitt, A., Wurtzel, J.B., Xu, J., Yamamoto, M., and Zhang, Y.G., 2018a. Expedition 363 methods. *In* Rosenthal, Y., Holbourn, A.E., Kulhanek, D.K., and the Expedition 363 Scientists, *Western Pacific Warm Pool.* Proceedings of the International Ocean Discovery Program, 363: College Station, TX (International Ocean Discovery Program). **https://doi.org/10.14379/iodp.proc.363.102.2018**

Rosenthal, Y., Holbourn, A.E., Kulhanek, D.K., Aiello, I.W., Babila, T.L., Bayon, G., Beaufort, L., Bova, S.C., Chun, J.-H., Dang, H., Drury, A.J., Dunkley Jones, T., Eichler, P.P.B., Fernando, A.G.S., Gibson, K.A., Hatfield, R.G., Johnson, D.L., Kumagai, Y., Li, T., Linsley, B.K., Meinicke, N., Mountain, G.S., Opdyke, B.N., Pearson, P.N., Poole, C.R., Ravelo, A.C., Sagawa, T., Schmitt, A., Wurtzel, J.B., Xu, J., Yamamoto, M., and Zhang, Y.G., 2018b. Site U1482. *In* Rosenthal, Y., Holbourn, A.E., Kulhanek, D.K., and the Expedition 363 Scientists, *Western Pacific Warm Pool.* Proceedings of the International Ocean Discovery Program, 363: College Station, TX (International Ocean Discovery Program). **https://doi.org/10.14379/iodp.proc.363.103.2018**

Rosenthal, Y., Holbourn, A.E., Kulhanek, D.K., Aiello, I.W., Babila, T.L., Bayon, G., Beaufort, L., Bova, S.C., Chun, J.-H., Dang, H., Drury, A.J., Dunkley Jones, T., Eichler, P.P.B., Fernando, A.G.S., Gibson, K.A., Hatfield, R.G., Johnson, D.L., Kumagai, Y., Li, T., Linsley, B.K., Meinicke, N., Mountain, G.S., Opdyke, B.N., Pearson, P.N., Poole, C.R., Ravelo, A.C., Sagawa, T., Schmitt, A., Wurtzel, J.B., Xu, J., Yamamoto, M., and Zhang, Y.G., 2018c. Site U1483. *In* Rosenthal, Y., Holbourn, A.E., Kulhanek, D.K., and the Expedition 363 Scientists, *Western Pacific Warm Pool.* Proceedings of the International Ocean Discovery Program, 363: College Station, TX (International Ocean Discovery Program). **https://doi.org/10.14379/iodp.proc.363.104.2018**

Rosenthal, Y., Holbourn, A.E., Kulhanek, D.K., Aiello, I.W., Babila, T.L., Bayon, G., Beaufort, L., Bova, S.C., Chun, J.-H., Dang, H., Drury, A.J., Dunkley Jones, T., Eichler, P.P.B., Fernando, A.G.S., Gibson, K.A., Hatfield, R.G., Johnson, D.L., Kumagai, Y., Li, T., Linsley, B.K., Meinicke, N., Mountain, G.S., Opdyke, B.N., Pearson, P.N., Poole, C.R., Ravelo, A.C., Sagawa, T., Schmitt, A., Wurtzel, J.B., Xu, J., Yamamoto, M., and Zhang, Y.G., 2018d. Site U1484. *In* Rosenthal, Y., Holbourn, A.E., Kulhanek, D.K., and the Expedition 363 Scientists, *Western Pacific Warm Pool.* Proceedings of the International Ocean Discovery Program, 363: College Station, TX (International Ocean Discovery Program). **https://doi.org/10.14379/iodp.proc.363.105.2018**

Rosenthal, Y., Holbourn, A.E., Kulhanek, D.K., Aiello, I.W., Babila, T.L., Bayon, G., Beaufort, L., Bova, S.C., Chun, J.-H., Dang, H., Drury, A.J., Dunkley Jones, T., Eichler, P.P.B., Fernando, A.G.S., Gibson, K.A., Hatfield, R.G., Johnson, D.L., Kumagai, Y., Li, T., Linsley, B.K., Meinicke, N., Mountain, G.S., Opdyke, B.N., Pearson, P.N., Poole, C.R., Ravelo, A.C., Sagawa, T., Schmitt, A., Wurtzel, J.B., Xu, J., Yamamoto, M., and Zhang, Y.G., 2018e. Site U1485. *In* Rosenthal, Y., Holbourn, A.E., Kulhanek, D.K., and the Expedition 363 Scientists, *Western Pacific Warm Pool.* Proceedings of the International Ocean Discovery Program, 363: College Station, TX (International Ocean Discovery Program). **https://doi.org/10.14379/iodp.proc.363.106.2018**

Rosenthal, Y., Holbourn, A.E., Kulhanek, D.K., Aiello, I.W., Babila, T.L., Bayon, G., Beaufort, L., Bova, S.C., Chun, J.-H., Dang, H., Drury, A.J., Dunkley Jones, T., Eichler, P.P.B., Fernando, A.G.S., Gibson, K.A., Hatfield, R.G., Johnson, D.L., Kumagai, Y., Li, T., Linsley, B.K., Meinicke, N., Mountain, G.S., Opdyke, B.N., Pearson, P.N., Poole, C.R., Ravelo, A.C., Sagawa, T., Schmitt, A., Wurtzel, J.B., Xu, J., Yamamoto, M., and Zhang, Y.G., 2018f. Site U1487. *In* Rosenthal, Y., Holbourn, A.E., Kulhanek, D.K., and the Expedition 363 Scientists, *Western Pacific Warm Pool.* Proceedings of the International Ocean Discovery Program, 363: College Station, TX (International Ocean Discovery Program). **https://doi.org/10.14379/iodp.proc.363.108.2018**

Rosenthal, Y., Holbourn, A.E., Kulhanek, D.K., Aiello, I.W., Babila, T.L., Bayon, G., Beaufort, L., Bova, S.C., Chun, J.-H., Dang, H., Drury, A.J., Dunkley Jones, T., Eichler, P.P.B., Fernando, A.G.S., Gibson, K.A., Hatfield, R.G., Johnson, D.L., Kumagai, Y., Li, T., Linsley, B.K., Meinicke, N., Mountain, G.S., Opdyke, B.N., Pearson, P.N., Poole, C.R., Ravelo, A.C., Sagawa, T., Schmitt, A., Wurtzel, J.B., Xu, J., Yamamoto, M., and Zhang, Y.G., 2018g. Site U1490. *In* Rosenthal, Y., Holbourn, A.E., Kulhanek, D.K., and the Expedition 363 Scientists, *Western Pacific Warm Pool.* Proceedings of the International Ocean Discovery Program, 363: College Station, TX (International Ocean Discovery Program). **https://doi.org/10.14379/iodp.proc.363.111.2018**

Rothwell, R.G., 1989. *Minerals and Mineraloids in Marine Sediments: An Optical Identification Guide:* London (Elsevier). **https://doi.org/10.1007/978-94-009-1133-8**

Rowan, C.J., Roberts, A.P., and Broadbent, T., 2009. Reductive diagenesis, magnetite dissolution, greigite growth and paleomagnetic smoothing in marine sediments: a new view. *Earth and Planetary Science Letters,* 277(1–2):223–235. **https://doi.org/10.1016/j.epsl.2008.10.016**

Stein, C.A., and Stein, S., 1992. A model for the global variation in oceanic depth and heat flow with lithospheric age. *Nature,* 359(6391):123–129. **https://doi.org/10.1038/359123a0**

Stoner, J.S., and St-Onge, G., 2007. Magnetic stratigraphy in paleooceanography: reversal, excursion, paleointensity and secular variation. *In* Hillaire-Marcel, C., and de Vernal, A. (Eds.), *Developments in Marine Geology* (Volume 1): *Proxies in Late Cenozoic Paleoceanography.* Stein, R. (Series Ed.): Amsterdam (Elsevier B.V.), 99–138. **https://doi.org/10.1016/S1572-5480(07)01008-1**

Tachikawa, K., Cartapanis, O., Vidal, L., Beaufort, L., Barlyaeva, T., and Bard, E., 2011. The precession phase of hydrological variability in the Western Pacific Warm Pool during the past 400 ka. *Quaternary Science Reviews,* 30(25–26):3716–3727. **https://doi.org/10.1016/j.quascirev.2011.09.016**

Tachikawa, K., Timmermann, A., Vidal, L., Sonzogni, C., and Timm, O.E., 2013. Southern Hemisphere orbital forcing and its effects on CO_2 and tropical Pacific climate. *Climate of the Past Discussions,* 9(2):1869–1900. **https://doi.org/10.5194/cpd-9-1869-2013**

Taylor, B., 1979. Bismarck Sea: evolution of a back-arc basin. *Geology,* 7(4):171–174. **https://doi.org/10.1130/0091-7613(1979)7<171:BSEOAB>2.0.CO;2**

van Morkhoven, F.P.C.M., Berggren, W.A., Edwards, A.S.,and Oertli, H.J., 1986. Cenozoic cosmopolitan deep-water benthic foraminifera. *Bulletin des Centres de Recherches Exploration-Production Elf-Aquitaine,* 11.

Weiner, A.K.M., Weinkauf, M.F.G., Kurasawa, A., Darling, K.F., and Kucera, M., 2015. Genetic and morphometric evidence for parallel evolution of the *Globigerinella calida* morphotype. *Marine Micropaleontology,* 114:19–35. **https://doi.org/10.1016/j.marmicro.2014.10.003**

Wilkens, R.H., Westerhold, T., Drury, A.J., Lyle, M., Gorgas, T., and Tian, J., 2017. Revisiting the Ceara Rise, equatorial Atlantic Ocean: isotope stratigraphy of ODP Leg 154. *Climate of the Past,* 13:779–793. **https://doi.org/10.5194/cp-13-779-2017**

Zijderveld, J.D.A., 1967. AC demagnetization of rocks: analysis of results. *In* Collinson, D.W., Creer, K.M., and Runcorn, S.K. (Eds.), *Methods in Palaeomagnetism:* Amsterdam (Elsevier), 254–286.